Clay-laden subaqueous gravity flows

Flow structures, deposits, and run-out distance

Hermidas, Navid

DOI
10.4233/uuid:0777f2f6-55fb-4670-b3ed-2318070cc7e7

Publication date
2019

Document Version
Final published version

Citation (APA)
Hermidas, N. (2019). *Clay-laden subaqueous gravity flows: Flow structures, deposits, and run-out distance*. [Dissertation (TU Delft), Delft University of Technology]. https://doi.org/10.4233/uuid:0777f2f6-55fb-4670-b3ed-2318070cc7e7

Important note
To cite this publication, please use the final published version (if applicable).
Please check the document version above.

CLAY-LADEN SUBAQUEOUS GRAVITY FLOWS

FLOW STRUCTURES, DEPOSITS, AND RUN-OUT DISTANCE

CLAY-LADEN SUBAQUEOUS GRAVITY FLOWS

FLOW STRUCTURES, DEPOSITS, AND RUN-OUT DISTANCE

Proefschrift

ter verkrijging van de graad van doctor
aan de Technische Universiteit Delft,
op gezag van de Rector Magnificus, prof. dr. ir. T.H.J.J. van der Hagen,
voorzitter van het College voor Promoties,
in het openbaar te verdedigen op
maandag 17 juni 2019 om 12:30 uur

door

Navid HERMIDAS

ingenieur luchtvaart- en ruimtevaart techniek,
Technische Universiteit Delft, Nederland.
geboren te Teheran, Iran.

Dit proefschrift is goedgekeurd door de

promotor: Prof. dr. S.M. Luthi
copromotor: Dr. J.T. Eggenhuisen

Samenstelling promotiecommissie:

Rector Magnificus	Technische Universiteit Delft, voorzitter
Prof. dr. S.M. Luthi	Technische Universiteit Delft, promotor
Dr. J.T. Eggenhuisen	Universiteit Utrecht, copromotor

Onafhankelijke leden:

Prof. dr. C.P.J.W. van Kruijsdijk	Technische Universiteit Delft
Prof. dr. J.C. Winterwerp	Technische Universiteit Delft
Prof. dr. P. Coussot	Université Paris-Est, France
Dr. J. Baas	Bangor University, United Kingdom
Prof. dr. A.W. Martinius	Technische Universiteit Delft, reservelid

Overige leden:

Dr. R. Silva Jacinto	IFREMER, Brest, Fance

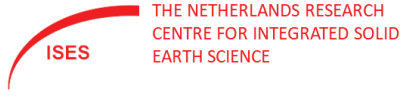

Keywords: Gravity flows, thixotropy, clay suspension, viscosity bifurcation, run-out distance, flow structures, debris flows

Printed by: Gildeprint

Front: Flysch facies during a sunset in April, depicting sequences of sedimentary rock layers from submarine gravity flow deposits. Picture, courtesy of Francisco Llano Tomé, was taken in Sakoneta, between Deba and Zumaya, in Basque Country.

ISBN 978-94-6323-690-4

An electronic version of this dissertation is available at
http://repository.tudelft.nl/.

“There is a pleasure in the pathless woods,
There is a rapture on the lonely shore,
There is society, where none intrudes,
By the deep sea, and music in its roar:
I love not man the less, but Nature more,
From these our interviews, in which I steal
From all I may be, or have been before,
To mingle with the Universe, and feel
What I can ne’er express, yet cannot all conceal."

Lord Byron, 1788 - 1824

CONTENTS

SUMMARY

Submarine gravity flows constitute the last link in the source-to-sink sediment transport chain. They are the main mechanism for the transportation of sediment from the shallower to the deeper parts of the ocean. Due to their great volume, mobility, and power, they pose a formidable threat to the offshore infrastructures, and can generate tsunamis which can result in human mortality and cause great damage to onshore structures. In addition, deposits of ancient submarine gravity flows host many hydrocarbon reservoirs. The quality of these reservoirs is primarily controlled by the grain size and the clay concentration of the flows that deposited the sediments. Due to the growing population and rise in the per capita energy consumption, connecting the dynamics of clay-laden density flows to their depositional characteristics has become important for oil and gas exploration purposes. The principle questions that were investigated in this study were: (1) How are the dynamics of subaqueous gravity flows related to their deposits?, and, (2) Why are these flows able to travel so far?

In an attempt to address the first question, a series of laboratory flume experiments was performed using 9%, 15%, and 21% sediment concentrations composed of sand, silt, clay, and tap water, on varying bed slopes of 6°, 8°, and 9.5°, and with discharge rates of 10 and 15 m^3/h. Based on the shape of the velocity profiles of the experimental flows, it was ascertained that the most complete anatomy of subaqueous clay-rich gravity flows is composed of three vertically stacked layers, 1) a free shear layer, 2) a plug layer, and 3) a boundary layer. The flow states within the boundary and free shear layers of the experimental flows were established using calculation of the inner variable, self-similarity considerations, and the magnitude of the apparent viscosity. Based on the state of the flow within these regions, a classification was then proposed for clay-rich gravity flows. According to this classification, a clay-rich flow may fall within one of four distinct flow types: (1) a plug flow with a laminar free shear layer, a plug layer, and a laminar boundary layer, (2) a top transitional plug flow, containing a turbulent free shear layer, a plug layer, and a laminar boundary layer, (3) a transitional turbidity current, with a turbulent free shear layer, no plug layer, and a laminar boundary layer, and (4) a fully turbulent turbidity current.

Study of the deposits emplaced by the experimental flows revealed some specific signatures for each flow type. In general, clay-rich PFs resulted in either no deposition or deposition of a thin bottom sand layer. TTPFs and TTCs were mostly characterized by a thin bottom sand layer. The bottom sand layers in PFs, TTPFs, and TTCs were overlain by a mud-sand mixture that was emplaced by the tail of the flow. TCs resulted in the deposition of a thick massive bottom sand layer which was overlain by either a mud-sand mixture or a sand and silt planar lamination from the tail of the flow.

In order to connect the regimes of each flow type with those of analogue large-scale flows in nature, four non-dimensional parameters were introduced. Scaling of the boundary and free shear layers was accomplished using the usual Reynolds and Froude numbers.

A non-dimensional yield stress parameter was introduced for the evaluation of the existence of a plug layer. The Reynolds versus Froude number plots revealed that in moving from low to high Reynolds numbers, the thick mud-sand deposit that is emplaced by the tail of the flow diminishes in thickness and more sand is deposited from the body. At very high Reynolds numbers however, very little deposit was emplaced by the flow. This may be attributed to the high turbulent energy of the flow at these Reynolds numbers that can help support the heavier grains. Flows with low Reynolds numbers on the other hand, do not have enough turbulent energy to efficiently separate the sand from the clay, and hence, result in very little sand deposition. Consequently, the Reynolds versus Froude number plots from this study suggest the existence of flows within the turbulent regime that can produce massive clean sand deposits.

The factors that contribute to the run-out distance of sediment flows were investigated. It was explained that the run-out distance is greatly influenced by: 1) The rheology of the flowing material, and 2) The ability of the flow to stay close to the equilibrium conditions. Once the flow is initiated, i.e., the static yield stress of the stationary material is surpassed by the gravitational force, its stoppage/freezing is controlled by the dynamic/critical yield stress. Therefore, the difference between the static and critical yield stress has a direct bearing on the run-out distance of sediment flows.

A set of strain controlled rheometry tests were performed on mixtures of kaolinite clay, sand, and water. The results of these tests demonstrated that the dynamic yield stresses of these mixtures are much smaller than their static yield stresses. Consequently, if a suspension of such a mixture, with a given thickness, begins to flow on a certain slope, it will stop only when its thickness is reduced dramatically, or when the slope is decreased considerably. Since mixtures of kaolinite clay, sand, and water are good analogues for the sediment mixtures that are encountered in nature, this result can be generalized to the behavior of natural sediment flows.

It was explained that as a consequence of generalization of Rolle's theorem, all gravity flows reach the equilibrium state at least once during their journey from the proximal to the distal regions. Furthermore, previous research has shown that the presence of cohesive particles in density flows can boost their ability to resist disturbances and promote turbulence damping. Consequently, concentrated clay-laden flows are less prone to the outside disturbances and can therefore stay close to the equilibrium conditions.

To simulate clay-laden flows (i.e., to capture their structure and their run-out distance), a constitutive model which can reproduce the behavior of sediment suspensions is desired. Such a model was constructed based on the bulk rheological behavior of clay-water suspensions. The model takes an indirect microstructural approach to the modeling of thixotropy, in that, it uses a scalar parameter to account for the amount of structure within the material. Since for the materials which exhibit a minimum in their strain controlled flow curves, the structure parameter must be a symmetric function of the strain rate and the stress, the destruction of structure within the material was modeled using the dissipation energy. An expression for the elastic strain of the flowing structure was then derived using the structure model.

To reproduce the behavior of thixotropic materials, the model relies on four empirical parameters. A methodology was presented for obtaining these parameters and power law functions were obtained for their calculations for a limited rest time of 3000 sec-

onds. Finally, different rheometry tests were performed on mixtures with various sediment concentrations to evaluate the performance of the rheological model. Experimental validation of the stress and strain controlled curves predicted by the model revealed that the final set of equations can reproduce the viscosity bifurcation that sediment suspensions may exhibit under a given load. This is important for accurate prediction of the run-out distance and the structures of clay-laden gravity flows, as well as modeling of particle settling velocity inside these flows.

Using the rheological model, the validity of the boundary layer assumptions was investigated. Using these assumptions, the Navier–Stokes equations were then simplified to obtain a reduced set of equations for modeling clay-laden gravity flows. It was observed that the simplified model can capture the C^1 discontinuity that exists at the edge of the boundary layer of clay-rich gravity flows. Furthermore, the steady state solutions of the reduced set of equations demonstrated that clay-laden flows can stay mobile on very low gradients.

SAMENVATTING

Mariene dichtheidsstromen vormen de laatste schakel in de ketting van het transport van sediment van de bron tot de afzetting. Ze zijn het belangrijkste mechanisme voor het transport van sediment van het ondiepe naar het diepe gedeelte van de oceaan. Vanwege hun grote volume, mobiliteit en kracht worden zij gezien als een grote bedreiging voor constructies die zich op zee bevinden. Daarnaast zijn deze stromen ook in staat om tsunamis te veroorzaken die kunnen leiden tot doden en grote schade aan bebouwing op land kunnen aanrichten. De afzettingen van zeer oude dichtheidsstromen bevatten vele reservoirs voor olie en gas. De kwaliteit van deze reservoirs is voornamelijk afhankelijk van de grootte van de korrels en de hoeveelheid klei die zich in de originele dichtheidsstroom bevonden. Door de toename van de bevolking en de stijging van de hoeveelheid energie die per persoon wordt verbruikt is het in de olie en gas industrie belangrijk geworden om de dynamiek van dichtheidsstromen die klei bevatten te kunnen relateren aan de kenmerken van hun afzetting. De hoofdvragen die in dit werk zijn bestudeerd waren: (1) Hoe is de dynamiek van een onderwater dichtheidsstroom gerelateerd aan de afzetting? en, (2) Hoe kunnen deze stromen zich zo ver verplaatsen?
In een poging om de eerste vraag te kunnen beantwoorden, zijn een aantal fluim experimenten gedaan, waarin gebruikt gemaakt werd van sediment met concentraties van 9%, 15% en 21% die bestonden uit een mengsel van zand, silt, klei en kraanwater, die gedaan werden op hellingen van 6°, 8°, en 9.5°, met ontlaadsnelheden van 10 en 15 m^3/h. Na het bestuderen van de vorm van de snelheidsprofielen van de expirmentele stromen werd het duidelijk dat de meest complete anatomie van een onderwater kleirijke dichtheidsstroom bestaat uit drie lagen die verticaal op elkaar zijn gestapeld, 1) een vrije schuif laag, 2) een stop laag en 3) een grens laag. De staat van de stroming in de grens en stop laag van de experimentele stromen werden bepaald door het berekenen van de innerlijke variabel, de zelfvergelijking overweging en de grootte van de viscositeit. Een classificatie voor de klei-rijke dichtheidsstromen werd gebaseerd op de staat van de stroming in deze regios. Volgens de classificatie valt een klei-rijke stroom in een van vier duidelijk afgebakende stroming types: (1) een stop stroom (PF) met een laminaire vrije schuif laag, een stop laag en een laminaire grens laag, (2) een top transitionele stop stroom (TTPF), die een turbulente vrije schuif laag, een stop laag en een laminaire grens laag bevat, (3) een transitionele turbiditeits stroom (TTC), met een turbulente vrije schuif laag, zonder stop laag, met een laminaire grens laag en (4) een volledig turbulente turbiditeits stroom (TC).
Door het bestuderen van de afzetting van de experimentele stromingen werden de specifieke eigenschappen van de afzetting gerelateerd aan de stroming types duidelijk. In het algemeen resulteerden klei-rijke PF stromen in geen afzetting of een afzetting van een dunne bodemlaag van zand. TTPF en TTC stromen veroorzaakten in de meeste gevallen ook een dunne bodemlaag van zand. De bodemlagen van zand afgezet door PF, TTPF en TTC stromen waren bedekt door een mengsel van modder en zand, dat werd

afgezet door het achterste uiteinde van de stroom. TC stromen zorgden voor de afzetting van een dikke massieve bodemlaag van zand, bedekt door een mengsel van modder en zand of een platte laminaire silt laag afgezet door het achterste uiteinde van de stroom.
Om het regime van ieder stroming type te vergelijken met de regimes van analoge grootschalige stromingen in de natuur werden vier non-dimensionale parameters geïntroduceerd. De schaling van de grens en vrije schuif lagen werd gedaan door het gebruik van de gebruikelijke Reynolds en Froude getallen. Het bestaan van de stop laag werd bepaald door het gebruik van een non-dimensionale treksterkte parameter. Grafieken waarin het Reynolds getal tegen het Froude getal werd geplot toonden aan dat als het Reynolds getal stijgt van laag naar hoog, de dikte van het mengsel van modder en zand dat is afgezet door het achterste uiteinde van de stroom afneemt en dat er meer zand wordt afgezet door de stroom. In het geval van een hoog Reynolds getal wordt er weinig materiaal afgezet. Dit kan verklaard worden doordat een stroom met een hoog Reynolds getal hoge trubulente energie bevatten die makkelijker de zware korrels van het zand kunne dragen. Een stroom met een laag Reynolds getal daarentegen, bevat niet genoeg turbulente energie om het zand effectief van de klei te scheiden en daardoor wordt er weinig zand afgezet. De grafieken van het Reynolds getal en Froude getal uit dit werk suggeren als gevolg hiervan dat er stromen bestaan in het turbulente regime die massieve afzettingen van schoon zand kunnen produceren.
De factoren die bijdragen aan de afstand die de sediment stromen kunnen afleggen werden onderzocht. Er werd uitgelegd dat deze afstand sterk wordt beïnvloed door: 1) De reologie van het stromings materiaal en 2) Het vermogen van de stroom om zo veel mogelijk aan de equilibrium voorwaarden te voldoen. Als de stroom eenmaal is gestart, in andere worden als de zwaartekracht groter is geworden dan de statische treksterkte van het stationaire materiaal, dan wordt het stoppen/bevriezen van de stroom bepaald door de dynamische/kritische treksterkte. Als een gevolg kan geconcludeerd worden dat het verschil tussen de statische en kritieke treksterkte direct gerelateerd is aan de afstand die een sediment stroom kan afleggen.
Een set reometrie testen, die bepaald worden door de rek, werden verricht op mengsels van kaoliniet klei, zand en water. De resultaten van deze testen toonden aan dat de dynamische treksterkte van deze mengels veel kleiner zijn dan hun statische tegenhangers. Als gevolg hiervan zal een suspensie van dit soort mengsels met een bepaalde dikte beginnen met stromen van een helling en zal pas stoppen als of de dikte van het mengsel of de grootte van de helling drastisch kleiner wordt. Aangezien mengsels van kaoliniet klei, zand en water goede analogen zijn voor sediment mengsels die in de natuur voorkomen, kan geconlcudeerd worden dat dit resultaat gegeneraliseerd kan worden voor het gedrag van natuurlijke sediment stromen.
Als een gevolg van het generaliseren van het theorema van Rolle, moeten alle dichtheidsstromen minimaal een keer een staat van equilibrium bereiken tijdens hun reis van proximale naar vergelegen regios. Daarnaast heeft eerder onderzoek aangetoond dat de aanwezigheid van samenhangende deeltjes in dichtheidsstromen het vermogen van deze stromen om verstoringen te kunnen weerstaan en turbulentie te verzwakken verhogen. Hieruit kan geconludeerd worden dat geconcentreerde stromen met klei minder gevoelig zijn voor verstoringen van buitenaf en daardoor makkelijker kunnen voldoen aan de voorwaarden voor equilibrium.

Voor het simuleren van stromen met klei (in andere woorden, om hun structuur en afgelegde afstand te bepalen), is er een noodzaak voor een constitutief model, dat het gedrag van sediment suspensies kan simuleren. Zo'n type model werd geconstructeerd, gebaseerd op het bulk reologische gedrag van klei-water suspensies. Het model maakt gebruik van een indirecte microstructurele benadering van het modeleren van de thixotropie, waarmee het gebruik maakt van een scalaire parameter om rekening te houden met de hoeveelheid structuur in het materiaal. Aangezien de structuur parameter een symmetrische functie moet zijn van de reksnelheid en de spanning als het materiaal een minimum toont in de stromen die bepaald worden door de rek, werd de afname van de structuur in het materiaal gemodeleerd door gebruik van het verlies van energie. Een uitdrukking voor de elastische rek van de stromende structuur werd afgeleid met behulp van het structuur model.
Het model is afhankelijk van het gebruik van vier empirische parameters om het gedrag van thixotrope materialen te reproduceren. Een methodologie werd gepresenteerd om deze parameters te verkijgen en machtswetten werden bepaald voor het berekenen van deze parameters voor een gelimiteerde rust tijd van 3000 seconden. Als laatste werden verschillende reometrie testen gedaan op mengsels met verschillende sediment concentraties zodat de prestatie van het reologische model kon worden geëvalueerd. Door het experimenteel valideren van de rek- en spannings-curves, die door het model werden voorspeld, werd een set vergelijkingen bepaald die de splitsing van de viscositieit die sediment kan vertonen onder een bepaalde lading kan voorspellen. Deze vergelijkingen zijn belangrijk voor de nauwkeurige bepaling van de structuur van en de afstand die afgelegd kan worden door klei-rijke dichtheidsstromen. Daarnaast kunnen ze ook gebruikt worden om de snelheid waarmee deeltjes worden afgezet in deze stromen te modeleren.
De nauwkeurigheid van de grens laag aannames werd onderzocht met gebruik van het reologische model. Met behulp van deze aannames werden de Navier-Stokes vergelijkingen versimpeld om een verkleinde set vergelijkingen te verkijgen om klei-rijke dichtheidsstromen te modeleren. Hieruit bleek dat het versimpelde model in staat is om de C^1 discontinuïteit langs de grens van de klei-rijke dischtheidsstroom te bepalen. Daarnaast laten de oplossingen voor de stabiele toestand van de vergelijkingen zien dat de klei-rijke stromen mobiel kunnen blijven op zeer flauwe hellingen.

1

INTRODUCTION

1.1. BACKGROUND

SUBAQUEOUS sediment gravity flows are submarine avalanches of mud, sand, gravel, and rock that carry sediment from the shallower to the deeper parts of the ocean. They are the last stage in the source-to-sink chain and occur due to sea floor failure or the inflow of sediment-laden rivers. Figure 1.1 shows the remnants of the Storegga landslide that occurred ~ 8,150 years ago off the coast of Norway displacing 2500 to 3500 km^3 of sediment as far as 800 km downstream, halfway to Greenland (Bryn et al., 2005; Williams, 2016).

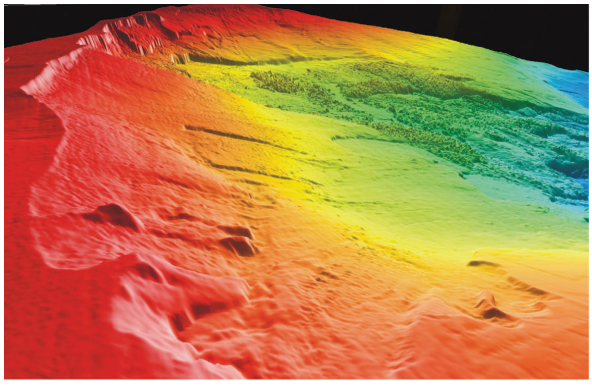

Figure 1.1: Remnants of the Storegga landslide off Norway viewed from the north along its 300-kilometer-long head wall. Image courtesy of Christian Brendt(GEOMAR).

Volumetrically, these flows are the most dominant sediment transport mechanism on

our planet (Talling et al., 2012), with the capability of displacing up to 20,000 km^3 of sediment in one event (Dingle, 1977). They result in the formation of some of the thickest depositional accumulations on Earth in the form of submarine fans, e.g., the Bengal submarine fan with the thickness of 16 km (Curray, 1994) that extends for 2000 km from the mouth of the Ganges and Brahmaputra Rivers to beyond the southern tip of the Indian subcontinent (Covault, 2011; Talling et al., 2013).

The commonly accepted controlling factors for the formation of such depositional systems are tectonic setting, sediment supply, and interplay of climate and sea level (Nelson et al., 2009). The main external controls that determine the type of depositional system, i.e., base of slope aprons, submarine fans, deep sea channels, etc., are size of the continental drainage basin, morphology of the basin, amount and type of sediment, and characteristics of the sediment input points (Nelson et al., 2009).

The study of subaqueous sediment gravity flows can be important because of the industrial, environmental, or human disasters that they can cause. In 1929, an earthquake of magnitude 7.2 on the Richter's scale, at the southern edge of Grand Banks, Newfoundland, set off a large submarine landslide (Heezen & Ewing, 1952), containing 200 km^3 of sediment (Piper et al., 1988). The resulting gravity flow transported mud and sand eastward up to 1000 km at maximum estimated speeds of 60-100 km/h (Heezen & Ewing, 1952). On its way it broke 12 submarine transatlantic telegraph cables and generated a tsunami that killed 28 people (Fine et al., 2005). In tectonically active areas, earthquakes may result in local submarine landslides and produce potentially devastating complex tsunamis in the adjacent coastal regions (Arai et al., 2013; Dawson, 1999; Yeh et al., 1993). In other areas (e.g., Hawaiian islands, Norwegian sea), submarine slides, caused by the oversteepening at the shelf break, may be the dominant source of tsunami generation (Bondevik et al., 1997; Moore & Moore, 1988).

Aside from tsunamis, submarine gravity flows can also cause significant damage to offshore infrastructures (Bruschi et al., 2006; Zakeri et al., 2008). In 2000, two ultra-deep pipeline projects, the Shell Malampaya Pipeline in the Philippines and the Gazprom Blue Stream Pipeline across the Black Sea, recognized subaqueous gravity flows as significant geohazards (Reed et al., 2000). These as well as other offshore projects have revealed the need for assessing the risks that are associated with these flows. The principal difficulty in quantifying such risks are the unpredictable and infrequent nature of these flows (Reed et al., 2000).

Deposits of ancient subaqueous sediment gravity flows are interesting for oil and gas exploration. In 1999 it was estimated that such deposits host approximately 1200 to 1300 oil and gas fields (Stow & Mayall, 2000), many of which are giants (> 500 million barrels oil equivalent). In the time span of 75 years, from 1894 to 1969, approximately 14 billion BOE ultimate recoverable were discovered in 11 turbidite giants. In contrast, within the following 28 years, from 1970 to 1998, an additional 34 billion BOE have been found in 30 giants (Pettingill, 1998), highlighting the increase in the discovery of such oil and gas fields (particularly in offshore settings) in recent years (Nilsen et al., 2008) (Figure 1.2). Although the number of offshore discoveries in the past decade has been impressive, offshore exploration and appraisal has been curtailed somewhat since the economic crash in 2008. Offshore production on the other hand, has seen an increase (IEA, 2017).

Both active and passive-margin settings produce similar turbidite systems (Nelson et al.,

2009) and both settings have had many turbidite giants associated with them. Nevertheless, in recent years Atlantic-type passive margin basins have proven to be the most important ones (Pettingill, 1998). However, while the setting is important, the quality of oil and gas reservoirs is primarily controlled by the grain size and the clay concentration of the ancient flows that deposited the sediments (Amy et al., 2009; Kane & Pontén, 2012; Kane et al., 2017; Porten et al., 2016; Talling et al., 2013).

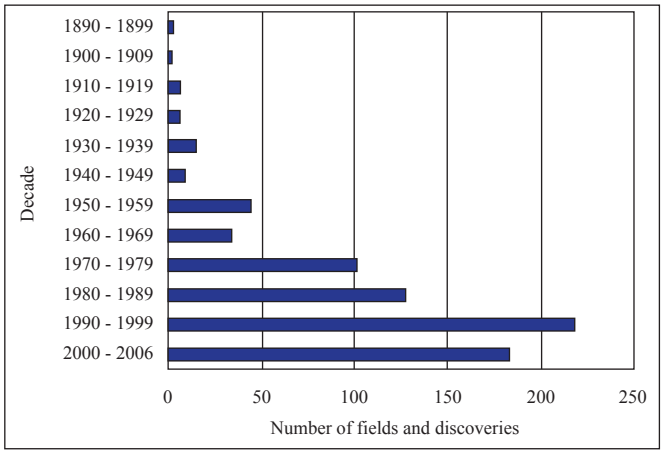

Figure 1.2: Graph of the number of fields and discoveries in deep-water deposits versus the decade in which they were discovered. Note the significant increase starting in the 1970s due to exploration in the North sea and U.S. Gulf of Mexico. Reprinted from Nilsen et al. (2008) with permission from the AAPG, whose permission is required for further use.

The permeabilities and porosities of sandstones are generally a function of their grain size and clay content (Amy et al., 2009; Bennes & Hamon, 2007; Marchand et al., 2015). High-quality sandstones have relatively large grain sizes and low clay contents, resulting in permeabilities that can reach 1 darcy and porosities of up to 35 volume percent. Lower quality sandstones, by contrast, have relatively small grain sizes and high clay contents, resulting in permeabilities lower than 0.1 millidarcy and porosities below 5 volume percent (Amy et al., 2009) [1].

For subaqueous sediment gravity flow deposits, the lithology, the bedding types, and the sedimentary structures within the deposits are to a large extent controlled by the characteristics of the flows that emplaced the sediment. Consequently, to better understand reservoir heterogeneity, which is controlled by these intrinsic rock properties, and in turn better predict production capability, it is important to connect the dynamics of sediment-laden flows to their depositional characteristics. Such connections however, have mostly been established qualitatively through outcrop studies (Felix et al., 2009; Fonnesu et al., 2015; Haughton et al., 2009; Manica, 2012; Talling et al., 2012), and only recently been analyzed numerically (Cantero et al., 2011; Kane et al., 2017).

[1] The presence of clay is not the only factor that can be detrimental to reservoir quality. In fact, clay-poor sandstones have a higher propensity for diagenetic quartz cementation, which also has a deleterious effect on permeability (Porten et al., 2016).

Figure 1.3 shows a classification scheme proposed by Haughton et al. (2009) for the deposits emplaced by flows ranging from cohesive laminar debris flows (resembling those that occurred subsequent to the Storegga landslide), to low-density turbidity currents (quintessentially those occurring in the Bengal submarine fan). Intermediate between these two deposit types are the enigmatic hybrid beds. These comprise a basal clean sandstone overlain by a variety of muddy layers that often contain rip-up clasts, convolutions and laminations that suggest deposition by a debris flow on top of and contemporaneous with the underlying turbidity current. Such deposits have been reported from various locations, e.g., the distal parts of large deep-marine fans in Tanqua Depocenter in the Karoo Basin (Hodgson, 2009; Kane et al., 2017) (Figure 1.4), Beds 58, 78, 82 from the upper Britannia sand-stone members (Barker et al., 2008), and the turbidite beds of the Marnoso Arenacea Formation (Amy et al., 2009).

Based on outcrop observations, the model in Figure 1.3 makes a qualitative, yet insightful, attempt at specifying the flow regimes inside a subaqueous gravity flow and the resulting deposit types. No free shear layer is predicted by the model for laminar debris flows (at their sediment-water interface), and the existence of a bottom sand layer in the hybrid beds is only justified by the presence of a front-running turbidity current.

Although such models have furthered our understanding of the depositional characteristics of subaqueous gravity flows, their lack of a quantified view of the vertical flow structures (based on nondimensional parameters), and their treatment of the complex rheological behavior of clay-water suspensions (Coussot et al., 2002, 2006; Derec et al., 2003), is judged to need further refinement. Accordingly, this study attempts a quantified classification of the flow types, based on a set of nondimensional parameters, and aims to link them to the resulting deposit types.

While flow characteristics control the type of deposit at a given location, how far the sediment is transported from its source area is to a great extent dictated by the rheology of the suspension. Research has shown that, under a given load, clay-rich suspensions exhibit viscosity bifurcation (Coussot et al., 2002; Pignon et al., 1996). This phenomenon, as will be explained in the present study, lies at the root of a question that has baffled researchers for decades, i.e., how do clay-laden flows achieve their mysterious long run-out distances (Embley, 1976; Gee et al., 1999; Jacobi, 1976; Khaldoun et al., 2009; Masson, 1996; Talling et al., 2007)? Consequently, the use of rheological models that can accurately capture the viscosity bifurcation of clay suspensions is imperative for numerical models that aim to predict the run-out distance of clay-laden flows (Hewitt & Balmforth, 2013). This is in contrast to the commonplace numerical practices which often rely on time-independent rheological models, such as the Bingham plastic or the Herschel–Bulkley, for modeling of such flows (Cantelli, 2009; Huang & Garcia, 1998; Jiang & Le Blond, 1993; L. Jing et al., 2018; M. Pastor et al., 2015; Pratson et al., 2000; van Kessel & Kranenburg, 1996). This study builds upon the recent literature on the rheology of clay-suspensions (Mujumdar et al., 2002; Yziquel et al., 1999) in order to develop a new thixotropic constitutive model that can capture the run-out distance of clay-laden gravity flows. This will pave the way for the construction of process-based models that can be used to simulate clay-laden gravity flows.

Due to the complexity of the physical processes acting in a subaqueous sediment flow, and the limited computational resources available, concessions must be made in or-

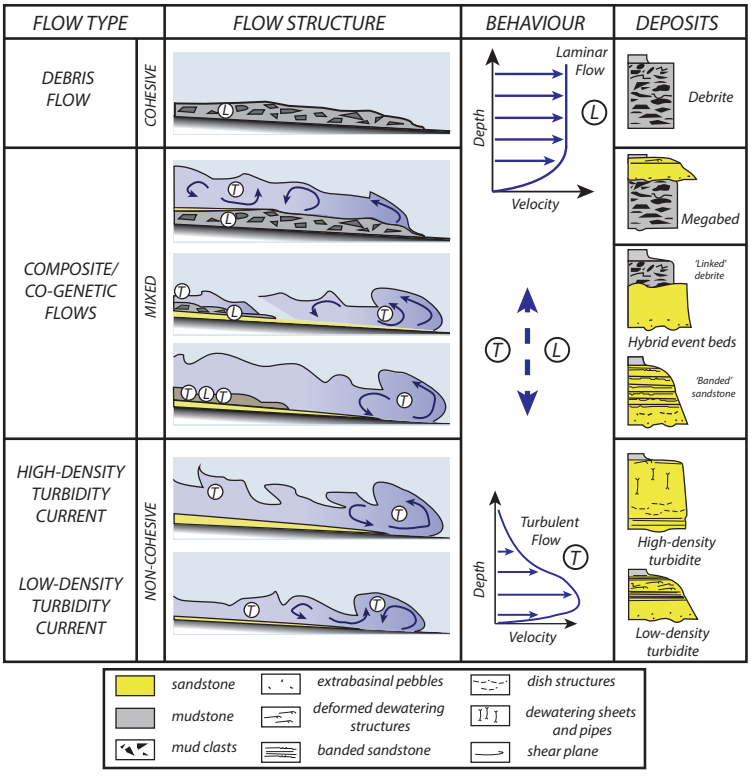

Figure 1.3: Classification scheme of Haughton et al. (2009), depicting the subaqueous sediment gravity flow types and their resulting deposits. In the mixed-cohesion range, hybrid beds are produce by a front-running turbidity current followed by a debris flow.

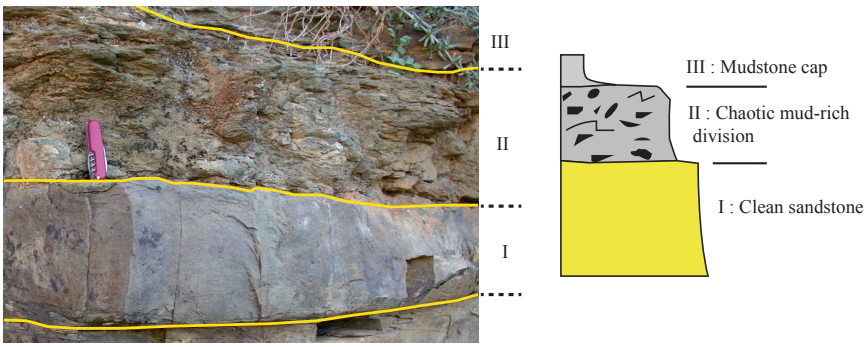

Figure 1.4: Field photo (left) and sedimentary log (right) of a hybrid bed from the Permian Tanqua-Karoo basin in South Africa, displaying a typical vertical sequence containing i) a clean bottom sandstone interval, ii) a middle, muddy sandstone, debrite interval, and iii) an overlying mud cap. Photo courtesy of Stefan Luthi.

der to make the numerical models to simulate these flows tractable. One way in which such complexities can be mitigated, is the use of the well known boundary layer approximation (Groenenberg et al., 2009; Huang & Garcia, 1998; Jiang & Le Blond, 1993; Sequeiros et al., 2009). Nonetheless, the applicability of the boundary layer theory for non-Newtonian fluids is a topic of ongoing research (Acrivos et al., 1960; Anwar et al., 2008; Balmforth et al., 2017; Harris, 1977; Oldroyd, 1947; Rajagopal et al., 1980; Ruckenstein, 1994; Sadeqi et al., 2011). In the present study, the applicability of this approximation is investigated for clay-rich suspensions and a set of equations are presented for modeling clay-rich flows.

1.2. QUESTIONS

The fundamental questions which will be investigated in this study are:

(1) How are the dynamics of subaqueous gravity flows related to their deposits?, and,

(2) Why are these flows able to travel so far?

The first question concerns with the connection between the deposit and the dynamics of the flow emplacing it (Talling et al., 2012). If such a connection can be developed, the flow dynamics can then be captured in the terminology of dimensionless parameters, and the regimes of ancient flows can be reconstructed based on their deposits.
The second question has to do with how far from its source area a gravity flow can travel. There are now numerous accounts of subaqueous gravity flows which have traveled astonishingly long distances on very small gradients (Bryn et al., 2005; Elverhoi et al., 2010; Gee et al., 1999; Legros, 2002; Talling et al., 2007). A good example of such a flow is the one that produced Bed 5 of the Agadir submarine fan in the Atlantic Ocean, offshore Morocco (Talling et al., 2007; Wynn et al., 2002). Based on core data, following initiation, this flow continued to travel through the Agadir canyon and beyond the Agadir basin, reaching as far as the Madeira Abyssal plain, a staggering distance of ~ 1500 km away from the Agadir continental margin, where it was sourced.
The approach to answering these questions involves capturing the transport processes in quantitative relations that can then be used as a foundation for the development of predictive models. This is the path that is followed in this study.

1.3. STUDY APPROACH

Monitoring submarine density flows is difficult because they occur in remote locations on the sea floor and can cover large areas (Talling et al., 2013). Therefore, observing them can be expensive since large research vessels or multiple remotely operated vehicles (ROVs) may be necessary to record an event. Also, their occurrence is infrequent, which makes it difficult to predict when a flow might occur. Finally, such flows are very powerful and are known to damage instruments and moorings, and displace sensors many kilometers from where they were deployed (Arai et al., 2013).
Because of these difficulties, there are only few studies that report such natural events (Arai et al., 2013; Azpiroz-Zabala et al., 2017), and research on subaqueous gravity flows

is for the most part performed through small scale flume experiments (Baker et al., 2017; De Leeuw et al., 2016, 2018; Hermidas et al., 2018) (Chapter 2 of this study) and computer simulations (Groenenberg et al., 2009; Jiang & LeBlond, 1992; Meiburg et al., 2017; Parker et al., 1986; Sequeiros et al., 2009). However, these approaches are not devoid of their own pitfalls.

From an experimental point of view, the major difficulty in studying gravity flows is how small scale flume experiments can be associated with natural large-scale density flows (De Leeuw et al., 2016; Iverson, 1997). While for turbulent low concentration turbidity currents there is some control over the scaling (through the Froude and the Shields/Rouse numbers) (De Leeuw et al., 2016), for clay-rich sediment gravity flows the current understanding of scaling is much more limited (Baker et al., 2017).

Another difficulty with the experimental approaches arises due to the current limitations in terms of measurement accuracy. Since density flows are opaque, velocity measurements are usually performed using Ultrasonic Velocity Profilers (UVPs) which emit sound pulses that bounce off a measurement volume in the density flow and return to a transceiver to be interpreted as a velocity profile (see Chapter 2 for the details of the technique). Due to the large size of the transceiver, the resolution of such measurements is usually much larger than the smallest flow scales. Therefore, in order to determine the regime of the flow from the measurements, one has to resort to large-scale indications, e.g., calculation of the inner variable, or self-similarity of the velocity profile within free shear flows.

Aside from these shortcomings, small-scale experiments provide a wealth of information regarding current hydrodynamics such as the velocity, concentration, turbulence structure, and the sedimentation process (Baas et al., 2011, 2009), for a relatively low cost. Therefore, in this work flume experiments are used to obtain such hydrodynamics information on clay-laden flows. This information is in turn used to assess which non-dimensional groups are sufficient to capture the scaling behavior/regimes of different types of flows.

From a computational point of view, given the large size of natural gravity flows, one of the major difficulties in simulating them has to do with the limitations of computational resources. Consequently, the immensely complex physical phenomena, e.g., particle-particle interaction, particle-fluid interaction, settling, complex non-Newtonian behavior, and turbulence, which drive the evolution of these flows, have to be looked at in a simplified way (e.g., Groenenberg et al., 2009). Yet, such simplifications are by no means trivial and the selection of the appropriate numerical approach is not straightforward.

Another difficulty is the current gap in our understanding of the phenomena involved in these flows. For instance, although a lot of work has been done on the modeling of dilute (Balachandar, 2009; Elghobashi & Truesdell, 1993), and dense (Feng & Michaelides, 2005; Mathiesen et al., 2000; Popken & Cleary, 1999; Vreman et al., 2009) particle-laden flows, to the extent of our knowledge, there is no published work that treats modeling of a large number of electrostatically charged plate-shaped particles (i.e., clays) of various sizes suspended in a fluid. As a result, this field of research has to combine findings from different fields such as: rheology, flows of granular solids, fluid dynamics, and numerical modeling.

Due to such complications, computational efforts of practical interest for mass gravity

flows are generally focused on simplified models of the end members, i.e., (1) debris flows (e.g., Jiang & LeBlond, 1992; Pratson et al., 2000), and (2) turbidity currents (e.g., Groenenberg et al., 2009), in which all the phases (solid as well as fluid) are treated as a single fluid. For debris flows, particle-particle interaction, particle-fluid interaction, and cohesive behavior of the sediment are usually incorporated within the flow equations using a non-Newtonian fluid stress model (Cantelli, 2009; Jiang & LeBlond, 1992), e.g., the Bingham plastic, or the Herschel–Bulkley model. For turbidity currents, the mixture is usually modeled as a Newtonian fluid and Reynolds stresses are incorporated within the flow equations as bed stresses (Groenenberg et al., 2009; Parker et al., 1986).
Aside from their limitations, process-based models can provide a manageable approach for predicting the distribution of sand and clay in submarine depositional systems (Groenenberg, 2007). Furthermore, they can be used to improve our understanding of the role that different parameters play in the evolution of gravity flows in a much easier and faster way compared to experiments. The present study uses such simulations to study the role of clay on the behavior of gravity flows, e.g., their run-out distance, velocity, and boundary layer profile. However, before doing so, a rheological model that can accurately mimic the behavior of clay-laden sediment suspensions is required.
As mentioned previously, at high sediment concentrations, both the effects of particle-fluid and particle-particle interactions become important (Balachandar, 2009). In addition, for clay-rich suspensions, the electrostatic charge of clay particles give rise to the thixotropic behavior of these suspensions (Coussot, 1997). For engineering applications (Dimitriou & McKinley, 2014), these phenomena can be captured through the use of an appropriate rheological model. Therefore, here a rheological model is proposed and experimentally tested to verify its predictions.

1.4. THESIS OUTLINE

Chapter 2 presents the results obtained from a series of flume experiments that was performed on mixtures of sand, silt, clay, and water. The insights gained from these experiments are used to classify clay-laden gravity flows based on their flow structures and to establish quantitative regime diagrams (for the flow types) based on a set of non-dimensional parameters, i.e., the Froude number, the Reynolds number, and the dimensionless yield stress parameter. In Chapter 3, an in depth analysis is performed on the role of clay on the run-out distance of clay-laden flows. This motivates the introduction of a rheological model in Chapter 4 that can accurately capture the effects of clay on the behavior of these flows. In Chapter 5, the applicability of the boundary layer equations for modeling of clay-laden flows is investigated and a simplified version of the Navier-Stokes equations, together with the new rheological model, are used to simulate the evolution of these flows over various gradients.

REFERENCES

Acrivos, A., Shah, M. J., & Petersen, E. E. (1960). Momentum and heat transfer in laminar boundary layer flows of non-Newtonian fluids past external surfaces. *AIChE Journal*, *6*(2), 312–317. doi: 10.1002/aic.690060227

Amy, L. A., Peachey, S. A., Gardiner, A. A., & Talling, P. J. (2009). Prediction of hydrocarbon recovery from turbidite sandstones with linked-debrite facies : Numerical flow-simulation studies. *Marine and Petroleum Geology*, *26*(10), 2032–2043. doi: 10.1016/j.marpetgeo.2009.02.017

Anwar, I., Amin, N., & Pop, I. (2008). Mixed convection boundary layer flow of a viscoelastic fluid over a horizontal circular cylinder. *International Journal of Non-Linear Mechanics*, *43*(9), 814–821. doi: 10.1016/j.ijnonlinmec.2008.04.008

Arai, K., Naruse, H., Miura, R., Kawamura, K., Hino, R., Ito, Y., ... Kasaya, T. (2013). Tsunami-generated turbidity current of the 2011 Tohoku-Oki earthquake. *Geology*, *41*(11), 1195–1198. doi: 10.1130/G34777.1

Azpiroz-Zabala, M., Cartigny, M. J., Talling, P. J., Parsons, D. R., Sumner, E. J., Clare, M. A., ... Pope, E. L. (2017). Newly recognized turbidity current structure can explain prolonged flushing of submarine canyons. *Science Advances*, *3*(10). doi: 10.1126/sciadv.1700200

Baas, J. H., Best, J. L., & Peakall, J. (2011). Depositional processes, bedform development and hybrid bed formation in rapidly decelerated cohesive (mud-sand) sediment flows. *Sedimentology*, *58*, 1953–1987. doi: 10.1111/j.1365-3091.2011.01247.x

Baas, J. H., Best, J. L., Peakall, J., & Wang, M. (2009). A phase diagram for turbulent, transitional and laminar clay suspension flows. *Journal of Sedimentary Research*, *79*, 162–183. doi: 10.2110/jsr.2009.025

Baker, M. L., Baas, J. H., Malarkey, J., Silva Jacinto, R., Craig, M. J., Kane, I. A., & Barker, S. (2017). The Effect of Clay Type On The Properties of Cohesive Sediment Gravity Flows And Their Deposits. *Jornal of Sedimentary Research*, *87*, 1176–1195. doi: 10.2110/jsr.2017.63

Balachandar, S. (2009). A scaling analysis for point-particle approaches to turbulent multiphase flows. *International Journal of Multiphase Flow*, *35*(9), 801–810. doi: 10.1016/j.ijmultiphaseflow.2009.02.013

Balmforth, N. J., Craster, R. V., Hewitt, D. R., Hormozi, S., & Maleki, A. (2017). Viscoplastic boundary layers. *Journal of Fluid Mechanics*, *813*, 929–954. doi: 10.1017/jfm.2016.878

Barker, S. P., Haughton, P. D., McCaffrey, W. D., Archer, S. G., & Hakes, B. (2008). Development of Rheological Heterogeneity in Clay-Rich High-Density Turbidity Currents: Aptian Britannia Sandstone Member, U.K. Continental Shelf. *Journal of Sedimentary Research*, *78*(2), 45–68. doi: 10.2110/jsr.2008.014

Bennes, M., & Hamon, G. (2007). Core Petrophysical Synthesis Carried Out at a Scale of a Basin, Some Examples From Tertiary Offshore Reservoirs. In *Society of core analysts*. Calgary: SCA2007-27.

Bondevik, S., Svendsen, J. I., Johnsen, G., Mangerud, J., & Kaland, P. E. (1997). The Storegga tsunami along the Norwegian coast, its age and run up. *Boreas*, *26*, 29–53. doi: 10.1111/j.1502-3885.1997.tb00649.x

Bruschi, R., Bughi, S., Spinazzè, M., Torselletti, E., & Vitali, L. (2006). Impact of debris flows and turbidity currents on seafloor structures. *Norwegian Journal of Geology*, *86*, 317–336.

Bryn, P., Berg, K., Forsberg, C. F., Solheim, A., & Kvalstad, T. J. (2005). Explaining the Storegga Slide. *Marine and Petroleum Geology*, *22*(1-2 SPEC. ISS.), 11–19. doi: 10.1016/j.marpetgeo.2004.12.003

Cantelli, A. (2009). Uniform Flow of Modified Bingham Fluids in Narrow Cross Sections. *Journal of Hydraulic Engineering*, *135*(8), 640–650. doi: 10.1061/(ASCE)HY.1943-7900.0000092

Cantero, M. I., Cantelli, A., Pirmez, C., Balachandar, S., Mohrig, D., Hickson, T. A., ... Parker, G. (2011). Emplacement of massive turbidites linked to extinction of turbulence in turbidity currents. *Nature Geoscience*, *5*(1), 42–45. doi: 10.1038/ngeo1320

Coussot, P. (1997). *Mudflow Rheology and Dynamics*. Taylor & Francis.

Coussot, P., Nguyen, Q. D., Huynh, H. T., & Bonn, D. (2002). Avalanche behavior in yield stress fluids. *Physical Review Letters*, *88*(17), 1755011–1755014. doi: 10.1103/PhysRevLett.88.175501

Coussot, P., Tabuteau, H., Chateau, X., Tocquer, L., & Ovarlez, G. (2006). Aging and solid or liquid behavior in pastes. *Journal of Rheology*, *50*(6), 975–994. doi: 10.1122/1.2337259

Covault, J. A. (2011). Submarine Fans and Canyon-Channel Systems: A Review of Processes, Products, and Models. *Nature Education Knowledge*, *3*(10).

Curray, J. R. (1994). Sediment volume and mass beneath the Bay of Bengal. *Earth and Planetary Science Letters*, *125*(1-4), 371–383. doi: 10.1016/0012-821X(94)90227-5

Dawson, A. G. (1999). Linking tsunami deposits, submarine slides and offshore earthquakes. *Quaternary International*, *60*(1), 119–126. doi: 10.1016/S1040-6182(99)00011-7

De Leeuw, J., Eggenhuisen, J. T., & Cartigny, M. J. (2016). Morphodynamics of submarine channel inception revealed by new experimental approach. *Nature Communications*, *7*, 1–7. doi: 10.1038/ncomms10886

De Leeuw, J., Eggenhuisen, J. T., & Cartigny, M. J. (2018). Linking submarine channel–levee facies and architecture to flow structure of turbidity currents: insights from flume tank experiments. *Sedimentology*, *65*(3), 931–951. doi: 10.1111/sed.12411

Derec, C., Ducouret, G., Ajdari, A., & Lequeux, F. (2003). Aging and nonlinear rheology in suspensions of polyethylene oxide–protected silica particles. *Physical Review E*, *67*(6), 9. doi: 10.1103/PhysRevE.67.061403

Dimitriou, C. J., & McKinley, G. H. (2014). A comprehensive constitutive law for waxy crude oil: A thixotropic yield stress fluid. *Soft Matter*, *10*(35), 6619–6644. doi: 10.1039/c4sm00578c

Dingle, R. V. (1977). The anatomy of a large submarine slump on a sheared continental margin (SE Africa). *Journal of the Geological Society*, *134*(3), 293–310. doi: 10.1144/gsjgs.134.3.0293

Elghobashi, S., & Truesdell, G. C. (1993). On the two-way interaction between homogeneous turbulence and dispersed solid particles. II. Particle dispersion. *Physics of Fluids*, *5*(7), 1790–1801. doi: 10.1063/1.868254

Elverhoi, A., Breien, H., Blasio, F. V. D., Harbitz, C. B., & Pagliardi, M. (2010). Submarine landslides and the importance of the initial sediment composition for run-out length and final deposit. *Ocean Dynamics*, *60*, 1027–1046. doi: 10.1007/s10236-010-0317-z

Embley, R. W. (1976). New evidence for occurrence of debris flow deposits in the deep sea. *Geology*, *4*(6), 371–374. doi: 10.1130/0091-7613(1976)4<371:NEFOOD>2.0.CO;2

Felix, M., Leszczyński, S., Ślaczka, A., Uchman, A., Amy, L., & Peakall, J. (2009). Field expressions of the transformation of debris flows into turbidity currents, with examples from the Polish Carpathians and the French Maritime Alps. *Marine and Petroleum Geology*, *26*, 2011–2020. doi: 10.1016/j.marpetgeo.2009.02.014

Feng, Z. G., & Michaelides, E. E. (2005). Proteus: A direct forcing method in the simulations of particulate flows. *Journal of Computational Physics*, *202*, 20–51. doi: 10.1016/j.jcp.2004.06.020

Fine, I. V., Rabinovich, A. B., Bornhold, B. D., Thomson, R. E., & Kulikov, E. A. (2005). The Grand Banks landslide-generated tsunami of November 18, 1929: Preliminary analysis and numerical modeling. *Marine Geology*, *215*, 45–57. doi: 10.1016/j.margeo.2004.11.007

Fonnesu, M., Haughton, P., Felletti, F., & Mccaffrey, W. (2015). Short length-scale variability of hybrid event beds and its applied significance. *Marine and Petroleum Geology*, *67*, 583–603. doi: 10.1016/j.marpetgeo.2015.03.028

Gee, M. J. R., Masson, D. G., Watts, A. B., & Allen, P. A. (1999). The Saharan debris flow: an insight into the mechanics of long runout submarine debris flows. *Sedimentology*, *46*, 317–335. doi: 10.1046/j.1365-3091.1999.00215.x

Groenenberg, R. M. (2007). *Process-based modelling of turbidity-current hydrodynamics and sedimentation* (Unpublished doctoral dissertation). TUDelft.

Groenenberg, R. M., Sloff, K., & Weltje, G. J. (2009). A high-resolution 2-DH numerical scheme for process-based modeling of 3-D turbidite fan stratigraphy. *Computers & Geosciences*, *35*, 1686–1700. doi: 10.1016/j.cageo.2009.01.004

Harris, J. (1977). *Rheology and Non-Newtonian Flow*. Longman.

Haughton, P., Davis, C., McCaffrey, W., & Barker, S. (2009). Hybrid sediment gravity flow deposits - Classification, origin and significance. *Marine and Petroleum Geology*, *26*, 1900–1918. doi: 10.1016/j.marpetgeo.2009.02.012

Heezen, B. C., & Ewing, W. M. (1952). Turbidity currents and submarine slumps, and the 1929 Grand Banks [Newfoundland] earthquake. *American Journal of Science*, *250*(12), 849–873. doi: 10.2475/ajs.250.12.849

Hermidas, N., Eggenhuisen, J. T., Silva Jacinto, R., Luthi, S. M., Toth, F., & Pohl, F. (2018). A Classification of Clay-Rich Subaqueous Density Flow Structures. *Journal of Geophysical Research*, *123*(5), 945–966. doi: 10.1002/2017JF004386

Hewitt, D., & Balmforth, N. (2013). Thixotropic gravity currents. *Journal of Fluid Mechanics*, *727*, 56–82. doi: 10.1017/jfm.2013.235

Hodgson, D. M. (2009). Distribution and origin of hybrid beds in sand-rich submarine fans of the Tanqua depocentre , Karoo Basin , South Africa. *Marine and Petroleum Geology*, *26*, 1940–1956. doi: 10.1016/j.marpetgeo.2009.02.011

Huang, X., & Garcia, M. H. (1998). A Herschel–Bulkley model for mud flow down a slope. *Fluid Mechanics*, *374*, 305–333. doi: 10.1017/S0022112098002845

IEA. (2017). *Offshore Energy Outlook* (D. Justus, Ed.). Retrieved from `www.iea.org`

Iverson, R. M. (1997). The physics of debris flows. *Reviews of Geophysics*, *35*, 245–296. doi: 10.1029/97RG00426

Jacobi, R. D. (1976). Sediment slides on the northwestern continental margin of Africa. *Marine Geology*, *22*(3), 157–173. doi: 10.1016/0025-3227(76)90045-1

Jiang, L., & Le Blond, P. H. (1993). Numerical Modelling of an Underwater Bingham Plastic Mud Slide and the Waves which it Generates. *Journal of Geophysical Research*, *98*(C6), 10303–10317. doi: 10.1029/93JC00393

Jiang, L., & LeBlond, P. H. (1992). The coupling of a submarine slide and the surface waves which it generates. *Journal of Geophysical Research*, *97*(C8), 12731–12744. doi: 10.1029/92JC00912

Kane, I. A., & Pontén, A. S. M. (2012). Submarine transitional flow deposits in the Paleogene Gulf of Mexico. *Geology*, *40*(12), 1119–1122. doi: 10.1130/G33410.1

Kane, I. A., Ponten, A. S. M., Vangdal, B., Eggenhuisen, J. T., Hodgson, D. M., & Spychala, Y. T. (2017). The stratigraphic record and processes of turbidity current transformation across deep-marine lobes. *Sedimentology*, *64*, 1236–1273. doi: 10.1111/sed.12346

Khaldoun, A., Moller, P., Fall, A., Wegdam, G., Leeuw, B. D., Me, Y., … Bonn, D. (2009). Quick Clay and Landslides of Clayey Soils. *Physical Review Letters*, *103*(188301), 1–4. doi: 10.1103/PhysRevLett.103.188301

L. Jing, Kwok, C. Y., Leung, Y. F., Zhang, Z., & Dai, L. (2018). Runout Scaling and Deposit Morphology of Rapid Mudflows. *Journal of Geophysical Research: Earth Surface*, *123*(8), 2004–2023. doi: 10.1029/2018JF004667

Legros, F. (2002). The mobility of long-runout landslides. *Geology, Engineering*, *63*, 301–331. doi: 10.1016/S0013-7952(01)00090-4

M. Pastor, Blanc, T., Haddad, B., Morles, M. S., Dutto, P., Stickle, M. M., … Fernández Merodo, J. A. (2015). Depth Averaged Models for Fast Landslide Propagation : Mathematical, Rheological and Numerical Aspects. *Archives of Computational Methods in Engineering*, *22*, 67–104. doi: 10.1007/s11831-014-9110-3

Manica, R. (2012). *Sediment Gravity Flows : Study Based on Experimental Simulations*. InTech. doi: 10.5772/28794

Marchand, A. M. E., Apps, G., Li, W., & Rotzien, J. R. (2015). Depositional processes and impact on reservoir quality in deepwater Paleogene reservoirs , US Gulf of Mexico. *AAPG Bulletin*, *99*(9), 1635–1648. doi: 10.1306/04091514189

Masson, D. G. (1996). Catastrophic collapse of the volcanic island of Hierro 15 ka ago and the history of landslides in the Canary Islands. *Geology*, *24*(3), 231–234. doi: 10.1130/0091-7613(1996)024<0231:CCOTVI>2.3.CO;2

Mathiesen, V., Solberg, T., & Hjertager, B. H. (2000). An experimental and computational study of multiphase flow behavior in a circulating fluidized bed. *International Journal of Multiphase Flow*, *26*, 387–419. doi: 10.1016/S0301-9322(99)00027-0

Meiburg, E., Radhakrishnan, S., & Nasr-azadani, M. (2017). Modeling Gravity and Turbidity Currents : Computational Approaches and Challenges. *Applied Mechanics Reviews*, *67*(4), 1–23. doi: 10.1115/1.4031040

Moore, G. W., & Moore, J. G. (1988). *Large-scale bedforms in boulder gravel produced by giant waves in Hawaii*. doi: 10.1130/SPE229

Mujumdar, A., Beris, A. N., & Metzner, A. B. (2002). Transient phenomena in thixotropic systems. *Journal of Non-Newtonian Fluid Mechanics*, *102*, 157–178. doi: 10.1016/s0377-0257(01)00176-8

Nelson, C. H., Escutia, C., Goldfinger, C., Karabanov, E., Gutierrez-Pastor, J., & Batist, M. D. (2009). *External Controls on Modern Clastic Turbidite Systems: Three Case Studies*. doi: 10.2110/sepmsp.092

Nilsen, T. H., Shew, R. D., Steffens, G. S., & Studlick, J. R. J. (2008). *Atlas of Deep-Water Outcrops*. doi: 10.1306/St561240

Oldroyd, J. G. (1947). Two-dimensional plastic flow of a Bingham solid: A plastic boundary-layer theory for slow motion. *Mathematical Proceedings of the Cambridge Philosophical Society*, *43*(3), 383–395. doi: 10.1017/S0305004100023616

Parker, G., Fukushima, Y., & Pantin, H. M. (1986). Self-accelerating turbidity currents. *J. Fluid Mech.*, *171*, 145–181. doi: 10.1017/S0022112086001404

Pettingill, H. S. (1998). Lessons learned from 43 turbidite giant fields. *Oil and Gas Journal*, *96*(41), 93–95.

Pignon, F., Magnin, A., & Piau, J.-M. (1996). Thixotropic colloidal suspensions and flow curves with minimum: Identification of flow regimes and rheometric consequences. *Journal of Rheology*, *40*, 573–587. doi: 10.1122/1.550759

Piper, D. J. W., Shor, A. N., & Hughes Clarke, J. E. (1988). The 1929 "Grand Banks" earthquake, slump, and turbidity current. In H. E. Clifton (Ed.), *Sedimentologic consequences of convulsive geologic events*. Geological Society of America. doi: 10.1130/SPE229

Popken, L., & Cleary, P. W. (1999). Comparison of Kinetic Theory and Discrete Element Schemes for Modelling Granular Couette Flows. *Journal of Computational Physics*, *155*(1), 1–25. doi: 10.1006/jcph.1999.6292

Porten, K. W., Kane, I. A., Warchoł, M. J., & Southern, S. J. (2016). A Sedimentological Process-Based Approach To Depositional Reservoir Quality of Deep-Marine Sandstones: An Example From the Springar Formation, Northwestern Vøring Basin, Norwegian Sea. *Journal of Sedimentary Research*, *86*(11), 1269–1286. doi: 10.2110/jsr.2016.74

Pratson, L. F., Imran, J., Parker, G., Syvitski, J. P. M., & Hutton, E. (2000, jan). *Debris Flows vs. Turbidity Currents: A Modeling Comparison of Their Dynamics and Deposits* (Vol. 72). American Association of Petroleum Geologists. doi: 10.1306/M72703C6

Rajagopal, K. R., Gupta, A. S., & Wineman, A. S. (1980). On a boundary layer theory for non-Newtonian fluids. *Lett. Appl. Engng Sci.*, *18*, 875–883. doi: 10.1016/0020-7225(80)90035-X

Reed, C. W., Niedoroda, A. W., Foristall, G. Z., & Mullee, J. E. (2000). Mass-gravity flows pose major hazards for deepwater pipelines. *Oil & Gas Journal*, *98*(47), 78–85.

Ruckenstein, E. (1994). Thermal and Diffusion Boundary Layers in Viscoelastic Flows. *Industrial & Engineering Chemistry Research*, *33*(10), 2331–2335. doi: 10.1021/ie00034a011

Sadeqi, S., Khabazi, N., & Sadeghy, K. (2011). Blasius flow of thixotropic fluids: A numerical study. *Communications in Nonlinear Science and Numerical Simulation*, *16*(2), 711–721. doi: 10.1016/j.cnsns.2010.05.009

Sequeiros, O. E., Cantelli, A., Viparelli, E., White, J. D., Garcí, M. H., & Parker, G. (2009). Modeling turbidity currents with nonuniform sediment and reverse buoyancy. *Water Resources Research*, *45*(6), 1–28. doi: 10.1029/2008WR007422

Stow, D. A. V., & Mayall, M. (2000). Deep-water sedimentary systems: New models for the 21st century. *Marine and Petroleum Geology*, *17*(2), 125–135. doi: 10.1016/S0264-8172(99)00064-1

Talling, P. J., Masson, D. G., Sumner, E. J., & Malgesini, G. (2012). Subaqueous sediment density flows: Depositional processes and deposit types. *Sedimentology*, *59*, 1937–2003. doi: 10.1111/j.1365-3091.2012.01353.x

Talling, P. J., Paull, C. K., & Piper, D. J. (2013). How are subaqueous sediment density flows triggered, what is their internal structure and how does it evolve? Direct observations from monitoring of active flows. *Earth-Science Reviews*, *125*, 244–287. doi: 10.1016/j.earscirev.2013.07.005

Talling, P. J., Wynn, R. B., Masson, D. G., Frenz, M., Cronin, B. T., Schiebel, R., … Amy, L. A. (2007, nov). Onset of submarine debris flow deposition far from original giant landslide. *Nature*, *450*, 541–544. doi: 10.1038/nature06313

van Kessel, T., & Kranenburg, C. (1996). Gravity Current of Fluid Mud on Sloping Bed. *Journal of Hydraulic Engineering*, *122*(12), 710–717. doi: 10.1061/(ASCE)0733-9429(1996)122:12(710)

Vreman, B., Geurts, B. J., Deen, N. G., Kuipers, J. A. M., & Kuerten, J. G. M. (2009). Two- and four-way coupled euler-lagrangian large-eddy simulation of turbulent particle-laden channel flow. *Flow, Turbulence and Combustion*, *82*(1), 47–71. doi: 10.1007/s10494-008-9173-z

Williams, S. C. P. (2016). Skimming the surface of underwater landslides. *Proceedings of the National Academy of Sciences*, *113*(7), 1675–1678. doi: 10.1073/pnas1524012113

Wynn, R. B., Weaver, P. P. E., Masson, D. G., & Stow, D. a. V. (2002). Turbidite depositional architecture across three interconnected deep-water basins on the north-west African margin. *Sedimentology*, *49*(4), 669–695. doi: 10.1046/j.1365-3091.2002.00471.x

Yeh, H., Imamura, F., Synolakis, C., Tsuji, Y., Liu, P., & Shi, S. (1993). The Flores Island tsunamis. *Eos, Transactions American Geophysical Union*, *74*(33), 369–373. doi: 10.1029/93EO00381

Yziquel, F., Carreau, P. J., Moan, M., & Tanguy, P. A. (1999). Rheological modeling of concentrated colloidal suspensions. *Journal of Non-Newtonian Fluid Mechanics*, *86*, 133–155. doi: 10.1016/S0377-0257(98)00206-7

Zakeri, A., Hoeg, K., Nadim, F., Uio, O., & Centre, I. (2008). Submarine Debris Flow Impact on Pipelines : Drag Forces , Mitigation , and Control. In *Offshore technology conference*. Houston.

2

CLASSIFICATION OF CLAY-LADEN SUBAQUEOUS DENSITY FLOW STRUCTURES

This chapter presents a classification for subaqueous clay-laden sediment gravity flows. A series of laboratory flume experiments were performed using 9%, 15%, *and* 21% *sediment mixture concentrations composed of sand, silt, clay, and tap water, on varying bed slopes of* 6°, 8° *and* 9.5°, *and with discharge rates of* 10 m^3/h *and* 15 m^3/h. *In addition to the characteristics of the boundary and plug layers, which have been previously used for the classification of open-channel clay-laden flows, the newly presented classification also incorporates the treatment of the free shear layer. The flow states within the boundary and free shear layers were constrained using the inherent overall features of turbulent and laminar flows, e.g., calculation of the inner variable, self-similarity considerations, and the magnitude of the apparent viscosity. Based on the experimental observations four flow types were recognized: 1) a clay-rich plug flow (PF) with a laminar free shear layer, a plug layer, and a laminar boundary layer, 2) a top transitional plug flow (TTPF) containing a turbulent free shear layer, a plug layer, and a laminar boundary layer, 3) a transitional turbidity current (TTC) with a turbulent free shear layer, no plug layer, and a laminar boundary layer, and, 4) a fully turbulent turbidity current (TC). A connection between the emplaced deposits and the relevant flow types is drawn and it is shown that a Froude number, two Reynolds numbers, and a dimensionless yield stress parameter are sufficient to associate an experimental flow type with a natural large-scale density flow.*

2.1. INTRODUCTION

IF initiated by a triggering event such as a sediment slide, a subaqueous density flow goes through a wide range of transformations in both space and time (Talling et al.,

This chapter has been published in the Journal of Geophysical Research 123(5), 945-966 (2018).

2007). In its initial state, such a flow is often composed of blocky material which disintegrates due to shearing and pressure (Schwarz, 1982). The resulting flow, which can be classified as debris flow, is laminar, dense, and cohesive (Talling et al., 2012).

As the flow moves towards equilibrium, depending on its boundary conditions, it may speed up or slow down, deposit sediment, erode the substrate, contract in the form of the tail approaching the head, stretch, entrain water and grow in height, or dewater and collapse. If the rate of the combined effects of sediment incorporation due to erosion, contraction, and dewatering of the flow is higher than those of sediment deposition, stretching, and water entrainment, the flow becomes denser, and if it is clay-bearing, more cohesive. The velocity profile of such a flow transforms towards that of a plug flow, which is dense and laminar within the boundary and free shear layers and whose primary sediment support mechanism is not turbulence. On the contrary, if the rate of deposition, stretching, and water entrainment is higher, the flow becomes more dilute and less cohesive. The velocity profile of such a flow transforms towards that of a turbidity current. Flows between these two end members are known as transitional flows (Haughton et al., 2009; Kane & Pontén, 2012; Talling et al., 2012).

Several attempts have been made in the past to connect structures of transitional density flows to their resulting deposits. Felix et al. (2009) presented a generic classification scheme for flows transitional between a concentrated debris flow and a high density turbidity current. In their work they connect five distinct flow types with their possible resulting deposit based on concentration and rheological properties of the fluid. The structures of the flows producing these deposits however, are not fully explored or quantified in their work. In this work we focus on the flow structures and aim to connect the resulting deposits to the flow structures. Baas et al. (2009) studied turbulent properties of transitional flows and presented a phase diagram for clay-laden open-channel flows on the basis of the balance between turbulent and cohesive forces. Following this work, they then studied the behavior of rapidly decelerating flows of mixtures of sand, silt, and clay and the influence of variations in clay concentration on the bed forms and the stratification produced (Baas et al., 2011). Sumner et al. (2009) used flume experiments to investigate linked debrite-turbidite deposits of waning density flows composed of a fixed amount of sand and variable mud fractions. In their work, they recognized four different deposit types which they then connected to the phase diagram of Baas et al. (2009). The contributions following from the work of Baas et al. (2009) illuminate depositional types as related to flow structure for clay-rich open-channel flows. Such a classification does not exist for clay-rich subaqueous density flows. While the flow structure of turbidity currents is relatively well understood (Altinakar et al., 1996; Islam & Imran, 2010; Kneller et al., 1999; Meiburg & Kneller, 2010), the flow structure of subaqueous clay-rich density currents that are thought to deposit hybrid beds have not been comprehensively documented yet (Felix et al., 2009). Manica (2012) performed a series of lock-exchange experiments on sediment gravity flows based on which six flow types were recognized according to the hydrodynamic, depositional, and rheological properties of the flows. He then connected the spatial evolution of these flows and their deposits to the flow types. The work of Manica (2012), presents an in-depth analysis of the effects of sediment concentration and rheological effects of clay on the deposition processes. However, it does not provide a quantified view of the vertical flow structures based on non-dimensional

parameters. Here we aim to expand on this front.
The aims of this chapter are threefold: 1) To present a classification of flow types intermediate between end-member debris flows and turbidity currents based on observed flow structures; 2) To link the flow types to their typical deposits; and 3) To present a set of scaling parameters that can be used to relate small-scale flume experiments to the large-scale natural flows.
To this end, a series of experimental runs were performed on mixtures composed of 1) sand, silt, clay, and water and, 2) sand, clay, and water. During the experiments the sediment concentration of the mixture, the bed slope, and the discharge rate were systematically varied. Velocity data was obtained using two Ultrasonic Doppler Velocity probes and rheometry measurements were performed on the mixtures to obtain apparent viscosity data. Three regions were then recognized within the velocity profile of a density flow. Reynolds number, Froude number, and yield stress were calculated in order to classify and scale subaqueous density flows. The resulting deposit from each experimental run was analyzed to make the connection to the types of flows.

2.2. METHODS

In section 2.2.1 the experimental setup is explained. In section 2.2.2, three length scales are introduced which are used in section 2.2.7 to define a set of dimensionless parameters. In order to evaluate the regime of the flow within the boundary and free shear layers, sections 2.2.3-2.2.6 present the procedures that are followed for the various necessary parametrizations of the results. Finally, for scaling purposes, a Froude number, two Reynolds numbers for the boundary and free shear layers, and a dimensionless yield stress parameter are defined in section 2.2.7.

2.2.1. EXPERIMENTAL SETUP

Experiments were performed in a 3.7 m long, 0.22 m wide, and 0.5 m high flume with glass side walls and an adjustable slope located at the Eurotank Laboratory at Utrecht University (Figure 2.1). To mitigate back flow, a wooden board was used to split the flume into two sections of 0.10 m wide (top view in Figure 2.1). Quartz sand from Sibelco with a median diameter of 150 μm was glued on the non-erodible bed to provide roughness.

Glass granules obtained from Kuhmichel Abrasiv B.V. in the Netherlands with a median diameter of 46 μm was used as silt material and Crown Kaolinite clay from ActiveMinerals International, with a median diameter of 0.18 μm was used as clay material (Figure 2.2). The same quartz sand material as the one glued to the bed was used to prepare the mixtures.
In order to incorporate the influences of sediment composition in this study, fourteen runs were performed with sand, clay, and tap water and fifteen runs were performed with sand, silt, clay, and tap water. The sediment volume concentration was varied between 9%, 15%, and 21% and contained 2/3 sand and 1/3 clay for the runs without silt and 1/3 sand, 1/3 silt, and 1/3 clay, for the runs including silt. An overview of the runs is given in Table 2.1.

The data from some of the runs were omitted from the data set. Runs 5 and 6 failed

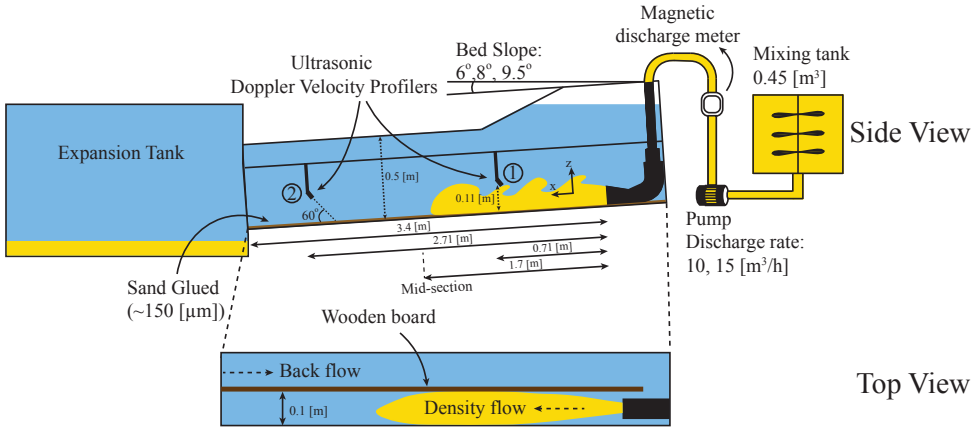

Figure 2.1: Sketch of the flume at the Eurotank Laboratory of Utrecht University

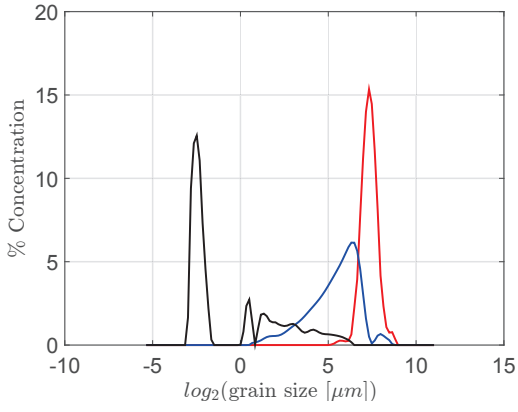

Figure 2.2: Grain size distribution of silt (blue), sand (red), and clay (black), obtained from Malvern grain size analysis.

due to technical issues and were omitted from the data set. For run 14, a mixture with a 30% sediment concentration was pumped onto a 9.5° bed slope. Upon entering the flume the sediment deposited immediately and, therefore, no flow velocity could be measured. The data for this run was therefore omitted from the data set.

Some mixtures had different pH levels compared to others. Runs containing silt were basic and had a pH close to 10. This resulted in less flocculation for these runs compared to those without silt, which had a pH of approximately 5.

Before the experiments the mixture was stirred for 30 minutes to 2 hours in a 0.45 m^3 mixing tank and the flume was filled with tap water. The sediment mixture was then pumped into the flume. The discharge rate was monitored by a magnetic discharge meter (Krohne Optiflux 2300) and regulated to 10 or 15 m^3/h by a Labview control system. Upon exiting the flume the sediment mixture flowed into an expansion tank (Figure 2.1)

Table 2.1: Slope, discharge rate, and sediment concentration of each run. Subscripts 1 and 2 signify information at the location of UVP1 and UVP2.

Run No.	Slope	Discharge rate $\frac{m^3}{h}$	Sed. Vol.%	Silt in Mix. Vol.%	Fr_1	Fr_2	$Re_{\mu,BL1}$	$Re_{\mu,BL2}$	$Re_{\mu,FSL1}$	$Re_{\mu,FSL2}$
1	6°	10	15	5	1	1.3	217	57	781	109
2	6°	10	15	0	0.7	0.6	52	34	106	27
3	9.5°	10	15	0	0.9	1.2	24	31	77	92
4	8°	10	15	0	1	1.2	95	123	316	216
7	8°	15	15	0	1.3	1.4	367	140	1806	770
8	9.5°	15	9	0	1	1.1	1944	2288	20112	15810
9	6°	10	9	0	0.7	1	2150	1325	14758	4811
10	9.5°	15	15	0	1.2	1.5	305	81	1788	539
11	6°	15	15	0	1.4	1.2	504	86	1792	271
12	6°	15	9	0	0.9	1	1307	2259	10350	13100
13	8°	15	21	0	1	0.9	31	21	156	36
15	9.5°	10	21	0	0.9	1	22	23	40	27
16	8°	10	21	7	1	1.3	23	22	51	40
17	9.5°	10	21	7	1.5	2	38	32	103	59
18	6°	10	21	7	1	1.1	42	21	116	23
19	8°	10	15	5	1.1	1.4	160	145	685	493
20	9.5°	10	15	5	1.2	1.4	131	218	633	1224
21	6°	15	15	5	1.1	1.2	295	83	2260	298
22	8°	15	15	5	1.2	1.3	322	74	2225	480
23	9.5°	15	15	5	1.2	1.5	140	65	888	392
24	6°	15	21	7	1.3	1.2	53	48	300	84
25	6°	10	9	3	0.8	1	2179	2205	10216	7806
26	6°	15	9	3	1	0.9	2287	2938	16449	14220
27	9.5°	15	21	7	1.4	1.8	88	48	566	190
28	8°	15	21	7	1.3	1.4	47	21	193	70
29	8°	10	21	0	0.6	0.5	12	8	22	8
30	9.5°	15	21	0	1.1	1.1	55	46	240	94
31	9.5°	10	9	3	1	1.2	1937	3178	14319	21328
32	9.5°	10	9	0	0.8	1.3	1891	1919	14472	12710

such that reflections had a minimal impact on the experimental measurements.
To obtain velocity profile measurements, two Ultrasonic Doppler Velocity Profiler probes (UVP Duo MX, 1 MHz) were placed at 0.7 m and 2.7 m distance from the inlet, at a height of 0.11 m above the bed, and with an angle of 60° to the bed, facing upstream (Figure 2.1). Each probe emitted and received 32 bursts, followed by a dead time of approximately 10 ms before the burst sequence of the second probe. The duration of each burst was 5 μs. The time resolution of a burst sequence was 0.16 ms. The time between successive burst sequences of a single probe was 0.22 s. The thickness of a measurement bin along the z direction was 0.64 mm. The velocities parallel to the bed were calculated from the measurements and used to obtain a velocity profile. The total duration of each flume measurement was approximately one minute and was long enough to obtain a steady state velocity profile.

2.2.2. LENGTH SCALE DEFINITIONS

Clay-rich sediment density flows consist of three vertically stacked regions: (1) a free shear layer at the top, (2) a plug layer and, (3) a basal boundary layer. Therefore, three length scales, δ_{FSL}, δ_{PL}, and δ_{BL} can be attributed to the sizes of the free shear layer, the thickness of the plug layer, and the thickness of the boundary layer, respectively. These are depicted in Figure 2.3a. The boundary layer thickness, δ_{BL}, is defined as the distance from the bed to the position where the time-averaged velocity, $\bar{u}$, becomes approximately equal to 0.99 $\bar{u}_{max}$, where, $\bar{u}_{max}$, is the maximum time-averaged velocity

above the bed. The plug layer thickness, δ_{PL}, is defined as the distance above the boundary layer to the position where the time-averaged velocity first falls below approximately 0.99 $\bar{u}_{max}$ (Figure 2.3a). The free shear layer thickness is defined as the distance from the top of the plug layer to the point of maximum vorticity, called the inflection point. The flow height, H, is defined as the distance from the bed to the inflection point (Figure 2.3a).

In order to obtain the position of the bed, i.e., the position of the top of the deposit emplaced over the bottom of the tank, the time-averaged velocity ($\bar{u}$) profile data obtained from the transceiver was used to pinpoint the position of the minimum velocity coinciding with approximately the distance of the UVP from the bed, as demonstrated for a typical velocity profile result in Figure 2.4. The profile recorded below the bed position in Figure 2.4 is due to the data received after the signal is reflected off the bed. Close to the bed, the measurement volume spans from the bed to a certain location above the bed. Consequently, within this measurement volume the velocity of the fluid varies from zero, at the bed, to a non-zero value, above the bed. Since post-processing is performed on the velocity recordings made from this finite measurement volume in the vicinity of the bed, the resulting velocity at the bed is not assigned a zero value.

The position of the inflection point was obtained by first linearly interpolating the velocity data over approximately seventeen uniformly spaced elements (for some runs different number of elements resulted in a better accuracy) and then differentiating the resulting curve to obtain a shear rate profile (Figure 2.3b). The element with the minimum shear rate was then associated with the inflection point. For computational purposes, the position of the top of the element corresponding to the inflection point was used as the vertical position of the inflection point (Figure 2.3b). The accuracy of pinpointing the vertical position of the inflection point from this process was approximately 0.006 m, i.e., each element spanned a vertical distance of approximately 0.006 m.

For some of the runs the velocity data extended above the position of the UVP, therefore, logarithmic extrapolation was used to estimate the position where the time average velocity first became zero in the top part of the flow (Figure 2.3a). The distance from the top of the plug layer to the position where the time-averaged velocity is approximated to be zero is called h (Figure 2.3a).

2.2.3. LAMINAR APPARENT VISCOSITY MEASUREMENTS

The apparent viscosity of the flow can carry important information regarding the regime of the flow. In this section we present the procedure that was followed for obtaining laminar apparent viscosity data for the sediment mixtures. This laminar apparent viscosity data will be used 1) to evaluate the regime of the flow and, 2) to define dimensionless parameters in section 2.2.7.

The occurrence of clay in a density flow can greatly influence its behavior (Pratson et al., 2000). The fluid in clay-laden flows is thixotropic, viscoelastic, and shear thinning (Coussot, 1997). For such fluids, in steady state, the relation between shear stress, τ, and shear rate can be expressed as,

$$\tau = \mu(C, \dot{\gamma})\dot{\gamma}, \tag{2.1}$$

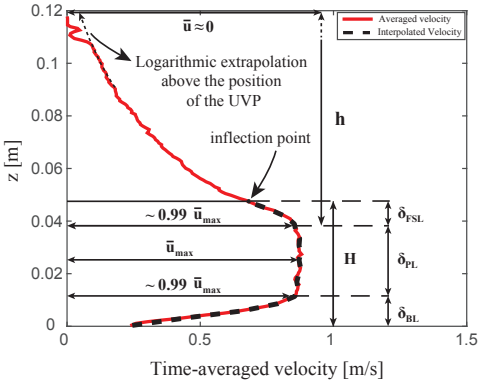

(a) Length scale definitions.

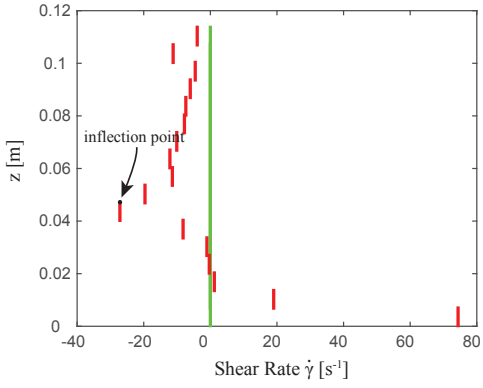

(b) Shear rate profile. The green line indicates zero shear rate.

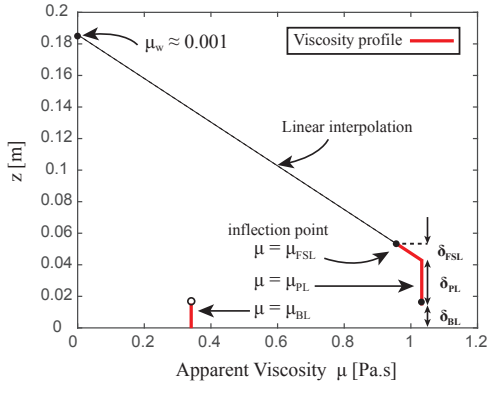

(c) Viscosity profile.

Figure 2.3: A representative example of experimental measurements: (a) Free shear layer, plug layer, and boundary layer length scales, (b) shear rate profile, and (c) viscosity profile, for run 15. The dotted black line in (a) depicts the interpolated velocity data. The boundary layer viscosity, μ_{BL}, and the plug layer viscosity, μ_{PL}, in (c) were obtained by averaging the viscosity data within the boundary and plug layers. Within the free shear layer the viscosity was obtained by linear interpolation, as will be explained in section 2.2.3.

where, μ is the apparent viscosity, C is the concentration, and $\dot{\gamma}$ is the shear rate.
The apparent viscosities of the mixtures used in the experiments were measured in a rheometer. Mixtures containing the same sediment composition and concentration as presented in Table 2.1 were prepared. Stress controlled tests were performed on these mixtures using an MRC302 Anton Paar rheometer and the apparent viscosity was measured at various shear rates (Figure 2.5). In order to prolong the settling duration the concentric cylinder geometry was used. The duration of the measurement for obtaining each data point was chosen to be 10 seconds and was considered long enough to ensure near equilibrium conditions. For shear rates lower than approximately $10^{-3} s^{-1}$, the precision of the measurements was low for mixtures of 15% and 21% sediment concen-

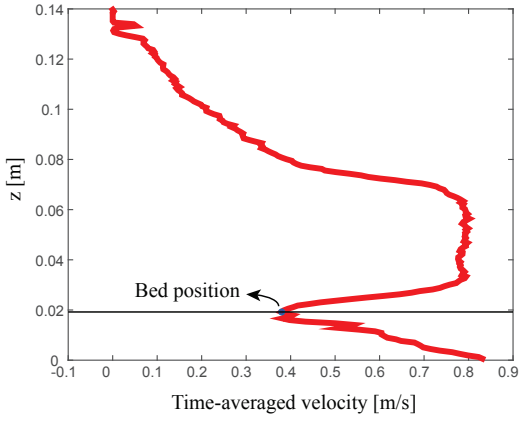

Figure 2.4: Bed position obtained from the UVP data of run 15.

tration (Figure 2.5). Therefore, for computational purposes only apparent viscosity data obtained for shear rates between $10^{-3}s^{-1}$ and approximately $100s^{-1}$ were considered. Figure 2.5 shows that, in general, sand-silt-clay-water mixtures had lower apparent viscosities compared to the sand-clay-water mixtures.

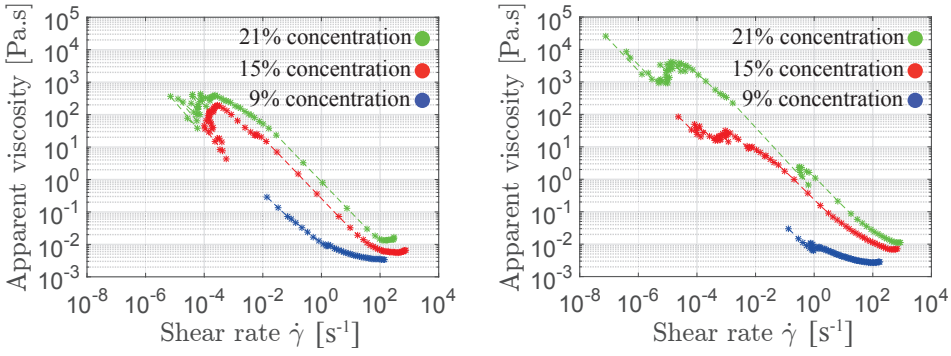

(a) Apparent viscosity versus shear rate data for sand-clay-water mixtures.

(b) Apparent viscosity versus shear rate data for sand-silt-clay-water mixtures.

Figure 2.5: Apparent viscosity versus shear rate data obtained from stress controlled tests for (a) sand-clay-water mixtures and, (b) sand-silt-clay-water mixtures. Mixtures with 21% sediment concentration are shown in green, those with 15% sediment concentration are shown in red, and those with 9% sediment concentration are shown in blue.

Since the head of the flow was not the subject of the current study, the effects of hydroplaning were neglected and the density of the fluid within the boundary and plug layers was assumed to be equal to that of the fluid within the mixing tank (Mohrig et al., 1998). Therefore, it was assumed that the apparent viscosity measured with the rheometer corresponds to the apparent viscosity of the fluid within the boundary and plug layers

and varies only as a function of the shear rate at these locations (Equation (2.1)). The apparent viscosities corresponding to the shear rates obtained from the velocity data, as in Figure 2.3b, were then obtained from the rheometer measurements by interpolating the apparent viscosity data for different shear rates and reading off the corresponding values. The number of elements used for interpolating the shear rate data were therefore accordingly adjusted for some runs to avoid an element having a shear rate lower than $10^{-3}s^{-1}$ within for example the plug layer region (Figure 2.3b). Consequently, for every shear rate profile obtained from velocity data, an apparent viscosity profile was obtained for the boundary and the plug layers. The apparent viscosity profile was then averaged within these two regions to obtain a mean viscosity for the boundary layer, here referred to as μ_{BL}, and a mean viscosity for the plug layer, here referred to as μ_{PL}.
Within the free shear layer and above the inflection point (specified as h in Figure 2.3a) the apparent viscosity varies between μ_{PL} at the plug, and that of water, $\mu_w = 0.001\ Pa.s$, at the assumed height of h. Therefore, the following simple linear approximation was used to obtain the value of the apparent viscosity at the inflection point,

$$\mu_{FSL} = \mu_w + \frac{(\mu_{PL} - \mu_w)(h - \delta_{FSL})}{h}. \tag{2.2}$$

Figure 2.3c depicts an example viscosity profile obtained for run 15. Since viscometric flows are laminar, the apparent viscosities obtained following the procedure described in this section are referred to as laminar apparent viscosities.

2.2.4. SHEAR STRESS PROFILE

We extend the common definition of the shear stress profile of density flows to density flows containing a plug layer. This stress profile together with the shear rate profile (Figure 2.3b) are used to obtain a compounded apparent viscosity in section 2.2.5.
For viscoelastic fluids, the shear stress is composed of a viscous-fluid part and an elastic-solid part (Tanner, 2000). While the viscous-fluid part is dependent on viscosity and velocity gradient, the elastic-solid part is dependent on the strain and elastic modulus and accounts for the solid deformations that the material undergoes. Within the boundary and free shear layers, the viscous-fluid part dominates. In the plug layer on the other hand, the elastic-solid part prevails. Therefore, in the plug layer the shear stress is predominantly related to the solid deformation of the suspension and not with the viscosity and the velocity gradient.
For a steady flow in equilibrium with only gravity and shear stress forces, the momentum equation can be written as,

$$(\rho - \rho_w)\, g \sin\theta = \frac{d\tau}{dz}, \tag{2.3}$$

where, ρ and ρ_w are fluid and water densities, and θ is the bed slope. Integrating this equation from the bed to the mid point of the plug layer, where the stress is assumed to be zero, yields,

$$(\rho - \rho_w)\, g \sin\theta\, (\delta_{BL} + \delta_{PL}/2) = -\tau_b, \tag{2.4}$$

where, τ_b is the stress at the bed.
The top and bottom of the plug layer are the two locations where the shear stress is equal to the yield strength of the plug. Within the boundary layer, the shear stress therefore varies between τ_b at the bed and the yield stress, τ_y, of the plug layer at the height $z = \delta_{BL}$, with $z = 0$ at the bed. Within the top part of the flow, the shear stress varies between the yield stress, τ_y, of the plug layer at $z = \delta_{BL} + \delta_{PL}$, and zero at $z = \delta_{BL} + \delta_{PL} + h$.
Using linear approximation, for every run a stress profile can be estimated (Figure 2.6b). Within this profile τ_H is the approximated stress at the inflection point, τ_y is the fluid yield stress, and $\Delta\tau = |\tau_y| + |\tau_b|$.

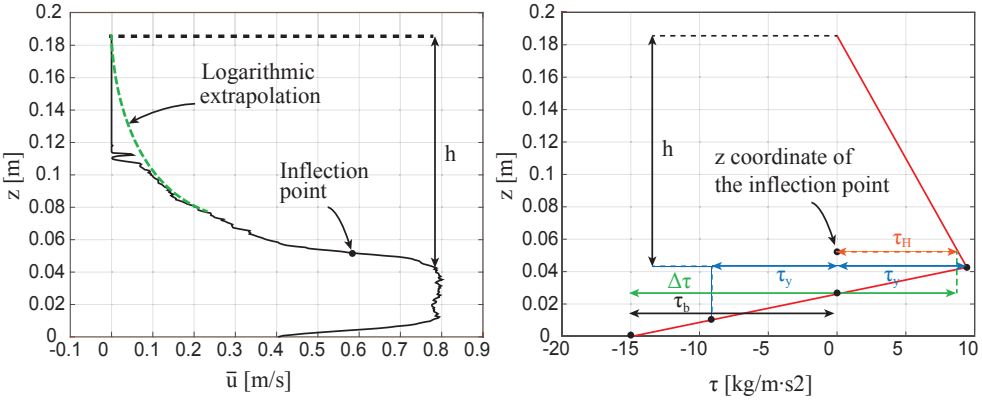

(a) Velocity versus flow height.

(b) Stress versus flow height.

Figure 2.6: Representative example of velocity and stress profiles: (a) Velocity profile and, (b) stress profile of run 15. The dashed green line in (a) shows the logarithmic extrapolation of the velocity profile above the location of the ultrasonic doppler velocity profiler. The shear stress at the inflection point, τ_H, the yield stress of the fluid, τ_y, the shear stress at the bed, τ_b, and $\Delta\tau$, are depicted in (b).

2.2.5. COMPOUNDED APPARENT VISCOSITY

Since the stress and the shear rate profiles described in sections 2.2.4 and 2.2.2 were derived using velocity data obtained from the UVP probe measurements, they contain the information regarding the regimes of the flows. In this section this information is used to introduce the notion of a compounded apparent viscosity.
The viscous-fluid and elastic-solid behaviors of a viscoelastic fluid are encapsulated within the laminar apparent viscosity data obtained from the rheometer. However, within the boundary or the free shear layer, the flow may become unsteady or even turbulent. Therefore, the apparent viscosity maybe considered to be a function of the shear strain, γ, as well as the concentration and the shear rate. For a fluid flowing within the turbulent regime, the flow parameters can be decomposed into a time-averaged quantity denoted by $\bar{}$, and a fluctuating quantity denoted by $'$. Then using Taylor expansion, the apparent viscosity can be written as,

$$\mu(\bar{C}+C',\bar{\gamma}+\gamma',\dot{\bar{\gamma}}+\dot{\gamma}') = \mu(\bar{C},\bar{\gamma},\dot{\bar{\gamma}}) + \frac{\partial\mu}{\partial\bar{C}}C' + \frac{\partial\mu}{\partial\bar{\gamma}}\gamma' + \frac{\partial\mu}{\partial\dot{\bar{\gamma}}}\dot{\gamma}' + H.O.T., \tag{2.5}$$

Inserting equation (2.5) in (2.1) and collecting terms yields,

$$\tau = \mu(\bar{C}+C',\bar{\gamma}+\gamma',\bar{\dot{\gamma}}+\dot{\gamma}')(\bar{\dot{\gamma}}+\dot{\gamma}') = \overbrace{\mu(\bar{C},\bar{\gamma},\bar{\dot{\gamma}})\bar{\dot{\gamma}}}^{\bar{\tau}} + \overbrace{\left(\mu(\bar{C},\bar{\gamma},\bar{\dot{\gamma}})\dot{\gamma}' + \frac{\partial\mu}{\partial\bar{C}}C'\bar{\dot{\gamma}} + \frac{\partial\mu}{\partial\bar{\gamma}}\gamma'\bar{\dot{\gamma}} + \dots\right)}^{\tau'}, \quad (2.6)$$

where, $\bar{\tau}$ and τ' are the time-averaged and the fluctuating part of the shear stress, respectively.

Performing Reynolds decomposition on the convective terms in the momentum equation results in the extra term $\rho u_i' u_j'$, where $\vec{u} = (u_1, u_2, u_3)$ is the velocity vector and $i, j = 1,2,3$. Lumping this expression with the fluctuating part of the shear stress yields,

$$\hat{\tau} = \tau - \rho u_i' u_j' = \bar{\tau} + (\tau' - \rho u_i' u_j'). \quad (2.7)$$

Factoring shear rate out of expression (2.7) yields,

$$\hat{\tau} = \left(\bar{\tau}/\dot{\gamma} + (\tau' - \rho u_i' u_j')/\dot{\gamma}\right)\dot{\gamma} = \overbrace{\left(\mu_l + \mu_t\right)}^{\tilde{\mu}}\dot{\gamma}, \quad (2.8)$$

where, $\tilde{\mu}$ is called the compounded apparent viscosity and is composed of a laminar apparent viscosity, $\mu_l = \bar{\tau}/\dot{\gamma}$, and a turbulent apparent viscosity, $\mu_t = (\tau' - \rho u_i' u_j')/\dot{\gamma}$.

The stress and the shear rate profiles described in sections 2.2.4 and 2.2.2 can be used to obtain average compounded apparent viscosities for the boundary layer, $\tilde{\mu}_{BL}$, and the free shear layer, $\tilde{\mu}_{FSL}$, similar to the laminar apparent viscosity data shown in Figure 2.3c.

The laminar apparent viscosity data obtained from the rheometer tests (section 2.2.3), corresponds to the viscosity of the mixtures within the laminar regime while the compounded apparent viscosity data computed from the stress and shear rate profiles of Figures 2.6 and 2.3b does not make such a restriction regarding the regime of the flow. Therefore, deviation of the former measured viscosity from the computed one is a measure of deviation of a flow from the laminar regime. In other words, this deviation can be seen as a measure of turbulence, albeit a qualitative one due to the approximations followed here. The ratios $\tilde{\mu}_{BL}/\mu_{BL}$ and $\tilde{\mu}_{FSL}/\mu_{FSL}$ will be used to evaluate the regimes of the flows within the boundary and free shear layers, respectively.

Due to the farther distance of the second UVP probe from the inlet compared to the first one, the flow at this location is assumed to be closer to steady equilibrium conditions. Therefore, it is suggested here that the data obtained from the second UVP probe satisfies the assumptions for calculating the compounded apparent viscosity profiles.

2.2.6. INNER VARIABLE AND EXISTENCE OF LOGARITHMIC REGION

Ludwig Prandtl and Theodore von Kármán deduced that a turbulent boundary layer must contain a logarithmic overlap layer (White, 1991). In order to evaluate the existence of a logarithmic overlap region and hence, the state of the flow within the boundary layer, the inner variable

$$z^+ = \frac{z u_* \rho}{\mu_{BL}}, \quad (2.9)$$

is calculated, where, ρ is the density of the mixture within the mixing tank and u_* is the friction velocity approximated by,

$$u_* = \sqrt{g\,\tilde{H}\,R\,\phi\,\sin(\theta)}. \tag{2.10}$$

In this expression, θ is the bed slope, $\tilde{H} = \frac{WH}{(2H+W)}$ is the hydraulic radius, with $W = 0.1\ m$ representing the width of the flume (Figure 2.1), $\phi = \frac{V_s}{V_s+V_w}$ is the sediment volume concentration, with V_s representing the sediment volume, and V_w the volume of water, $R = \frac{\rho_s-\rho_w}{\rho_f}$, with ρ_w representing the water density, ρ_s, the sediment density, and ρ_f the fluid density.

Within the boundary layer, the viscous sublayer and the buffer layer extend from approximately $0 \leq z^+ \leq 30$, and the logarithmic overlap region begins from approximately $30 < z^+$ (White, 1991). Therefore, a turbulent boundary layer containing a logarithmic overlap region is expected to have a maximum inner variable, $z^+_{\delta_{BL}}$, well above 30.

2.2.7. REYNOLDS NUMBERS, FROUDE NUMBER, AND DIMENSIONELESS YIELD STRESS PARAMETER DEFINITIONS

It was found that in order to differentiate various density flows, two Reynolds numbers for the boundary and free shear layers, a Froude number, and a dimensionless yield stress parameter are needed. The Reynolds numbers characterize the laminar or turbulent regime of a flow within the boundary and the free shear layers and are defined as,

$$Re_{\mu,FSL} = \frac{\rho_{FSL}U(2\delta_{FSL})}{\mu_{FSL}}, \tag{2.11a}$$

$$Re_{\mu,BL} = \frac{\rho_{BP}U\delta_{BL}}{\mu_{BL}}, \tag{2.11b}$$

for the free shear layer (subscript FSL) and the boundary layer (subscript BL), respectively. In these expressions, U is the average velocity defined as,

$$U = \frac{\int_0^H \bar{u}\,dz}{H}, \tag{2.12}$$

and for a specific run was obtained by integrating the interpolated velocity profile of the run (Figure 2.3a), ρ_{BP} is the density of the mixture within the boundary and plug layers and was assumed to be equal to the density of the mixture within the mixing tank, and ρ_{FSL} is the density of the mixture in the free shear layer.

Within the free shear layer and above the inflection point the density varies between that of the plug layer to that of water at the height $z = \delta_{BL} + \delta_{PL} + h$. Therefore, the density at the inflection point was approximated by,

$$\rho_{FSL} = \rho_w + \frac{\left(\rho_{BP} - \rho_w\right)(h - \delta_{FSL})}{h}. \tag{2.13}$$

The largest Kelvin-Helmholtz eddies which are created within the free shear layer and which contribute the most to the mixing in this region can be viewed to rotate about the inflection point, as this is the point of maximum vorticity (White, 1991). Therefore, these eddies have a radius that spans from the top of the plug to the inflection point. Their diameter is approximately $2\delta_{FSL}$.
Following the definitions in (2.11), the laminar to turbulent transition zone starts at an approximate Reynolds number of 500. This is equivalent to a Reynolds number of 2000 if the definition of the length scale in (2.11) is replaced by the hydraulic diameter (Wang & Plate, 1996).
Using the definitions of the average velocity, U, and the flow height, H, the Froude number is defined as,

$$Fr = \frac{U}{\sqrt{gH}}. \tag{2.14}$$

For low concentration density flows the effect of density fluctuations on the inertial term in the momentum equation can be ignored. This is known as the Boussinesq approximation. This approximation falls apart for high concentration density flows. Therefore, a reduced gravity term is not considered here in the definition of the Froude number (Nappo, 2002).
The existence of a plug layer is here characterized by the dimensionless yield stress parameter, $\frac{\tau_y}{\Delta\tau}$, where, τ_y and $\Delta\tau$ were defined in section 2.2.4.

2.3. RESULTS

2.3.1. FLOW TYPES

Based on the experimental results four different flow types were observed which are defined by different vertical stacking patterns of flow states. The data sets obtained for runs 18, 20, 22, and 25 exhibit distinct characteristics corresponding to these four different flow types and will be used as examples. In this section the velocity profile, the boundary layer structure, and the free shear layer structure of these four flow types are discussed in detail.

VELOCITY PROFILE

Figure 2.7 depicts the velocity profiles of runs 18, 20, 22, and 25. Normalized velocity fluctuations, $\frac{u-\bar{u}}{\bar{u}}$, where, u is the recorded velocity and $\bar{u}$ is the time-averaged velocity, are also depicted at 3.8 mm from the bed, at the point of minimum root mean square of velocity fluctuations (u'_{rms}), and at the inflection point in the mixing layer.
Following a length scale analysis, the Kolmogorov length scales, the velocity amplitude spectrum, and the energy spectrum were calculated. Based on this analysis, it was observed that the measurement resolutions were not adequate for performing turbulence intensity calculations. Therefore, the velocity fluctuation data could only provide a qualitative means for the estimation of the level of turbulence.
From Figure 2.7a it can be observed that for run 18, the magnitude of velocity fluctuations is relatively small within the free shear layer, a large plug layer is visible within

the velocity profile of this run, and the magnitude of velocity fluctuations is relatively small within the boundary layer. By contrast the data of run 20 (Figure 2.7b) shows large velocity fluctuations within the free shear layer. A small plug layer is visible within the velocity profile of this run, and within the boundary layer the magnitude of velocity fluctuations is relatively small. The data for run 22 (Figure 2.7c) resemble that of run 20, with the exception that no plug layer is visible within the velocity profile of this run. Finally, the data of run 25 (Figure 2.7d) show relatively large velocity fluctuations within the free shear layer, no plug layer, and relatively large velocity fluctuations within the boundary layer.

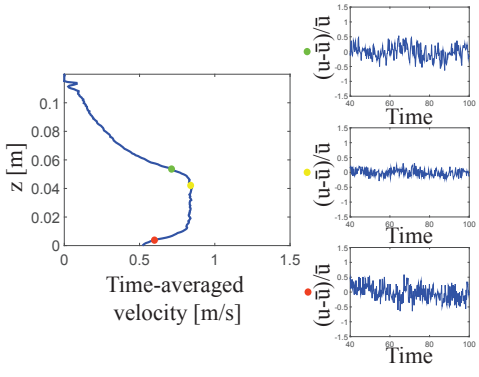

(a) Velocity profile (left) and velocity fluctuations (right) of run 18 at the location of UVP2 probe.

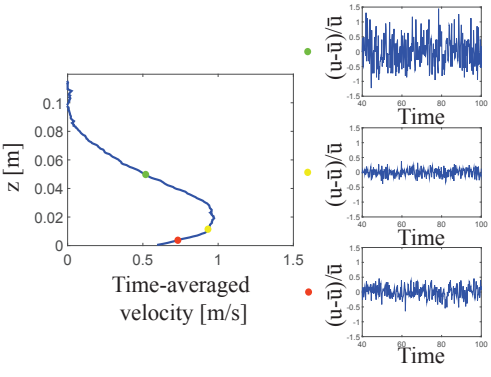

(b) Velocity profile (left) and velocity fluctuations (right) of run 20 at the location of UVP1 probe.

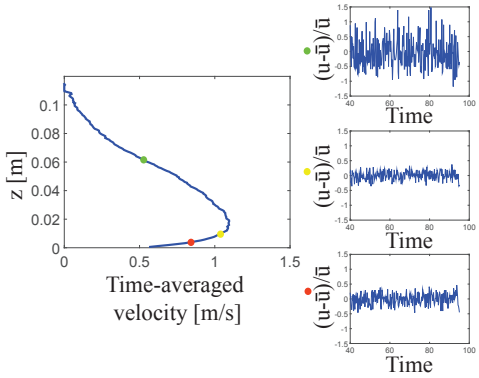

(c) Velocity profile (left) and velocity fluctuations (right) of run 22 at the location of UVP1 probe.

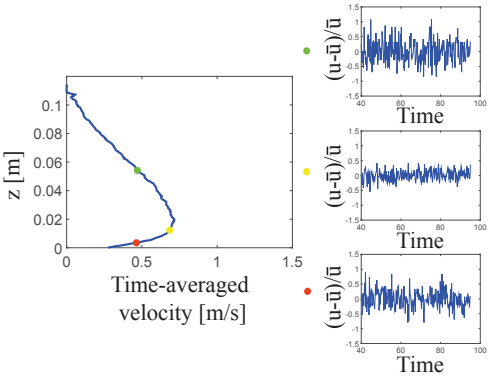

(d) Velocity profile (left) and velocity fluctuations (right) of run 25 at the location of UVP1 probe.

Figure 2.7: Velocity profiles and fluctuations of runs 18 (a), 20 (b), 22 (c), and 25(d). Normalized velocity fluctuations, $\frac{u-\bar{u}}{\bar{u}}$, are depicted at 3.8 mm from the bed (red), at the point of minimum u'_{rms} (yellow), and at the inflection point (green).

BOUNDARY LAYER STRUCTURE

Figure 2.8 shows the maximum inner variable versus the boundary layer Reynolds number for different runs. The vertical orange lines in these plots are located at $Re_{\mu,BL} = 500$, and separate the laminar and turbulent regimes. The horizontal orange lines are located at $z^+ = 30$, and indicate termination of the buffer layer and the beginning of the logarithmic overlap region. It can be observed that the boundary layers of the runs with 21% sediment concentration, shown in black, extend from the bed until the end of the buffer layer. The boundary layers of the runs with 15% sediment concentration, shown in red, extend from the bed into the logarithmic region and terminate within this region. The boundary layers of the runs with 9% sediment concentration, shown in green, extend the furthest into the log-law region and have Reynolds numbers higher than 500. Therefore, the data suggests that the boundary layers of these runs are turbulent.

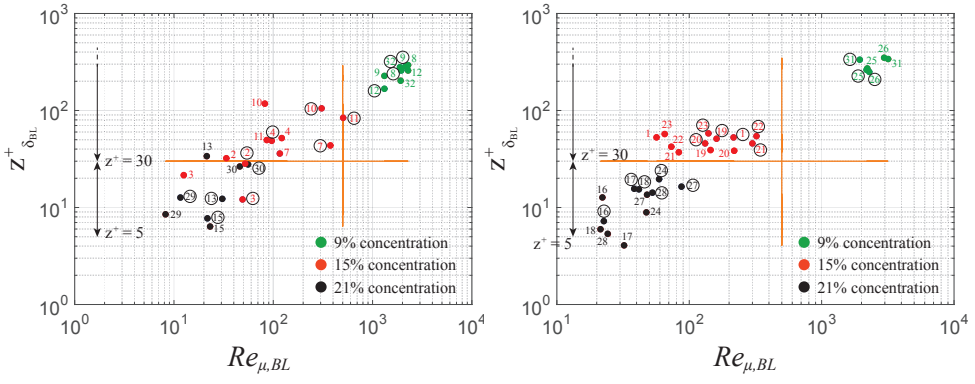

(a) Sand-clay-water runs.

(b) Sand-silt-clay-water runs.

Figure 2.8: Maximum inner variable, $z^+_{\delta_{BL}}$, versus $Re_{\mu,BL}$ for (a) sand-clay-water runs, and (b) sand-silt-clay-water runs. The vertical orange lines indicate $Re_{\mu,BL}$=500. The horizontal orange lines indicate z^+=30. Dots indicate where different runs are situated in this plot. Run numbers are placed next to their corresponding dots. Encircled run numbers indicate data obtained from the first UVP probe. Runs with 21% sediment concentration are shown in black, runs with 15% sediment concentration are shown in red, and runs with 9% sediment concentration are shown in green.

Figure 2.9 shows the ratio of compounded apparent viscosity, $\tilde{\mu}_{BL}$, obtained as in section 2.2.5, to the laminar apparent viscosity obtained from rheometer tests, μ_{BL}, versus the boundary layer Reynolds number, $Re_{\mu,BL}$. It can be observed that for higher concentration runs, shown in black and red, the ratio $\tilde{\mu}_{BL}/\mu_{BL}$, is low, indicating low levels of turbulence within the boundary layers of these runs. For the runs with 9% sediment concentration, shown in green, on the other hand, $10 < \tilde{\mu}_{BL}/\mu_{BL}$, indicating higher values of turbulent viscosity and turbulence levels within the boundary layers of these runs.

The velocity fluctuation data, the maximum inner variable plots, and the apparent viscosity results suggest laminar and close to laminar boundary layer conditions for runs 18, 20, and 22, and turbulent boundary layer conditions for run 25.

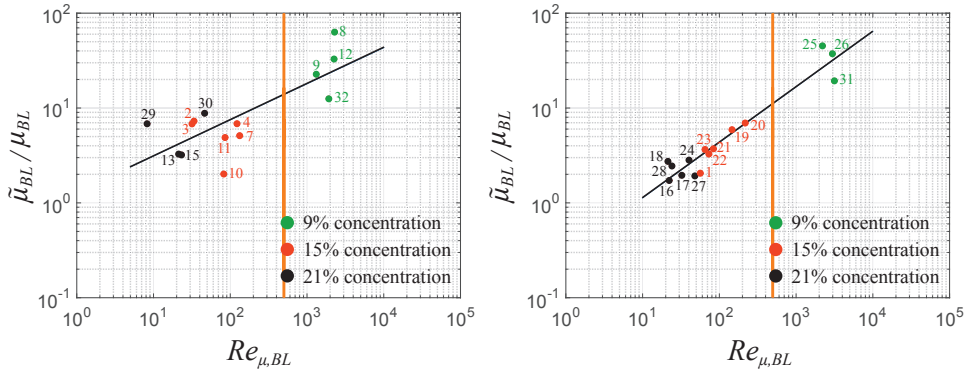

(a) Sand-clay-water runs.

(b) Sand-silt-clay-water runs.

Figure 2.9: $\tilde{\mu}_{BL}/\mu_{BL}$ versus $Re_{\mu,BL}$ for the data gathered from the second UVP probe for (a) sand-clay-water runs, and (b) sand-silt-clay-water runs. The vertical orange line indicates $Re_{\mu,BL}$=500. Dots indicate where different runs are situated in this plot. Run numbers are placed next to their corresponding dots. Runs with 21% sediment concentration are shown in black, runs with 15% sediment concentration are shown in red, and runs with 9% sediment concentration are shown in green. The black line is a least squares fit to the data.

FREE SHEAR LAYER STRUCTURE

A characteristic of fully developed turbulent flows is self-similarity (White, 1991). For fully developed turbulent free shear layers, self-similarity entails $\bar{u}_{inf}/\bar{u}_{max} \rightarrow 0.5$, where, $\bar{u}_{inf}$ is the time-averaged velocity at the inflection point and $\bar{u}_{max}$ is the maximum time-averaged velocity. Figure 2.10 shows the plots of $\bar{u}_{inf}/\bar{u}_{max}$ versus $Re_{\mu,FSL}$ for different runs.

It can be observed that the runs with 21% sediment concentration, shown in black, have relatively high values of $\bar{u}_{inf}/\bar{u}_{max}$ and fall within the laminar region. Various runs with 15% sediment concentration, shown in red, have high values of $\bar{u}_{inf}/\bar{u}_{max}$ and fall within the laminar region, while the others have low values of $\bar{u}_{inf}/\bar{u}_{max}$ and fall within the turbulent region. The runs with 9% sediment concentration, shown in green, have $\bar{u}_{inf}/\bar{u}_{max} \lesssim 0.67$ and fall within the turbulent region.

Self-similarity of fully turbulent free shear flows also entails the collapse of all properly scaled free shear layer velocity profiles onto each other. Figure 2.11a, depicts the scaled free shear layers of eleven runs at the location of the second UVP probe. These eleven runs were chosen out of the total number of runs for the sake of clarity in presentation. In this figure, 0.99 $\bar{u}_{max}$ is the time-averaged velocity above the plug layer (Figure 2.3(a)), $\bar{u}(H)$ is the time-averaged velocity at the height H, $\bar{u}$ is the time-averaged velocity with range [$\bar{u}(H)$,0.99 $\bar{u}_{max}$], and z is the distance above the bed and varies between $\delta_{BL}+\delta_{PL}$ and H. It can be seen that the free shear layers of the majority of the runs with 21% sediment concentration fall above those of runs with 15% and 9% sediment concentrations. Figure 2.11(b) shows the scaled free shear layers of run 18 at the location of the second UVP probe, and runs 20, 22, and 25 at the location of the first UVP probe. It can be seen that the free shear layer of run 18 is recognizable and falls above those of the other runs. This deviation from the self-similar and hence fully turbulent flow for run 18 is in agree-

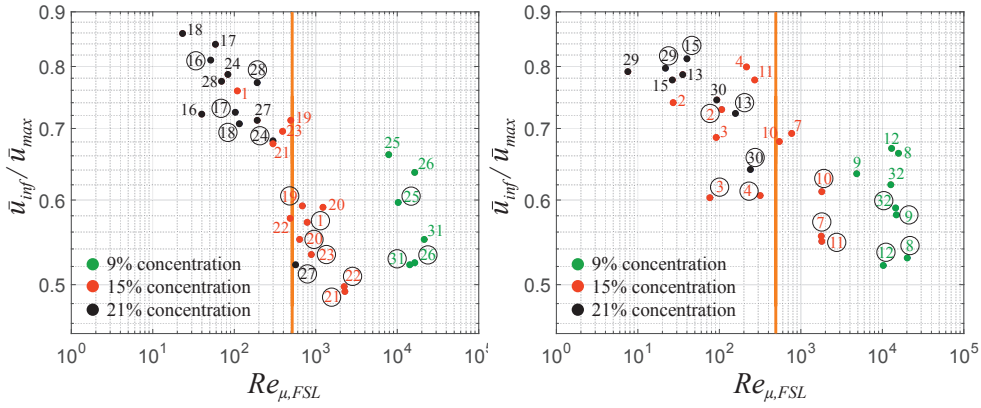

(a) Sand-clay-water runs.

(b) Sand-silt-clay-water runs.

Figure 2.10: Plots of $\bar{u}_{inf}/\bar{u}_{max}$ versus $Re_{\mu,FSL}$ for (a) sand-clay-water runs, and (b) sand-silt-clay-water runs. The vertical orange line indicates $Re_{\mu,FSL}$=500. Dots indicate where different runs are situated in this plot. Run numbers are placed next to their corresponding dots. Encircled run numbers indicate data obtained from the first UVP probe. Runs with 21% sediment concentration are shown in black, runs with 15% sediment concentration are shown in red, and runs with 9% sediment concentration are shown in green.

ment with the high values of $\bar{u}_{inf}/\bar{u}_{max}$ for this run, and the low velocity fluctuations observed within the free shear layer of this run (Figure 2.7).

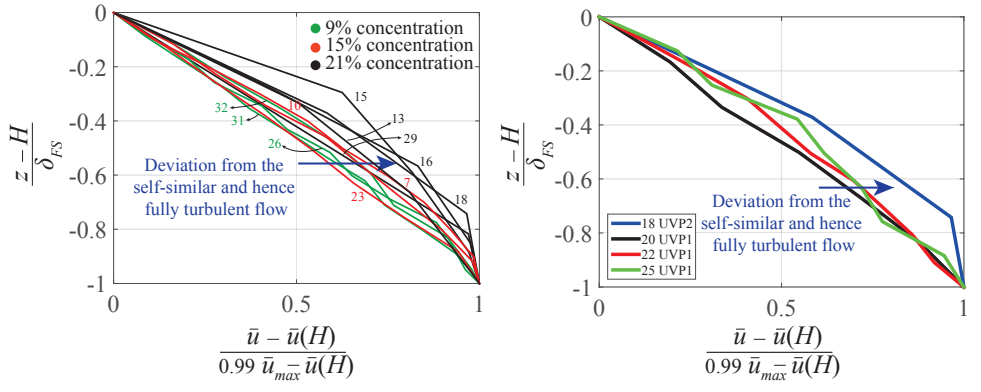

(a) Scaled free shear layers of 10 runs at the location of the second UVP probe.

(b) Scaled free shear layers of run 18, 20, 22, and 25.

Figure 2.11: Scaled free shear layers for (a) ten random runs, and for (b) the selected runs 18, 20, 22, and 25. In (a), runs with 21% sediment concentration are shown in black, runs with 15% sediment concentration are shown in red, and runs with 9% sediment concentration are shown in green.

Figure 2.12 shows the ratio of compounded apparent viscosity within the free shear layer, $\tilde{\mu}_{FSL}$, obtained as in section 2.2.4, and the laminar apparent viscosity, μ_{FSL}, obtained from rheometer tests, versus the free shear layer Reynolds number, $Re_{\mu,FSL}$.

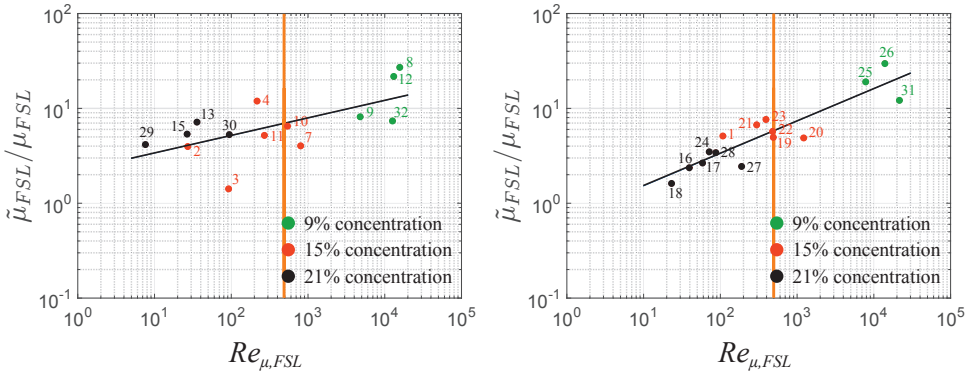

(a) Sand-clay-water runs.

(b) Sand-silt-clay-water runs.

Figure 2.12: $\tilde{\mu}_{FSL}/\mu_{FSL}$ versus $Re_{\mu,FSL}$ for the data gathered from the second UVP probe for (a) sand-clay-water runs, and (b) sand-silt-clay-water runs. The vertical orange line indicates $Re_{\mu,BL}$=500. Dots indicate where different runs are situated in this plot. Run numbers are placed next to their corresponding dots. Runs with 21% sediment concentration are shown in black, runs with 15% sediment concentration are shown in red, and runs with 9% sediment concentration are shown in green. The black line is a least squares fit to the data.

Similar to the boundary layer results, in Figure 2.12 it can be observed that for higher concentrations the ratio $\tilde{\mu}_{FSL}/\mu_{FSL}$, decreases towards one. Higher viscosity ratios are reached at higher Reynolds numbers, suggesting higher turbulence levels for more dilute flows within the free shear layer. The increase in viscosity ratio is less pronounced in Figure 2.12 compared to Figure 2.9.
Within the free shear layer, the velocity fluctuation data (Figure 2.7), the self-similarity results (Figures 2.10 and 2.11), and the viscosity calculations (Figure 2.12) suggest laminar conditions for run 18 and turbulent conditions for runs 20, 22, and 25.

2.3.2. SEDIMENT DEPOSITS

Figure 2.13 shows the deposits emplaced by the runs in Figure 2.7. The classification scheme of Talling et al. (2012) is used for each layer and the classification scheme of Sumner et al. (2009) is used for the complete deposits. The 21% sediment concentration flow of run 18, with a discharge rate of 10 m^3/h and on a bed slope of 6°, resulted in a very thin basal sand layer that was deposited by the body of the flow at the mid-section of the flume (Figure 2.1). Once the run was close to termination and the discharge rate waned, the tail of the flow resulted in en-masse deposition of a thick, uniform, mud-sand mixture throughout the flume, similar to the deposit Type IV of Sumner et al. (2009). A top thin clay drape was deposited from the suspension after the flow stopped. Similar to run 18, the 15% sediment concentration flow of run 20, with a discharge rate of 10 m^3/h and on a bed slope of 9.5°, resulted in a thin bottom sand layer that was deposited from the body of the flow at the mid-section of the flume. Once the run was close to termination and the discharge rate waned, the tail of the flow deposited a mud-sand layer throughout the flume. This layer was thinner compared to the mud-sand layer of run 18. A top thin clay drape was deposited from the suspension after the flow stopped. Similar to run 18,

the deposit from this run resembles the deposit Type IV of Sumner et al. (2009). Moving to a higher discharge rate of 15 m^3/h and a lower bed slope of 8°, the 15% sediment concentration flow of run 22 resulted in deposition of a bottom sand layer at the mid-section of the flume and at the location of the second UVP probe. This sand layer was emplaced by the body of the flow. Once the run was close to termination and the discharge rate waned, the tail of the flow deposited a mud-sand layer throughout the flume. A top thin clay drape was deposited from the suspension after the flow stopped. The deposits from this run at the mid-section of the flume and at the location of the second UVP probe resemble the deposit type III of Sumner et al. (2009). The 9% sediment concentration flow of run 25, with a discharge rate of 10 m^3/h and a bed slope of 6°, resulted in deposition of a bottom sand layer throughout the flume. This sand layer was emplace by the body of the flow. Once the run was close to termination and the discharge rate waned, the tail of the flow deposited a mud-sand layer at the location of the first UVP probe, a planar sand and sand-silt lamination at the mid-section of the flume, and a sand layer at the location of the second UVP probe. A top thin clay drape was deposited from the suspension after the flow stopped. The deposit from this run at the mid-section of the flume resembles the deposit type I of Sumner et al. (2009). At the location of the second UVP probe, this flow emplaced a deposit similar to the deposit Type II of Sumner et al. (2009).
It can be observed that in moving from run 18 to runs 20 and 22, the mud-sand layer becomes thinner and the basal clean sand layer forms an increasing proportion of the deposit. All in all, in moving from the top towards the bottom in Figure 2.13, it can be seen that more sand is deposited by the low concentration flows that experienced higher velocity fluctuations within the boundary layer. Furthermore, while the velocity profiles of runs 20 and 22 show different flow structures (Figure 2.7), their deposits do not differ much.

2.4. DISCUSSION OF FLOW TYPES AND THE RESULTING DEPOSITS

Subaqueous density flows can be classified based on the existence of turbulence within the free shear and/or boundary layer and presence of a plug layer. A dense and cohesive flow whose primary sediment support mechanism is not turbulence and which is laminar within the boundary and free shear layers and contains a plug layer is referred to as a plug flow (PF) (Figure 2.14a). The inflection point is relatively close to the plug for such a flow (Figure 2.14a). During the experiments such a flow type resulted in either no deposition or deposition of a thin basal clean sand layer as in the case of run 18 in Figure 2.13. The thin basal clean sand layer is attributed to the large amount of shearing within the boundary layer, which breaks up the gel structure created by the clay particles and dramatically decreases the yield stress and viscosity of the suspension (Ovarlez et al., 2012). Since the turbulence levels are low within the boundary layer of PFs (i.e., low sand grain support by turbulence), this further facilitates the movement of sand particles through the boundary layer and allows them to settle, resulting in the deposition of a basal clean sand layer during the run. Once the discharge rate waned, within the tail region of the flow the yield stress of the fluid overcame the force of gravity and the flow froze, resulting in en masse deposition of a thick, uniform, mud-sand mixture. A top clay drape was deposited from the suspension after the flow stopped.

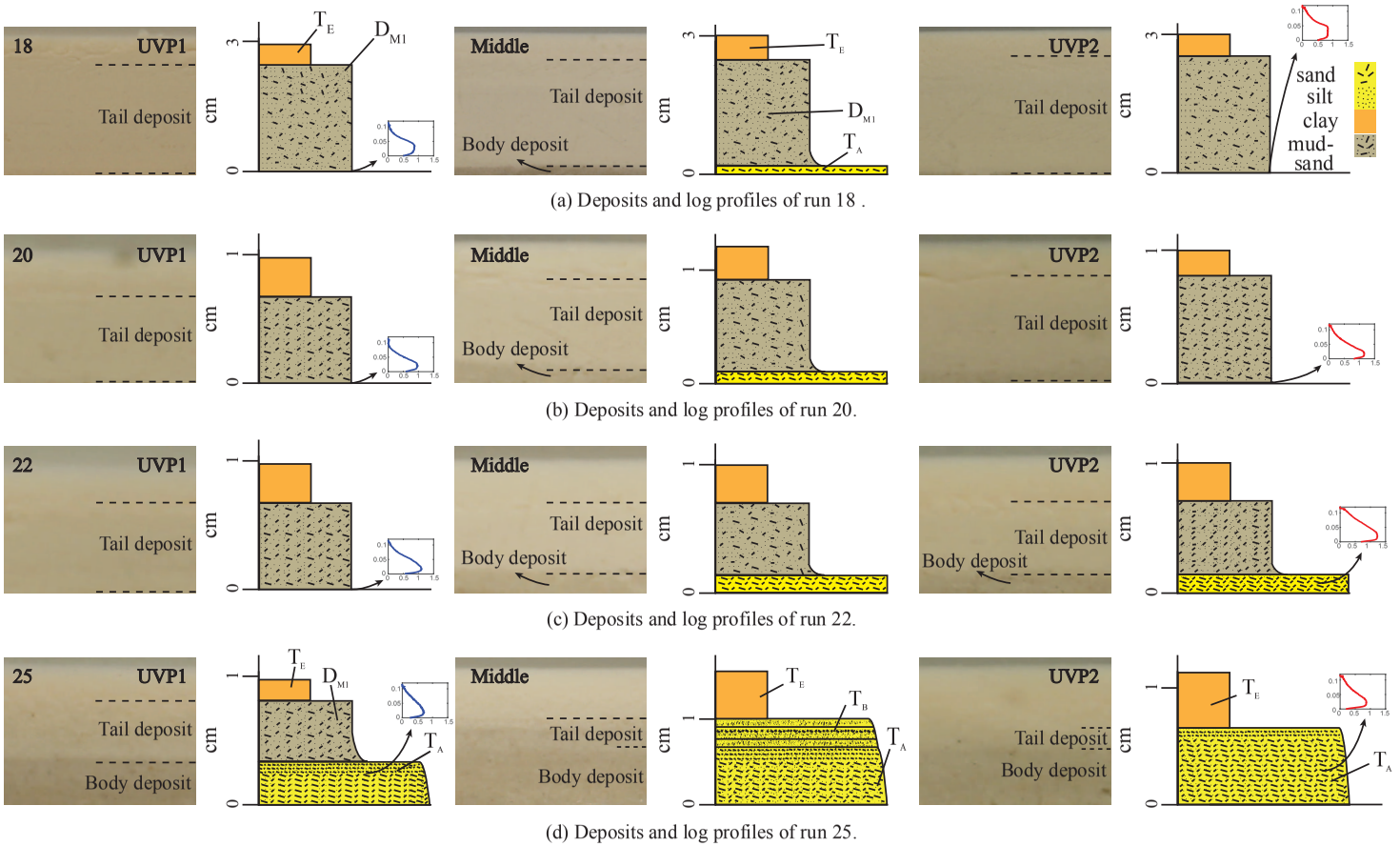

(a) Deposits and log profiles of run 18 .

(b) Deposits and log profiles of run 20.

(c) Deposits and log profiles of run 22.

(d) Deposits and log profiles of run 25.

Figure 2.13: Deposits and log profiles of (a) run 18, (b) run 20, (c) run 22, and (d) run 25, at the location of the first UVP probe (left), at the mid-section of the flume (middle), and at the location of the second UVP probe (right). Inset plots depict velocity profiles at the location of the first UVP probe (blue), and the right UVP probe (red). Classification of Talling et al. (2012) is used for the deposit types. T_E: Fine mud, D_{M1}: Muddy sand, T_B: Planar laminae and massive sand, T_A: Massive sand.

Higher slopes, lower sediment concentrations, or higher discharge rates, all amplify Kelvin-Helmholtz instabilities within the free shear layer. As these instabilities become more severe, the top free shear layer becomes turbulent, yet a plug may continue to exist and the boundary layer may remain laminar. This flow is referred to as top transitional plug flow (TTPF) (Figure 2.14b). If heavier grains are not supported within the turbulent free shear layer, they settle onto the plug layer and mix into the mud-sand mixture. Experiments showed that a TTPF can result in the deposition of a basal clean sand layer during the flow. This layer was covered by a mud-sand deposit from the tail and a mud drape which settled from suspension once the run was terminated.

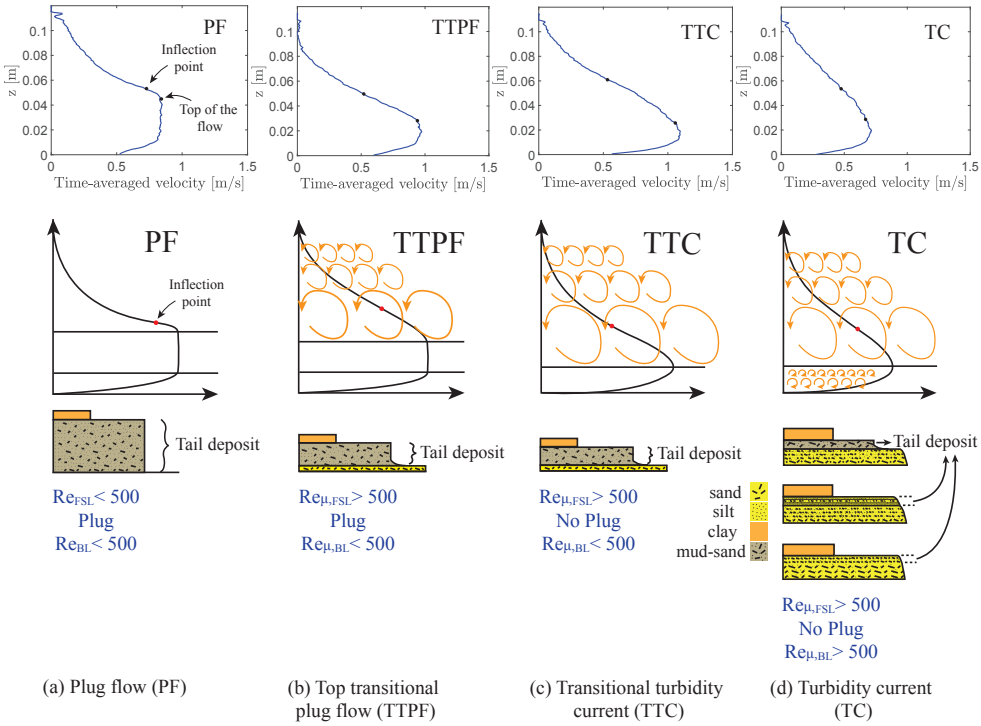

(a) Plug flow (PF) (b) Top transitional plug flow (TTPF) (c) Transitional turbidity current (TTC) (d) Turbidity current (TC)

Figure 2.14: Velocity profiles (top), schematics of the flow structures (middle), and log profiles of the deposits (bottom) of, (a) a plug flow (PF), (b) a top transitional plug flow (TTPF), (c) a transitional turbidity current (TTC), and, (d) a turbidity current (TC). The orange arrows indicate turbulent regions with Reynolds numbers higher than 500. Three deposit types were observed for TCs, as was explained in Figure 2.13 for run 25.

As the plug erodes away, due to the top and the bottom stresses, within a TTPF, the boundary layer may still remain within the laminar regime because of higher concentrations close to the substrate where it is sheltered from outside fluctuations. When the plug disappears, the velocity profile begins to resemble that of a turbidity current, yet the boundary layer remains laminar. Such a flow is here referred to as a transitional turbidity current (TTC) (Figure 2.14c). Experiments showed that a TTC can result in the deposition of a basal clean sand layer during the flow. This layer was overlain by a uniform

mud-sand mixture that was emplaced once the yield stress exceeded the gravitational forces within the tail region of the flow. A mud drape was emplaced on top of the deposits after the runs were terminated.

Finally, more dilution of the flow reduces the ability of the laminar boundary layer to withstand the outside disturbances and transition of the boundary layer is initiated by velocity perturbations induced by fluctuations within the external turbulent free shear layer (Thole & Bogard, 1996). Once the boundary layer transitions from laminar to turbulent, the turbulent free shear layer and boundary layer begin to interact. This interaction is dictated by the size and strength of the eddies within these layers (Hunt & Durbin, 1998; Thole & Bogard, 1996). In this regime the sediment is mainly supported by turbulence and such a flow is referred to as a turbidity current (TC) (Figure 2.14d). Experiments showed that this flow type resulted in deposition of a massive bottom sand layer such as in the deposit of run 25 in Figure 2.13. This layer was overlain by either a mud-sand mixture or a sand and sand-silt interlamination. In all cases a mud drape was deposited on top of the deposit after the run was terminated.

For turbulent flows in which turbulence levels are high enough to break the gel structure of the clay, the conditions are favorable for the deposition of sand and silt. If turbulence levels are just high enough to support the silt grains, only sand particles will be deposited. On the other hand if the turbulence levels are not high enough to support the silt grains, sand and silt are deposited together. If the flow is on the edge between these two regimes, it may move back and forth between them, i.e., moving back and forth between depositing only sand and depositing sand together with silt. Such a flow results in the deposition of sand and sand-silt interlamination as in the deposit of run 25 at the mid-section of the flume in Figure 2.13(d). Higher turbulence levels that can support silt grains result in the deposition of clean bottom sand layer as in the deposit of run 25 at the location of the second UVP probe in Figure 2.13(d). On the other hand, lower turbulence levels cannot efficiently separate the sand and silt from the clay and result in the deposition of a mud-sand mixture as in the deposit of run 25 at the location of the first UVP probe in Figure 2.13(d).

The deposits investigated in this study show that both the effect of the flow type and rheology as well as the time evolution of the passage of flow are important in the formation of the structures within a deposit. The deposit emplaced by a flow in steady state at a certain location is solely dependent on the structure of the flow at that location. For clay-rich flows however, the deposits are mainly the result of a time-dependent decrease in the flow height and dominance of the yield strength of the fluid over the force of gravity. For dilute clay-laden flows, time dependence may be in the form of fluctuations in the turbulence levels which manifests itself in the form of laminations within the deposit. All in all, the structure of the deposit at a location is a result of the flow structures at that location as well as the time dependent variations in the flow height and turbulence levels.

Table 2.2 presents different flow types resulting from permutation of flow states within the boundary and free shear layers and the presence or absence of a plug layer. From the table it becomes apparent that the flows observed in this study correspond to a subset of a wider range of possible flow structures. However, the cases $X1$ to $X3$ can be argued to have low probabilities of occurrence, as will be explained in the following para-

Table 2.2: Flow types resulting from permutation of flow states within the boundary and free shear layers and the presence or absence of a plug layer. The abbreviations stand for free shear layer (FSL) and boundary layer (BL). Flow types denoted by X1, X2, and X3 have arguably low probabilities of occurrence.

Flow type	FSL	BL	Plug
Plug flow	Laminar	Laminar	Yes
Top transitional plug flow	Turbulent	Laminar	Yes
X1	Laminar	Turbulent	Yes
Top and base transitional plug flow	Turbulent	Turbulent	Yes
X2	Laminar	Laminar	No
Transitional turbidity current	Turbulent	Laminar	No
X3	Laminar	Turbulent	No
Turbidity current	Turbulent	Turbulent	No

graphs. The table also hypothesizes the existence of a top and base transitional plug flow (TBTPF) with a turbulent free shear layer, a plug layer, and a turbulent boundary layer. Although such a flow was not observed in this study, its existence is hypothesized here. The flow types in the classification of Baas et al. (2009) for subaerial flows extensively classify the evolutionary stages of a turbulent boundary layer in the vicinity of a plug layer and therefore cover the plug and boundary layer regions of a TBTPF. However, more work is needed to demonstrate the occurrence and characteristics of TBTPFs.

The cases $X1$ and $X3$ in Table 2.2 are predicted to have a laminar free shear layer and a turbulent boundary layer. The existence of an inflection point within the velocity profile of the free shear layer results in the existence of inviscid instability and possibly a lower critical Reynolds number (White, 1991). Although, this effect may to some extent be counteracted by the stratification and influence of the buoyant force on suppressing the growth of disturbances (Nappo, 2002), the inviscid instability theory suggests possibly earlier transition of the free shear layer to turbulence than the boundary layer. Therefore, a flow with a laminar free shear layer and a turbulent boundary layer, cases $X1$ and $X3$ in Table 2.2, seems to have a low probability occurring.

The case $X2$ in Table 2.2 is predicted to have a laminar free shear layer, no plug layer, and a laminar boundary layer. From equation (2.3), for a subaerial clay laden flow in equilibrium conditions with only gravitational and shear stress forces one has,

$$\left(\rho - \rho_w\right) g \sin\theta \left(H - \delta_{BL}\right) = \tau_y, \tag{2.15}$$

where, H is the flow height. From equation (2.15), it can be deduced that for a yield stress fluid, i.e., $\tau_y \neq 0$, with no shearing at the top, the plug layer cannot disappear, i.e., $(H - \delta_{BL}) \neq 0$. For a subaqueous clay laden flow the plug may be sheared away by the stresses at the top. However, then the density must be high enough for the gravitational force of the sheared laminar top layer to overcome the fluid yield stress, and hence induce a flow, and low enough to avoid a plug layer to be created. Such a flow, case $X2$ in Table 2.2, seems to have a low probability of occurrence.

2.5. FLOW REGIME

In order to connect the regimes of each flow type introduced here with those of analogue large-scale flows in nature, appropriate scaling parameters are necessary. Scaling of the boundary and free shear layers can be achieved using the usual Reynolds and Froude numbers. Furthermore, the evaluation of the existence of a plug region is accomplished here with the dimensionless parameter $\tau_y/\Delta\tau$ (Figure 2.6). In this way, a flow type can be associated with a natural large-scale density flow, or vice versa, using a Froude number, two Reynolds numbers, and a non-dimensional yield stress parameter, $\tau_y/\Delta\tau$.

2.5.1. BOUNDARY LAYER SCALING

Figure 2.15 depicts the boundary layer Reynolds number vs. the Froude number for all the runs. The orange line corresponds to the beginning of the turbulent region with a Reynolds number of 500.

The four observed flow types, PF, TTPF, TTC, and TC, are marked by yellow, orange, brown, and green, respectively. Moving from the left to the right in Figure 2.15, it can be seen that PFs dominate the regions with low boundary layer Reynolds and Froude number. On average, TTPFs and TTCs have higher boundary layer Reynolds and Froude numbers compared to PFs. The separation of TTPFs from TTCs is not very clear. TCs dominate the high boundary layer Reynolds number regions of the figure and on average seem to have lower Froude numbers compared to TTPFs and TTCs.

The inset plots in Figure 2.15 are the velocity profiles of selected runs. It can be seen that by moving from PFs towards TTPFs, the plug layer diminishes in size and finally disappears for TTCs and TCs.

2.5.2. FREE SHEAR LAYER SCALING

Figure 2.16 depicts the free shear layer Reynolds number vs. the Froude number for all the runs.

The flow types in this figure follow a trend similar to that of Figure 2.15. PFs dominate the regions with low free shear layer Reynolds and Froude number. On average, TTPFs and TTCs have higher free shear layer Reynolds and Froude numbers compared to PFs. The separation of TTPFs from TTCs seems to be better than in Figure 2.15. TCs dominate the high free shear layer Reynolds number regions of the figure.

The inset plots in Figure 2.16 are the velocity profiles of selected runs and represent each flow type. The log profiles of the deposits that were emplaced by the majority of the runs, containing the different flow types, are also depicted. Moving from low to high Reynolds numbers, it can be seen that the thick mud-sand deposit that is present for clay-rich flows diminishes in thickness and more sand is deposited from the body of the flow. TCs result in the deposition of most sand. However, at high Reynolds numbers very little deposit is emplaced by the TCs and most of the sediment is bypassed into the basin.

2.5.3. PLUG LAYER SCALING

In order to classify a flow as a TTC or as a TTPF, it is necessary to relate the existence of a plug layer to the physical properties of a density flow. Figure 2.17 depicts the non-dimensional yield stress parameter, $\frac{\tau_y}{\Delta\tau}$, as a function of the boundary layer Reynolds

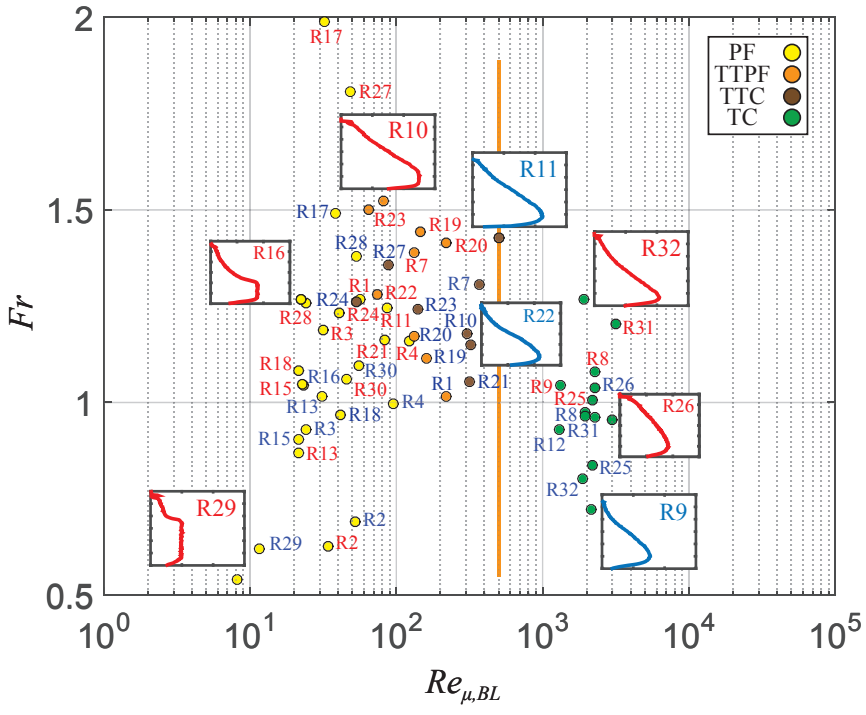

Figure 2.15: Froude number vs. boundary layer Reynolds number for all the runs. Inset plots are the velocity profiles of the runs obtained from the first (blue) and the second (red) UVP probes. Circles represent where each run is situated within the plot. The run numbers are shown next to each circle and represent the data from the first (blue) or the second (red) UVP probes. The yellow, orange, brown, and green colors represent the flow type corresponding to each run. The orange line separates the laminar from the turbulent flow regime.

number for all the runs. The data in this figure suggests that below the approximate value of $\frac{\tau_y}{\Delta\tau} = 0.25$ the plug layer disappears. This threshold is depicted with a dashed horizontal line to convey that this boundary may not be a horizontal or a linear boundary.

2.5.4. DISCUSSION OF SCALING PARAMETERS

In this study density flows are treated as flows of non-Newtonian fluids. Writing the Navier-Stokes equations for such flows and scaling the equations results in Reynolds and Froude numbers as scaling parameters. The complexities which arise due to various stresses that accompany momentum transport within the mixture (Iverson, 1997) are buried in the apparent viscosity term here obtained from rheometry experiments. The complication which arises here is the problem of connecting the scaling parameters that characterize very low concentration turbulent flows to the scaling parameters that characterize clay-rich laminar flows. An attempt to overcome this complication, which has been followed here, is to separate the flows into regions with different flow regimes, i.e., a free shear layer, a plug layer, and a boundary layer. The free shear and boundary layers in general have different Reynolds numbers and consequently one may be lami-

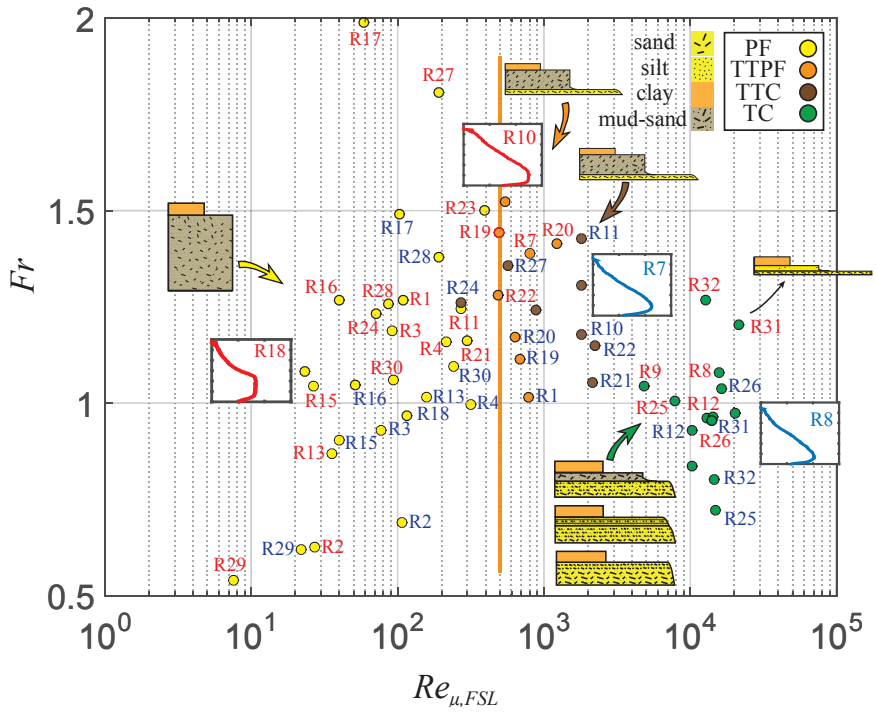

Figure 2.16: Froude number vs. free shear layer Reynolds number for all the runs. Inset plots are the velocity profiles of the runs obtained from the first (blue) and the second (red) UVP probes. Circles represent where each run is situated within the plot. The run numbers are shown next to each circle and represent the data from the first (blue) or the second (red) UVP probes. The yellow, orange, brown, and green colors represent the flow type corresponding to each run. The orange line separates the laminar from the turbulent flow regime. The log profiles of the deposits that were emplaced by the majority of the runs, corresponding to the different flow types, are also depicted. Three deposit types were observed for TCs, as was explained in Figure 2.13 for run 25.

nar while the other is turbulent.

Figures 2.15 and 2.16 show that PFs dominate the low Reynolds and Froude number regions. On average, TTPFs and TTCs have higher Reynolds and Froude numbers compared to PFs. TCs dominate the high Reynolds number regions of the figures and on average seem to have lower Froude numbers compared to TTPFs and TTCs.

For TCs, the Reynolds Number crucially controls the deposits. Flows with higher Reynolds numbers support more sand, while flows with lower Reynolds numbers do not efficiently separate the sand from the clay, and hence, result in the deposition of mud-sand mixtures. Figure 2.16 suggests that there exists a TC with certain Reynolds and Froude numbers which can result in the maximum clean sand deposition.

The fact that at approximately $\frac{\tau_y}{\Delta\tau} < 0.25$ the plug layer disappears is reminiscent of the Richardson number criterion of stability which states that dynamic instability occurs for $0 \leq Ri \leq 1/4$, while for $1/4 < Ri$ the flow is stable (Nappo, 2002). This point however, requires further investigation.

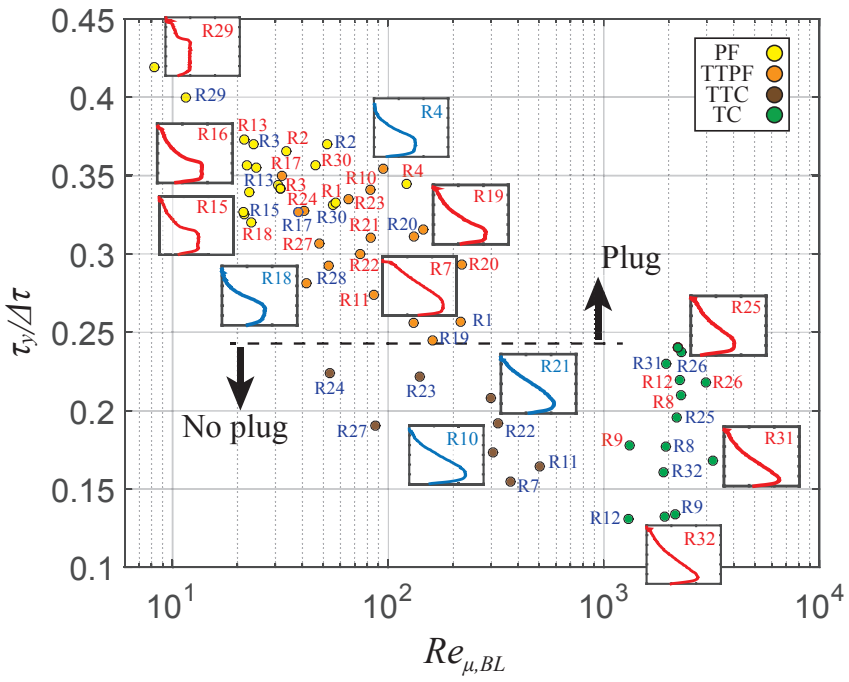

Figure 2.17: Non-dimensional yield stress parameter as a function of boundary layer Reynolds number for all the runs. Inset plots are velocity profiles of the runs obtained from the first (blue) and the second (red) UVP probes. Circles represent where each run is situated within the plot. The run numbers are shown next to each circle and represent the data from the first (blue) or the second (red) UVP probes. The yellow, orange, brown, and green colors represent the flow type corresponding to each run. The horizontal line separates the regions where a plug exists from where it does not. The line is dashed to convey that this boundary may be a sloping or a curved line.

2.6. CONCLUSIONS

Based on the state of the free shear and boundary layers and existence of a plug, a clay-rich density flow may fall within one of four distinct flow types: 1) a clay-rich plug flow (PF), 2) a top transitional plug flow (TTPF), 3) a transitional turbidity current (TTC) and, 4) a turbulent turbidity current (TC). These flow types were observed in this study and we have demonstrated that they can be distinguished in measurements performed on experimental density flows.

It was observed that clay-rich PFs resulted in either no deposition or deposition of a thin bottom sand layer. TTPFs and TTCs were mostly characterized by a thin bottom sand layer. The bottom sand layers in PFs, TTPFs, and TTCs were overlain by a mud-sand mixture that was emplaced by the tail of the flow. TCs resulted in the deposition of a thick massive bottom sand layer which was overlain by either a mud-sand mixture or a sand and silt planar lamination from the tail of the flow. In all cases a mud drape was deposited on top of the deposits after the runs were terminated.

The free shear and boundary layers in general have different Reynolds numbers and consequently, one may be laminar while the other is turbulent. PFs on average have lower Reynolds and Froude numbers compared to TTPFs and TTCs. TCs have the highest Reynolds numbers. However, on average they seem to have lower Froude numbers compared to TTPFs and TTCs.

It was observed that in moving from low to high Reynolds numbers, the thick mud-sand deposit that is emplaced by the tail of the flow diminishes in thickness and more sand is deposited from the body. At high Reynolds numbers turbulent energy can be high enough to support the heavier grains. As a result, very little deposit may be emplaced by the flow. Flows with low Reynolds numbers on the other hand, do not have enough turbulent energy to efficiently separate the sand from the clay, and hence, result in very little sand deposition. Therefore, the Reynolds versus Froude number plots suggest the existence of a flow within the turbulent regime that may produce clean sand deposits.

The Fr, Re_{BL}, Re_{FSL}, and $\tau_y/\Delta\tau$ parameter space presented here can be used to separate flow types and to connect the small-scale flume experiments to large-scale natural flows. The establishment of regime maps of our classification will allow numerical modelers to determine whether their flows are in a conventional TC regime, or whether they need to account for any of the more complex structures arising from the clay in the flows. The linkage between flow structures and depositional characteristics will enable better flow process interpretations from hybrid bed sequences studied by outcrop sedimentologists. Application of the results of this study to large-scale natural flows and their deposits is the scope of future research.

REFERENCES

Altinakar, M., Graf, W., & Hopfinger, E. (1996). Flow structure in turbidity currents. *Journal of Hydraulic Research*, *34*(5), 713–718. doi: 10.1080/00221689609498467

Baas, J. H., Best, J. L., & Peakall, J. (2011). Depositional processes, bedform development and hybrid bed formation in rapidly decelerated cohesive (mud-sand) sediment flows. *Sedimentology*, *58*, 1953–1987. doi: 10.1111/j.1365-3091.2011.01247.x

Baas, J. H., Best, J. L., Peakall, J., & Wang, M. (2009). A phase diagram for turbulent, transitional and laminar clay suspension flows. *Journal of Sedimentary Research*, *79*, 162–183. doi: 10.2110/jsr.2009.025

Coussot, P. (1997). *Mudflow Rheology and Dynamics*. Taylor & Francis.

Felix, M., Leszczyński, S., Ślaczka, A., Uchman, A., Amy, L., & Peakall, J. (2009). Field expressions of the transformation of debris flows into turbidity currents, with examples from the Polish Carpathians and the French Maritime Alps. *Marine and Petroleum Geology*, *26*, 2011–2020. doi: 10.1016/j.marpetgeo.2009.02.014

Haughton, P., Davis, C., McCaffrey, W., & Barker, S. (2009). Hybrid sediment gravity flow deposits - Classification, origin and significance. *Marine and Petroleum Geology*, *26*, 1900–1918. doi: 10.1016/j.marpetgeo.2009.02.012

Hermidas, N., Eggenhuisen, J. T., Silva Jacinto, R., Luthi, S. M., Toth, F., & Pohl, F. (2018). A Classification of Clay-Rich Subaqueous Density Flow Structures. *Journal of Geophysical Research*, *123*(5), 945–966. doi: 10.1002/2017JF004386

Hunt, B. J. C. R., & Durbin, P. A. (1998). Interactions between freestream turbulence and boundary layers. *CTR Annual Research Briefs*.

Islam, M. A., & Imran, J. (2010). Vertical structure of continuous release saline and turbidity currents. *Journal of Geophysical Research*, *115*, 1–14. doi: 10.1029/2009JC005365

Iverson, R. M. (1997). The physics of debris flows. *Reviews of Geophysics*, *35*, 245–296. doi: 10.1029/97RG00426

Kane, I. A., & Pontén, A. S. M. (2012). Submarine transitional flow deposits in the Paleogene Gulf of Mexico. *Geology*, *40*(12), 1119–1122. doi: 10.1130/G33410.1

Kneller, B. C., Bennett, S. J., & Mccaffrey, W. D. (1999). Velocity structure, turbulence and fluid stresses in experimental gravity currents. *Journal of Geophysical Research*, *104*(C3), 5381–5391. doi: 10.1029/1998JC900077

Manica, R. (2012). *Sediment Gravity Flows : Study Based on Experimental Simulations*. InTech. doi: 10.5772/28794

Meiburg, E., & Kneller, B. (2010). Turbidity Currents and Their Deposits. *Annual Review of Fluid Mechanics*, *42*, 135–156. doi: 10.1146/annurev-fluid-121108-145618

Mohrig, D., Whipple, K. X., Hondzo, M., Ellis, C., & Parker, G. (1998). Hydroplaning of subaqueous debris flows. *GSA Bulletin*, *110*(3), 387–394. doi: 10.1130/0016-7606(1998)110<0387:HOSDF>2.3.CO;2

Nappo, C. J. (2002). *An Introduction to Atmospheric Gravity Waves*. Elsevier Science.

Ovarlez, G., Bertrand, F., Coussot, P., & Chateau, X. (2012). Shear-induced sedimentation in yield stress fluids. *Journal of Non-Newtonian Fluid Mechanics*, *177-178*, 19–28. doi: 10.1016/j.jnnfm.2012.03.013

Pratson, L. F., Imran, J., Parker, G., Syvitski, J. P. M., & Hutton, E. (2000, jan). *Debris Flows vs. Turbidity Currents: A Modeling Comparison of Their Dynamics and Deposits* (Vol. 72). American Association of Petroleum Geologists. doi: 10.1306/M72703C6

Schwarz, H. U. (1982). *Subaqueous slope failures: experiments and modern occurences*. Schweizerbart'sche Verlagsbuchhandlung.

Sumner, E. J., Talling, P. J., & Amy, L. A. (2009, oct). Deposits of flows transitional between turbidity current and debris flow. *Geology*, *37*(11), 991–994. doi: 10.1130/G30059A.1

Talling, P. J., Masson, D. G., Sumner, E. J., & Malgesini, G. (2012). Subaqueous sediment density flows: Depositional processes and deposit types. *Sedimentology*, *59*, 1937–2003. doi: 10.1111/j.1365-3091.2012.01353.x

Talling, P. J., Wynn, R. B., Masson, D. G., Frenz, M., Cronin, B. T., Schiebel, R., … Amy, L. A. (2007, nov). Onset of submarine debris flow deposition far from original giant landslide. *Nature*, *450*, 541–544. doi: 10.1038/nature06313

Tanner, R. I. (2000). *Engineering Rheology*. OUP Oxford.

Thole, K. A., & Bogard, D. G. (1996). High Freestream Turbulence Effects on Turbulent Boundary Layers. *Journal of Fluids Engineering*, *118*(2), 276–284. doi: 10.1115/1.2817374

Wang, P. Z., & Plate, P. D. E. C. H. J. (1996). A preliminary study on the turbulence structure of flows of non-Newtonian fluid. *Journal of Hydraulic Research*, *34*(3), 345–361. doi: 10.1080/00221689609498484

White, F. M. (1991). *Viscous Fluid Flow*. McGraw-Hill.

3

THE RUN-OUT DISTANCE OF CLAY-LADEN SUBAQUEOUS GRAVITY FLOWS

Charm'd magic casements, opening on the foam
Of perilous seas, in faery lands forlorn.

John Keats

Studies have now covered numerous accounts of giant clay-laden subaqueous gravity flows that traveled extraordinarily long distances on slopes that decrease to virtually zero. Here, for the first time, it is suggested that the run-out distance of these cohesive flows is directly related to the static and the dynamic yield stresses of their constitutive sediment-water mixtures and their ability to stay close to the equilibrium conditions.

3.1. INTRODUCTION

CLAY-LADEN subaqueous gravity flows - also referred to as debris flows - consist of variable mixtures of water, clay, silt, sand, gravel, and boulders. Due to their cohesive strength, they usually occur on steep terrains as a consequence of slope failure. The deposits of these flows, called debrites, form by *en masse* settling and are predominantly composed of ungraded chaotic clay-rich mixtures that frequently contain clasts that are supported by the cohesive strength of the matrix (Talling et al., 2012).
A phenomenon that has been puzzling researchers for decades has to do with the long distances that these flows seem to be able to travel on very small slopes (Embley, 1976; Jacobi, 1976; Masson, 1996). Offshore Agadir (Morocco), individual flow deposits have been mapped that extend for ~ 1500 km from their source area (Talling et al., 2007). The

bathymetry of the region suggests that the gravity flow traveled on gradients as low as 0.01°. Another study from the western Canary Islands describes deposits of a two phase debris flow, consisting of a basal volcaniclastic debris flow phase overlain by a pelagic debris flow phase, called the Saharan debris flow, that traveled over 400 km on slopes that decrease to as low as 0.05° (Gee et al., 1999).

Firstly, we define the run-out distance of a subaqueous clay-laden flow as the distance that its center of mass travels until it comes to a standstill (Legros, 2002). Secondly, in order to achieve long run-out distances, we recognize that a such flow should ideally 1) Have a large sediment volume (Legros, 2002), 2) Experience very low drag and consequently, achieve high velocities, and 3) Stay close to the equilibrium conditions for a longer period of time.

Legros (2002) provided an in-depth study of the effect of flow volume on the run-out distance of gravity flows. Therefore, this point will not be addressed here. Instead the focus will be on explaining how subaqueous clay-laden flows can achieve high velocities and stay close to the equilibrium conditions.

3.2. DRAG REDUCTION

In order to achieve higher velocities a flow should experience less drag. Several arguments have been proposed to explain how subaqueous clay-laden flows may experience low drags. The two major arguments are: 1) Hydroplaning (Mohrig et al., 1998), and 2) High levels of flow stratification (Kneller et al., 2016).

Hydroplaning occurs when a debris flow cannot displace the ambient fluid from its path fast enough and consequently hovers over the substrate on a thin film of fluid (Mohrig et al., 1998). Although the practicality of hydroplaning as a cause for drag reduction on the head of debris flows has been confirmed experimentally (Mohrig et al., 1998), it seems unlikely that the same reasoning can be applied for the remainder of the flow, i.e., its body and tail.

Due to the force of gravity, a clay-laden flow stratifies such that the heavier grains are closer to the bed and the lighter ones are further above the bed (Cantero et al., 2011). This stratification promotes turbulence damping at the interface where the debris flow and the overlying water meet and can therefore result in reduced energy dissipation, higher velocities, and consequently longer run-out distances (Kneller et al., 2016). While flow stratification as a cause for longer run-outs has been tested numerically, it solely takes into account the friction drag at the debris flow-water interface, which is negligible compared to the friction drag between the debris flow and the underlying bed.

Small scale experiments, aimed at testing the effect of sediment composition on the run-out distance of clay-laden flows, show that increasing the clay content in a flow initially enhances the run-out distance. However, addition of too much clay leads to very viscous flows with shorter travel distances (De Haas et al., 2015).

Research on the rheology of clay-water suspensions has revealed the existence of two yield stresses in these suspensions. Inclined plane experiments have shown that if a clay-water suspension with a given thickness begins to flow on a given slope, it will stop only when the thickness is reduced dramatically or when the slope is decreased considerably (Coussot et al., 2002a,b). This phenomenon is a consequence of the existence of two yield stresses. One that governs the initiation of the flow from rest and is known as

the static or the pre-failure yield stress, τ_y, and the other which governs the abrupt stoppage/freezing of the flow and is known as the dynamic or the critical yield stress, τ_c. The static yield stress is larger than the critical yield stress. Therefore, following the initiation of the flow, the friction drag that is experienced by the mixture at the bed is reduced. The extent of this drag reduction is dictated by the difference between the two yield stresses. Consequently, it is suggested that $\tau_y - \tau_c$ is the factor that, to a large extent, controls the run-out distance of clay-laden flows.

3.2.1. THEORY

For a steady flow in equilibrium with only gravity and shear stress forces, the momentum equation can be written as,

$$(\rho - \rho_w)\, g \sin(\theta) = \frac{d\tau}{dz}, \tag{3.1}$$

where, τ is the shear stress, ρ and ρ_w are the debris flow and water densities, θ is the bed slope, and g is the gravitational acceleration.
Consider now the slab of sediment in Figure 3.1(a), and increase the bed angle to the point where the slab is just about to flow. The slab in this case is in a static and equilibrium state and the stress at the bottom of the slab, τ_b, is almost equal to τ_y. Equation (3.1) can be integrated for this case from the bed to the top of the slab to obtain,

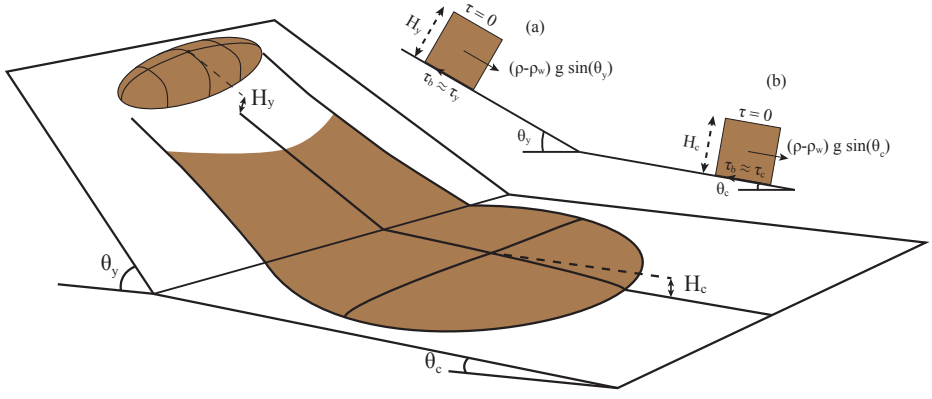

Figure 3.1: A slab of sediment moving from (a) the proximal to (b) the distal regions. τ_b, τ_y, and τ_c are the bed shear stress, the static yield stress, and the critical yield stress, respectively. θ_y and θ_c are the yield and the freeze slopes.

$$(\rho - \rho_w)\, g \sin(\theta_y) H_y = \tau_y, \tag{3.2}$$

where, θ_y is the angle at which the slab initially begins to flow and H_y is the height of the slab.
Now consider the same slab of sediment at the end of its journey when it has just come

to a static equilibrium state (Figure 3.1(b)). The stress at the bottom of the slab is now almost equal to τ_c. Integrating equation (3.1) for this case yields,

$$(\rho - \rho_w)\, g \sin(\theta_c) H_c = \tau_c, \tag{3.3}$$

where, θ_c is the angle at which the slab freezes and H_c is the height of the slab. Assuming $H_y = H_c = H$, and subtracting equation (3.3) from (3.2) yields,

$$(\rho - \rho_w)\, g\, (\sin(\theta_y) - \sin(\theta_c))\, H = \tau_y - \tau_c. \tag{3.4}$$

On the other hand, assuming $\theta_y = \theta_c = \theta$, and subtracting equation (3.3) from (3.2) yields,

$$(\rho - \rho_w)\, g \sin(\theta)(H_y - H_c) = \tau_y - \tau_c. \tag{3.5}$$

From equation (3.4), it can be seen that if $\tau_c \ll \tau_y$, then $\theta_c \ll \theta_y$, and therefore, for the flow to stop, the slope has to decrease dramatically. From equation (3.5), it can be seen that if $\tau_c \ll \tau_y$, then $H_c \ll H_y$, and therefore, for the flow to stop, the flow height has to decrease dramatically. Consequently, if $\tau_c \ll \tau_y$, then for the flow to stop, either the slope has to decrease dramatically, the flow height has to decrease considerably, or a less dramatic combination of the two cases has to occur.

3.2.2. RHEOMETRY TESTS

To assess the magnitude of the critical yield stress with respect to the static yield stress, a set of strain controlled rheometry tests were performed on the mixtures of kaolinite clay, sand, and water (details of these tests are explained in Chapter 4). Figure 3.2 shows the transient stress versus strain rate curves that were obtained from the measurements. The values of the static and the critical yield stresses approximated from these curves suggest that for low clay concentrations ($\leq 21\%$), the critical yield stress can be much smaller than the static yield stress (~ 10 times). The data also suggests that τ_c grows for higher concentrations. Nonetheless, nothing can be concluded from this data regarding whether the quantity $\tau_y - \tau_c$, in reality has a maximum or not.

3.3. EQUILIBRIUM STATE FOR CLAY-LADEN FLOWS

Consider a particle sitting on the continental shelf. Before a triggering event sets off its motion, this particle is at rest and hence in an equilibrium state. Once the motion commences, this particle starts to move and its momentum begins to build up in time. Now imagine the same particle at the end of its journey. In this case, the momentum of this particle decreases in time until it comes to a standstill, which is again an equilibrium state. It is a consequence of the generalization of Rolle's theorem that the particle reaches at least one equilibrium point between the time it starts to build up momentum and the time it comes to a standstill (Figure 3.3). At this equilibrium point the rate of change of momentum, p, of the particle is zero and therefore the forces on the particle balance each other out.

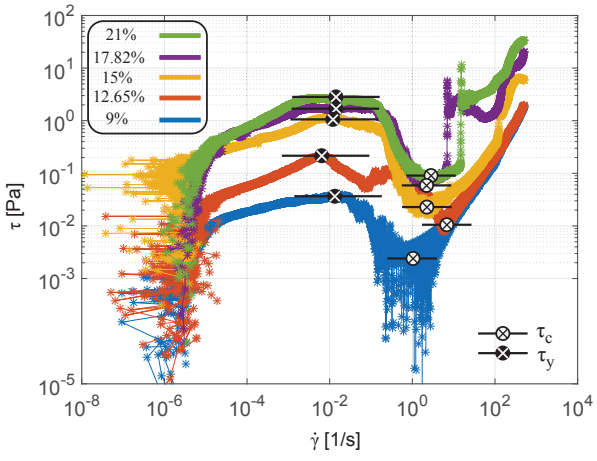

Figure 3.2: Transient stress versus strain rate plots for mixtures with 9%, 12.65%, 15%, 17.82%, and 21% sediment volume concentration. Approximated static and critical yield stresses, τ_y and τ_c, are depicted with white crosses in black circles and black crosses in white circles, respectively.

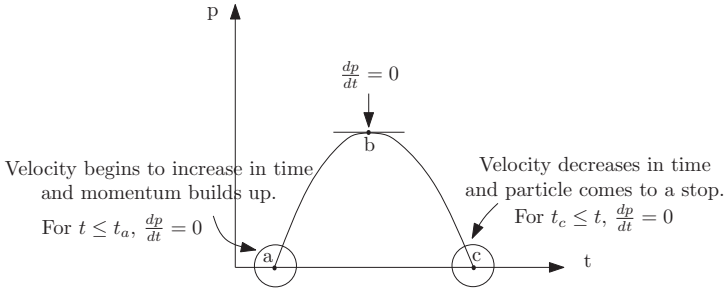

Figure 3.3: 1D plot of momentum vs. time. There exists at least one stationary point b, between points a and c.

Now that we have established that every individual particle within a gravity flow reaches the equilibrium state at least once during its journey from the proximal to the distal regions, let us consider a gravity flow as an ensemble of n particles. The linear momentum of this flow, P_{flow}, at a given instant can be obtained by summing up the momentum contributions of all the individual particles within the flow at that instant, and can be related to the forces acting on the system as follows,

$$\frac{d}{dt}\left(\sum_{i=1}^{n} m_i v_i\right) = \frac{d}{dt}\left(M v_G\right) = \dot{P}_{flow} = F, \tag{3.6}$$

where, m_i and v_i are the mass and the velocity of particle i, $M = \sum_i m_i$, is the total mass, v_G is the velocity of the center of mass of the flow, and F is the sum of all external and internal forces acting on the system (Figure 3.4).
Figure 3.5 depicts the momentum curve of a hypothetical gravity flow consisting of four particles. Erosion and deposition are incorporated in this figure by allowing some parti-

cles to be picked up by the flow and some particles to come to rest earlier than the whole flow. It can be deduced that similar to an individual particle, a gravity flow as a whole will reach the equilibrium state at least once during its journey. Note that for the flow as a whole to be in equilibrium, it is not necessary that all the particles, which make up the flow, be in the equilibrium state. However, this is a sufficient condition.

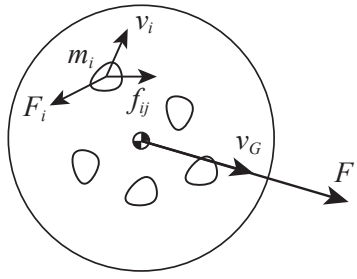

Figure 3.4: Schematics of a system of particles. f_{ij} represents the force exerted on particle i by particle j, F_i is the sum of all external forces acting on particle i, and F is the sum of all forces on the system enclosed within the circle.

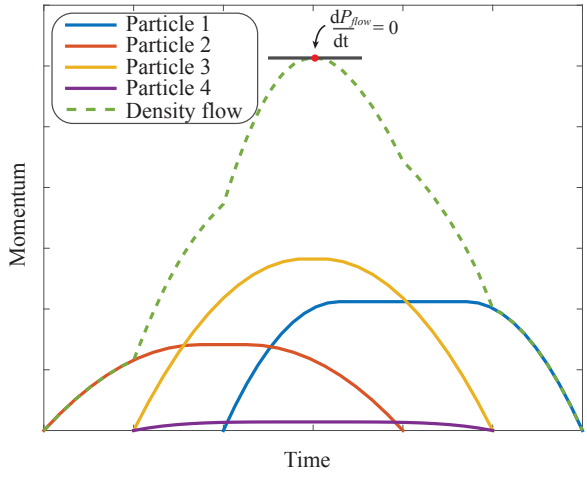

Figure 3.5: Momentum curve of a hypothetical gravity flow consisting of four particles.

Figure 3.6 depicts a simplified global model of the journey of a gravity flow from the proximal to the distal regions, containing an initial speeding up phase, an equilibrium phase, and a slowing down and coming to rest phase.

Previous research has shown that the presence of cohesive particles in gravity flows can boost their ability to resist disturbances and promote turbulence damping (Best & Leeder, 1993; Li & Gust, 2000; Wang et al., 1998; Winterwerp, 2001; Winterwerp et al., 2009). For a concentration higher than the gelling concentration, clay particles, through

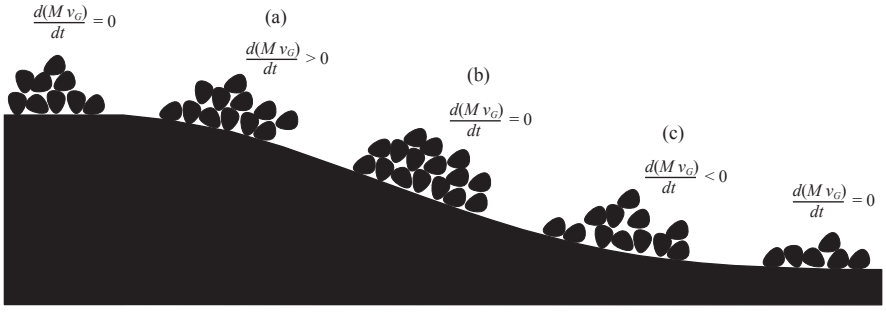

Figure 3.6: Simplified model of the journey of a density current from the proximal to the distal regions, containing an initial speeding up phase (a), an equilibrium phase (b), and a slowing down and coming to rest phase (c).

flocculation, can create a structured fluid (Coussot, 1997; Coussot & Piau, 1994; Toorman, 1997; Winterwerp & van Kesteren, 2004). Therefore, it takes energy to break up the resulting structure. Consequently, concentrated clay-laden flows are less prone to deviations from the equilibrium state in response to the outside disturbances. Therefore, it can be expected that once these cohesive flows reach the equilibrium condition, they can stay close to it for longer periods of time compared to their non-cohesive counterparts.

3.4. CONCLUSIONS

The run-out distance of clay-laden subaqueous gravity flows is significantly influenced by the presence of clay. While flow initiation for sediment-water suspensions is controlled by the static yield stress, its stoppage is dictated by the critical yield stress. Therefore, the difference between the static and the critical yield stresses, to a large extent, governs the run-out distance of clay-laden flows.

For kaolinite clay, sand, and water mixtures, it was shown that the critical yield stress can be much smaller than the static yield stress. Therefore, for a flow of this mixture to stop, either the slope has to decrease dramatically, the flow height has to decrease considerably, or a less dramatic combination of these two cases has to occur.

Furthermore, it was demonstrated that, regardless of the regime, all gravity flows reach the equilibrium state at least once during their journey from the proximal to the distal regions. In clay-laden flows, the electrostatic charge of the clay particles drives more and more particles to participate in forming a structured fluid. Consequently, the instance that most particles reach the equilibrium state is synced and the duration that individual particles spend close to the equilibrium state is prolonged.

From this study it can be concluded that the numerical models which aim to accurately simulate the run-out distance of clay-laden flows should at the very least employ constitutive models that can reproduce the rheological behavior of sediment-water suspensions. Such a model will be developed in the next chapter.

REFERENCES

Baker, M. L., Baas, J. H., Malarkey, J., Silva Jacinto, R., Craig, M. J., Kane, I. A., & Barker, S. (2017). The Effect of Clay Type On The Properties of Cohesive Sediment Gravity Flows And Their Deposits. *Jornal of Sedimentary Research*, *87*, 1176–1195. doi: 10.2110/jsr.2017.63

Best, J. L., & Leeder, M. R. (1993). Drag reduction in turbulent muddy seawater flows and some sedimentary consequences. *Sedimentology*, *40*, 1129–1137. doi: 10.1111/j.1365-3091.1993.tb01383.x

Cantero, M. I., Cantelli, A., Pirmez, C., Balachandar, S., Mohrig, D., Hickson, T. A., … Parker, G. (2011). Emplacement of massive turbidites linked to extinction of turbulence in turbidity currents. *Nature Geoscience*, *5*(1), 42–45. doi: 10.1038/ngeo1320

Coussot, P. (1997). *Mudflow Rheology and Dynamics*. Taylor & Francis.

Coussot, P., Nguyen, Q. D., Huynh, H. T., & Bonn, D. (2002a). Avalanche behavior in yield stress fluids. *Physical Review Letters*, *88*(17), 1755011–1755014. doi: 10.1103/PhysRevLett.88.175501

Coussot, P., Nguyen, Q. D., Huynh, H. T., & Bonn, D. (2002b). Viscosity bifurcation in thixotropic, yielding fluids. *Journal of Rheology*, *46*(3), 573–589. doi: 10.1122/1.1459447

Coussot, P., & Piau, J. M. (1994). On the behavior of fine mud suspensions. *Rheologica Acta*, *33*(3), 175–184. doi: 10.1007/BF00437302

De Blasio, F. V. (2004). Hydroplaning and submarine debris flows. *Journal of Geophysical Research*, *109*(C1), C01002. doi: 10.1029/2002JC001714

De Haas, T., Braat, L., Leuven, J. R., Lokhorst, I. R., & Kleinhans, M. G. (2015). Effects of debris flow composition on runout, depositional mechanisms, and deposit morphology in laboratory experiments. *Journal of Geophysical Research F: Earth Surface*, *120*(9), 1949–1972. doi: 10.1002/2015JF003525

Embley, R. W. (1976). New evidence for occurrence of debris flow deposits in the deep sea. *Geology*, *4*(6), 371–374. doi: 10.1130/0091-7613(1976)4<371:NEFOOD>2.0.CO;2

Gee, M. J. R., Masson, D. G., Watts, A. B., & Allen, P. A. (1999). The Saharan debris flow: an insight into the mechanics of long runout submarine debris flows. *Sedimentology*, *46*, 317–335. doi: 10.1046/j.1365-3091.1999.00215.x

Huang, X., & Garcia, M. H. (1998). A Herschel–Bulkley model for mud flow down a slope. *Fluid Mechanics*, *374*, 305–333. doi: 10.1017/S0022112098002845

Jacobi, R. D. (1976). Sediment slides on the northwestern continental margin of Africa. *Marine Geology*, *22*(3), 157–173. doi: 10.1016/0025-3227(76)90045-1

Jiang, L., & Le Blond, P. H. (1993). Numerical Modelling of an Underwater Bingham Plastic Mud Slide and the Waves which it Generates. *Journal of Geophysical Research*, *98*(C6), 10303–10317. doi: 10.1029/93JC00393

Kneller, B., Nasr-Azadani, M. M., Radhakrishnan, S., & Meiburg, E. (2016). Long-range sediment transport in the world's oceans by stably stratified turbidity currents. *Journal of Geophysical Research*, *121*(12). doi: 10.1002/2016JC011978

Legros, F. (2002). The mobility of long-runout landslides. *Geology, Engineering*, *63*, 301–331. doi: 10.1016/S0013-7952(01)00090-4

Li, M. Z., & Gust, G. (2000). Boundary layer dynamics and drag reduction in flows of high cohesive sediment suspensions. *Sedimentology*, *47*, 71–86. doi: 10.1046/j.1365-3091.2000.00277.x

Masson, D. G. (1996). Catastrophic collapse of the volcanic island of Hierro 15 ka ago and the history of landslides in the Canary Islands. *Geology*, *24*(3), 231–234. doi: 10.1130/0091-7613(1996)024<0231:CCOTVI>2.3.CO;2

Mohrig, D., Whipple, K. X., Hondzo, M., Ellis, C., & Parker, G. (1998). Hydroplaning of subaqueous debris flows. *GSA Bulletin*, *110*(3), 387–394. doi: 10.1130/0016-7606(1998)110<0387:HOSDF>2.3.CO;2

Pratson, L. F., Imran, J., Parker, G., Syvitski, J. P. M., & Hutton, E. (2000). *Debris Flows vs. Turbidity Currents: A Modeling Comparison of Their Dynamics and Deposits* (Vol. 72). American Association of Petroleum Geologists. doi: 10.1306/M72703C6

Talling, P. J., Masson, D. G., Sumner, E. J., & Malgesini, G. (2012). Subaqueous sediment density flows: Depositional processes and deposit types. *Sedimentology*, *59*, 1937–2003. doi: 10.1111/j.1365-3091.2012.01353.x

Talling, P. J., Wynn, R. B., Masson, D. G., Frenz, M., Cronin, B. T., Schiebel, R., … Amy, L. A. (2007). Onset of submarine debris flow deposition far from original giant landslide. *Nature*, *450*, 541–544. doi: 10.1038/nature06313

Toorman, E. a. (1997). Modelling the thixotropic behaviour of dense cohesive sediment suspensions. *Rheologica Acta*, *36*, 56–65. doi: 10.1007/BF00366724

Wang, Z. Y., Larsen, P., Nestmann, F., & Dittrich, A. (1998). Resistance and Drag Reduction of Flows of Clay Suspensions. *Journal of Hydraulic Engineering*, *124*(1), 41–49. doi: 10.1061/(ASCE)0733-9429(1998)124:1(41)

Winterwerp, J. C. (2001). Stratification effects by cohesive and noncohesive sediment. *Journal of Geophysical Research*, *106*(C10), 22559–22574. doi: 10.1029/2000JC000435

Winterwerp, J. C., Lely, M., & He, Q. (2009). Sediment-induced buoyancy destruction and drag reduction in estuaries. *Ocean Dynamics*, *59*, 781–791. doi: 10.1007/s10236-009-0237-y

Winterwerp, J. C., & van Kesteren, W. G. M. (2004). *Introduction to the Physics of Cohesive Sediment in the Marine Environment*. Elsevier.

4

A NEW RHEOLOGICAL MODEL FOR THIXOELASTIC MATERIALS IN SUBAQUEOUS GRAVITY DRIVEN FLOWS

The real voyage of discovery consists not in seeking new landscapes, but in having new eyes.

Marcel Proust

A new viscoelastic constitutive model for subaqueous clay-rich gravity flows is presented. It is explained that for the materials which exhibit a minimum in their strain controlled flow curves the structure parameter must be a symmetric function of the strain rate and the stress. Therefore, the destruction of structure within the material is modeled using the dissipation energy. An expression for the elastic strain of the flowing structure is derived. The final set of equations can reproduce the viscosity bifurcation that clay suspensions may exhibit under a given load. This is explained to be important for the prediction of the run-out distance of clay-rich gravity flows. The ability of the model to reproduce the general response of pasty materials to step stress and step shear rate tests is examined. The model requires four empirical parameters. A methodology is presented for obtaining these parameters and power law functions are given for their calculations for a limited rest time of 3000 s. The ability of the model to reproduce the rheological behavior that clay-rich suspensions exhibit under both stress and strain controlled conditions is examined using rheometry tests.

This chapter has been published in the Journal of Non-Newtonian Fluid Mechanics 266, 102-117 (2019).

4.1. INTRODUCTION

CLAY is present in the majority of deep marine (Baker et al., 2017), coastal (Healy et al., 2002; Winterwerp & van Kesteren, 2004), and fluvial environments (Van Maren et al., 2009). For clay-rich gravity flows, presence of clay greatly influences the run-out distance and the internal structure of these flows (Baas et al., 2016; Coussot et al., 2005). Using their inclined plane experiments, Coussot et al. (2002a,b) showed that under a given load, clay suspensions experience viscosity bifurcation, i.e., they either stop flowing altogether or experience a discontinuous decrease in their viscosity depending on their structural state at the time of the applied stress. They concluded that, for strain controlled measurements, stable flows can occur only when the shear rate is above a critical value. For smaller shear rates the material either fractures or shows shear banding instabilities (Pignon et al., 1996). These experiments also showed that if a clay-water suspension with a given thickness begins to flow on a certain slope, it will stop only when the thickness is reduced dramatically or when the slope is decreased considerably. This phenomenon is a consequence of the existence of two yield stresses. One which governs the initiation of the flow from rest and is known as the static yield stress, τ_y, and the other which governs the abrupt stoppage/freezing of the flow and is known as the dynamic or critical yield stress, τ_c. The static yield stress is larger than the critical yield stress and the difference between the two is the factor which governs the run-out distance of clay-water suspensions. The model which will be presented here can capture both the static and the critical yield stresses of clay-water suspensions, and therefore, can be used to accurately simulate the run-out distance of gravity flows.

The most complete anatomy of subaqueous clay-rich gravity flows is composed of three vertically stacked layers (Hermidas et al., 2018). These three regions are characterized in Figure 4.1(a), which depicts the velocity profile of a clay-rich sediment gravity flow during small scale flume experiments (Hermidas et al., 2018).

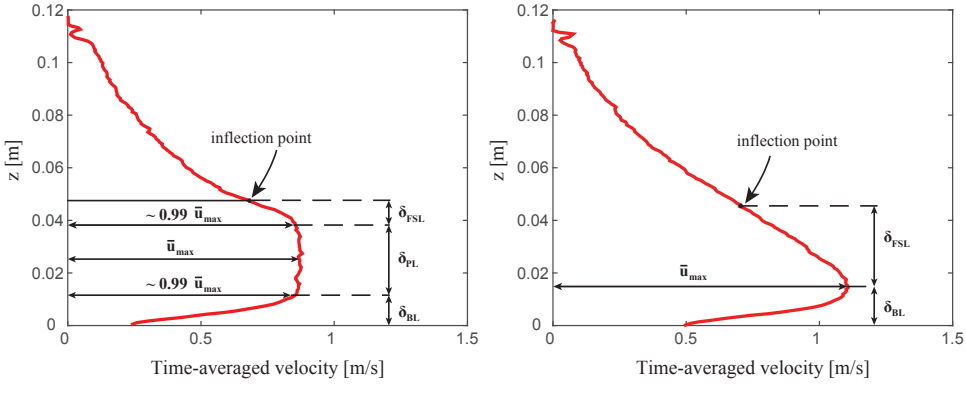

(a) Velocity profile of a 21% concentration gravity flow

(b) Velocity profile of a 9% concentration gravity flow

Figure 4.1: Free shear layer, δ_{FSL}, plug layer, δ_{PL}, and boundary layer, δ_{BL}, regions of sediment gravity flows captured using an Ultrasonic Doppler Velocity probe (Hermidas et al., 2018).

The density and velocity gradients that exist on the interface between the sediment flow and the overlying water result in a dilute mixing layer known as the free shear layer.

Due to low sediment concentration, the fluid within this layer behaves similar to a Newtonian fluid. The free shear layer is stacked on top of a layer referred to as the plug layer. The behavior of the mixture within this layer resembles that of a gel-like suspension whose yield stress is reached on the interface where the free shear layer and the plug layer meet. The existence and size of the plug layer is dependent on the sediment concentration, and for dilute sediment gravity flows it disappears, as shown in Figure 4.1(b). Due to the no slip condition between the sediment flow and the bed, the plug layer in the vicinity of the bed is liquefied, producing a third layer known as the boundary layer. The fluid within this layer behaves as a viscoelastic fluid.

Modeling approaches for these flow structures are problematic due to the complex behavior of clay-water suspensions. Clay particles are flat platelets with electrostatically charged surfaces. Once immersed in high concentrations (higher than the 'gelling' concentration) in a medium such as water, they can form two types of structures, namely, the 'card-house flocs' and 'card-pack aggregates' (Michaels & Bolger, 1962). Presence of these structures are characteristic of many clay-water suspensions which exhibit viscoelastic, yield, shear thinning, and thoxitropic behavior (Billingham & Ferguson, 1993). Thixotropy is generally viewed as the time-dependent decrease in the apparent viscosity of a fluid under shear due to the break down of the structure (Coussot et al., 2002b). Recovery of a damaged structure ensues once shearing is removed. The concept of simultaneous break down and build up of structure was first discussed by Goodeve (1939). Subsequent models of Moore (1959), Hahn et al. (1959), and Peter (1964) aimed at capturing these simultaneous processes by a rate equation for a scalar structure parameter that is incorporated in the constitutive model. Generalization of these models for the special case of steady, homogeneous, incompressible, irrotational flows, came following the work of Rivlin (Billingham & Ferguson, 1993; Cheng & Evans, 1965; Hewitt & Balmforth, 2013; Rivlin, 1948, 1949). For more general flows, different variations of these models are usually considered where various material characteristics such as the yield stress (Dimitriou & McKinley, 2014; Toorman, 1997), the elastic modulus, and/or the viscosity are considered to be functions of the structure parameter (Acierno et al., 1976; Coussot et al., 1993; De Kee & Chan Man Fong, 1994; de Souza Mendes, 2009; Fong et al., 1996; Yziquel et al., 1999). These functions are generally constructed in such a way as to reproduce the overall behavior of the material.

In contrast to this group of models, which are based on the bulk rheological behavior of the material, a separate branch has evolved over the years which adopts a microstructural approach. The constitutive relations in these models are emergent from the physical considerations regarding the interactions between the material's microstructural constituents (Bocquet et al., 2009; Falk & Langer, 1998; Fielding et al., 2000; Sollich et al., 1997). While the level of abstraction that these models possess and their added intuition from the microstructural approach is appealing, considerable mathematical manipulation is usually required to express them in terms of macroscopic variables. Therefore, they have not often been employed to describe experimental data sets. The bulk rheological models on the other hand, such as those of Mujumdar et al. (2002) or Dullaert & Mewis (2006), are written explicitly in terms of the bulk parameters and are therefore easier to employ in engineering applications.

Nonetheless, construction of such bulk models can suffer from ambiguities regarding

how various relations should be constructed. One ambiguity has to do with the way the structure model is formulated. For instance, the destruction of structure in such models has been related to various invariants of the deviatoric stress and/or the strain rate tensors depending on the material and the flow field characteristics (Yziquel et al., 1999). Here we will remove this ambiguity by resorting to physical symmetry arguments.
In this study a new rheological model is presented which can be used for modeling clay-rich gravity flows. In order to capture the anatomy of these flows, from the outset a constitutive model is favored that can reproduce the creep behavior of the plug layer, the yielding at the base of the plug, and the visco-elastic behavior within the boundary layer. The Kelvin-Voigt model is here considered very applicable for the elastic solid and the yield regimes, and suitable for the viscous fluid regime. Therefore, similar to the approach taken by Mujumdar et al. (2002), the total stress is split into an elastic and a viscous part. However, in contrast to their approach, an expression for the elastic strain of the flowing structure is not assumed. Instead, such an expression is derived based on the structure model and by assuming spring like interactions between clay particles at the micro-scale. This reduces the number of empirical parameters required by the model. The generation and the destruction of structure are accounted for using a structure model based on the model of Yziquel et al. (1999).
We will discuss how the final equations capture the viscosity bifurcation and the yielding and freezing behavior that clay suspensions display under a given load. This is important for accurate prediction of the run-out distance of gravity flows. The most general flow curves which are allowed by the model are discussed. The model response to constant stress and constant shear rate inputs are analyzed (Coussot et al., 2006; de Souza Mendes, 2009; Derec et al., 2003; Dullaert & Mewis, 2006).
The final constitutive model requires four empirical parameters. A methodology is presented for obtaining these parameters and power law functions are given for their calculation, assuming complete structure recovery within a limited amount of rest time. We will show that the model is capable of reproducing the rheological behavior that clay-rich suspensions may exhibit in both stress and strain controlled flow conditions which exist within the free shear and boundary layers of clay-laden environmental flows. This is achieved by comparing the output of the model with stress and strain controlled measurements obtained from rheometry tests.

4.2. RHEOLOGICAL MODEL

4.2.1. CONNECTING MICROSCALE BEHAVIOR TO A MACRO SCALE MODEL

At very short distances two clay particles exert a repulsive force on each other (Born repulsion). At longer distances, this repulsive force is overcome by the Van der Waals attraction and therefore two clay particles attract each other. In the absence of other forces, the addition of these two forces results in an equilibrium distance corresponding to the balance of the Born repulsion with the Van der Waals attraction (Coussot, 1997; Olphen, 1977). A net repulsive force is generated when the particles are brought inside the equilibrium distance, and a net attractive force when the particles are brought outside the equilibrium distance. Therefore, at short distances the interaction of clay particles can be modeled by springs. Although it is known that at long distances two clay particles

may exert a net repulsive force on each other (Coussot, 1997), here we assume that this force is weak and the interaction can be modeled as if the spring between the particles is broken.

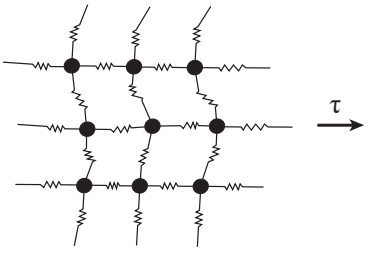

Figure 4.2: Clay particle network.

Consider a force applied to a homogeneous and isotropic network of clay particles connected together with springs as in Figure 4.2. Following the homogeneity and the isotropy assumptions, away from the boundaries, the direction in which a force is applied to this network is irrelevant. Furthermore, once equilibrium is reached the internal forces cancel out and the applied force is counteracted by the sum of all the forces that are associated with strains in the direction of the applied force. However, the amount of strain that the whole network experiences in the direction of the applied force is different from the amount of strain that each individual spring experiences. Therefore, to relate the total strain of the network to that of individual springs, we assume that all the springs experience the same strain in the direction of the applied force as that of the total network and instead modify their stiffnesses, G_i's, such that the total reaction force becomes equal to the applied external force. Thus, the complex system of springs in Figure 4.2 can be reduced to the one shown in Figure 4.3. A general form of equivalence between the model networks is discussed by Roscoe (1950), by resorting to electrical network theory.

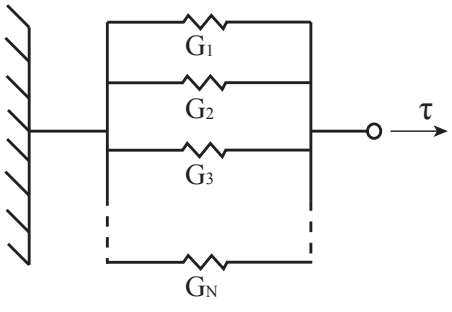

Figure 4.3: The simplified clay particle network model.

The resultant strain, γ_r, of the system under an applied force is a residual or storage deformation that the material exhibits or recovers in the future in a stress-free state. The liquid matrix surrounding this particle network provides a viscous contribution to the total stress and is incorporated by adding a dashpot in parallel to the collection of

springs. As stress is applied, some connections are destroyed and some are created (this point is more thoroughly explained in the next section). We define the modulus of elasticity, G_0, as $\sum_{i=1}^{N} \frac{G_i}{N} = \frac{G_0}{N_0}$, where N is the number of current connections and N_0 is the number of connections of a completely structured material. The resulting clay particle model, depicted in Figure 4.4, can be written as,

$$\begin{aligned} \tau_d + \tau_{s_1} + \tau_{s_2} + \cdots + \tau_{s_N} &= \tau \;\Rightarrow \\ \tau_d + \gamma_r G_1 + \gamma_r G_2 + \cdots + \gamma_r G_N &= \tau \;\Rightarrow \\ \tau_d + \gamma_r \frac{NG_0}{N_0} = \tau_d + G_0 \gamma_r \lambda &= \tau, \end{aligned}$$

where, the stresses, τ's, are defined in Figure 4.4, and $\lambda = \frac{N}{N_0} = \sum_{i=1}^{N} \frac{G_i}{G_0}$, is the structure parameter with range $[0,1]$. Furthermore, $\tau_d = \mu\dot{\gamma}$, where μ is the viscosity of the material at $\lambda = 0$, and $\dot{\gamma}$ is the strain rate tensor. Therefore, the resulting constitutive model is,

$$\tau = \mu\dot{\gamma} + \gamma_r \frac{NG_0}{N_0} = \tau_d + G_0 \gamma_r \lambda. \tag{4.1}$$

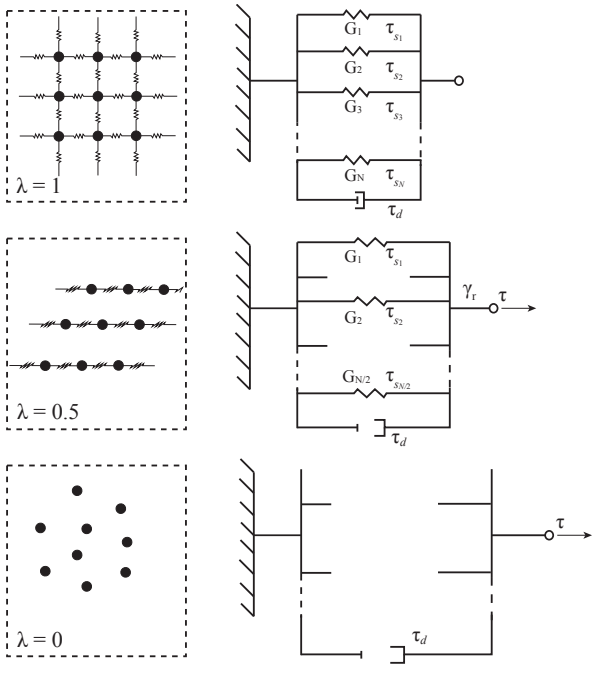

Figure 4.4: The simplified clay particle network model with complete structure ($\lambda = 1$), top, with half the structure ($\lambda = 0.5$), middle, and with no structure ($\lambda = 0$), bottom.

4.2.2. STRUCTURE MODEL

Experiments have shown that stress and strain controlled measurements performed on clay-water suspensions result in different flow curves. In their work on lubricating greases Mas & Magnin (1994) observed that the flow curves obtained from strain controlled tests showed a minimum stress. The same flow curves obtained using stress controlled tests however, did not show such a minimum. Nonetheless, the failure which occurs within the structure of clay-water suspensions when yielding is the same for the two types of test. This signifies that the structure parameter cannot be a function of only stress or only strain but rather a combination of both that is independent of the type of test that is performed. In this respect energy is a viable choice. Therefore, following the work of Moore (1959) and Yziquel et al. (1999) the time rate of change of the structure parameter is written as,

$$\frac{d\lambda}{dt} = \alpha(1-\lambda) - |\tau : \dot{\gamma}|\beta\lambda. \tag{4.2}$$

The first term on the right hand side of (4.2) represents generation of structure by the Brownian motion. The second term, $|\tau : \dot{\gamma}|$, captures the change in the internal energy of a fluid volume due to the application of a stress or a strain rate (Bird et al., 1987). Once a stress or a strain rate is applied to the suspension, it damages the structure (i.e., breaks some connections). This damage can also be seen in the increase in the internal energy of the system. Therefore, the increase in the internal energy is used to indicate destruction of structure. Note that equation (4.2) is symmetric with respect to $\dot{\gamma}$ and τ. In (4.2), α and β are empirical parameters which should be determined through experiments.

4.2.3. RESIDUAL STRAIN MODEL

Let $\sum_{i=1}^{N} \tilde{\gamma}_i(t)\tilde{G}_i$ represent the force applied to a clay particle network with N number of connections at a given time t. Following the dynamics of the system undergoing a deformation with a strain rate $\dot{\gamma}$, at a later time $t+\Delta t$, let us assume that M number of connections remain, D number of connections are destroyed, and C number of connections are newly created. The strain of the remaining, $N-D=M$, connections at $t+\Delta t$ can be written as,

$$\gamma(t+\Delta t) \approx \dot{\gamma}\Delta t + \tilde{\gamma}(t),$$

which results in the following expression for the force applied to the clay particle network at time $t+\Delta t$,

$$\sum_{i=1}^{M} \left(\dot{\gamma}\Delta t + \tilde{\gamma}_i(t)\right)\tilde{G}_i + \sum_{i=1}^{C} \gamma_i G_i, \tag{4.3}$$

where, γ_i and G_i are the strains and the stiffnesses of the newly created connections, respectively. Furthermore, from the definition of the residual strain one has,

$$\sum_{i=1}^{N} \tilde{\gamma}_i(t)\tilde{G}_i = \gamma_r(t)\sum_{i=1}^{N} \tilde{G}_i = \gamma_r(t)\frac{N}{N_0}G_0 \;\Rightarrow\; \gamma_r(t) = \frac{\sum_{i=1}^{N} \tilde{\gamma}_i(t)\tilde{G}_i}{\frac{N}{N_0}G_0}. \tag{4.4}$$

Similarly, from (4.3), for the residual strain $\gamma_r(t+\Delta t)$ one has,

$$\sum_{i=1}^{M}\left(\dot{\gamma}\Delta t+\tilde{\gamma}_i(t)\right)\tilde{G}_i+\sum_{i=1}^{C}\gamma_i G_i = \gamma_r(t+\Delta t)\sum_{i=1}^{M+C}\widehat{G}_i=\gamma_r(t+\Delta t)\frac{M+C}{N_0}G_0 \Rightarrow$$
$$\gamma_r(t+\Delta t) = \frac{\sum_{i=1}^{M}\left(\dot{\gamma}\Delta t+\tilde{\gamma}_i(t)\right)\tilde{G}_i+\sum_{i=1}^{C}\gamma_i G_i}{\frac{M+C}{N_0}G_0}. \tag{4.5}$$

Subtracting (4.4) from (4.5) and dividing by Δt yields,

$$\frac{\gamma_r(t+\Delta t)-\gamma_r(t)}{\Delta t} = \frac{\sum_{i=1}^{M}\left(\dot{\gamma}\Delta t+\tilde{\gamma}_i(t)\right)\tilde{G}_i+\sum_{i=1}^{C}\gamma_i G_i}{\frac{M+C}{N_0}G_0\Delta t}-\frac{\sum_{i=1}^{N}\tilde{\gamma}_i(t)\tilde{G}_i}{\frac{N}{N_0}G_0\Delta t} \Rightarrow \ldots$$
$$\ldots=\left(\frac{N_0}{M+C}\right)\sum_{i=1}^{M}\frac{\dot{\gamma}\tilde{G}_i}{G_0} + \left(\frac{N_0}{M+C}\right)\sum_{i=1}^{C}\frac{\dot{\gamma}G_i}{G_0}+\left(\frac{M}{M+C}-1\right)\frac{\gamma_r(t)}{\Delta t} \Rightarrow \ldots$$
$$\frac{\gamma_r(t+\Delta t)-\gamma_r(t)}{\Delta t} = \dot{\gamma}-\left(\frac{C}{M+C}\right)\frac{\gamma_r(t)}{\Delta t}. \tag{4.6}$$

Using the structure model (4.2) in equation (4.6), $C=N_0\Delta t\alpha(1-\lambda(t))$ and $M+C=N_0\lambda(t+\Delta t)$, which for $\Delta t\to 0$, yields,

$$\frac{d\gamma_r}{dt}=\dot{\gamma}-\frac{\alpha(1-\lambda)}{\lambda}\gamma_r. \tag{4.7}$$

Combining (4.1), (4.2), and (4.7), results in the following rheological model,

$$\tau = G_0\lambda\gamma_r+\mu\dot{\gamma}, \tag{4.8}$$
$$\dot{\lambda} = \alpha(1-\lambda)-|\tau:\dot{\gamma}|\beta\lambda, \tag{4.9}$$
$$\dot{\gamma}_r = \dot{\gamma}-\frac{\alpha(1-\lambda)}{\lambda}\gamma_r. \tag{4.10}$$

4.2.4. THREE-DIMENSIONAL FORMULATION OF THE RHEOLOGICAL MODEL FOR SIMPLE SHEAR FLOWS

The expression for the total stress tensor, σ, within a fluid can be written as,

$$\sigma=p\delta+\tau. \tag{4.11}$$

where, p is the thermodynamic pressure, δ is the unit tensor, and τ is the stress tensor. For isotropic fluids in simple shear flow depicted in Figure 4.5, the stress tensor can be written as (Bird et al., 1987; Tanner, 2000),

$$\tau=\begin{pmatrix}\tau^{11} & \tau^{21} & 0\\ \tau^{21} & \tau^{22} & 0\\ 0 & 0 & \tau^{33}\end{pmatrix}. \tag{4.12}$$

The components of the strain tensor can be written as $\gamma^{ij}=\delta-g^{ij}$, where g^{ij} is the inverse of the metric tensor. This yields,

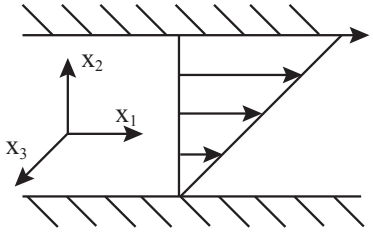

Figure 4.5: Simple shear flow.

$$\gamma = \begin{pmatrix} -\gamma^{21^2} & \gamma^{21} & 0 \\ \gamma^{21} & 0 & 0 \\ 0 & 0 & 0 \end{pmatrix}. \tag{4.13}$$

The strain rate tensor can be written as,

$$\dot{\gamma} = (\nabla v + \nabla v^T) = \begin{pmatrix} 0 & \dot{\gamma}^{21} & 0 \\ \dot{\gamma}^{21} & 0 & 0 \\ 0 & 0 & 0 \end{pmatrix}. \tag{4.14}$$

From the definition of the residual strain and assuming linearity between the stain and the residual strain tensors yields,

$$\gamma_r^{ks} = \frac{G_{ij}^{--ks}\gamma^{ij}}{\lambda G_0}. \tag{4.15}$$

where, the elastic modulus, G_{ij}^{--ks}, is a fourth-rank tensor.
Assuming a homogeneous and isotropic material yields (Tanner, 2000),

$$\gamma_r = \begin{pmatrix} \gamma_r^{11} & \gamma_r^{21} & 0 \\ \gamma_r^{21} & \gamma_r^{22} & 0 \\ 0 & 0 & \gamma_r^{22} \end{pmatrix}. \tag{4.16}$$

Using the fact that the Christoffel symbols, $\Gamma_{kl}^{i} = \frac{1}{2} g^{im}\left(\frac{\partial g_{mk}}{\partial x_l} + \frac{\partial g_{ml}}{\partial x_k} - \frac{\partial g_{kl}}{\partial x_m}\right) = 0$, and taking the time derivative of (4.16) and its basis vectors yields (Bird et al., 1987),

$$\dot{\gamma}_r = \frac{\partial}{\partial t}\begin{pmatrix} \gamma_r^{11} & \gamma_r^{21} & 0 \\ \gamma_r^{21} & \gamma_r^{22} & 0 \\ 0 & 0 & \gamma_r^{22} \end{pmatrix} - \begin{pmatrix} 2\dot{\gamma}^{21}\gamma_r^{21} & \dot{\gamma}^{21}\gamma_r^{22} & 0 \\ \dot{\gamma}^{21}\gamma_r^{22} & 0 & 0 \\ 0 & 0 & 0 \end{pmatrix}. \tag{4.17}$$

Finally, the three-dimensional formulation of the equations (4.8)-(4.10) for the case of the simple shear flow can be written as,

$$\begin{pmatrix} \tau^{11} & \tau^{21} & 0 \\ \tau^{21} & \tau^{22} & 0 \\ 0 & 0 & \tau^{33} \end{pmatrix} = G_0\lambda \begin{pmatrix} \gamma_r^{11} & \gamma_r^{21} & 0 \\ \gamma_r^{21} & \gamma_r^{22} & 0 \\ 0 & 0 & \gamma_r^{22} \end{pmatrix} + \mu \begin{pmatrix} 0 & \dot{\gamma}^{21} & 0 \\ \dot{\gamma}^{21} & 0 & 0 \\ 0 & 0 & 0 \end{pmatrix}, \tag{4.18}$$

$$\dot{\lambda} = \alpha(1-\lambda) - |\tau : \dot{\gamma}|\beta\lambda, \tag{4.19}$$

$$\frac{\partial}{\partial t}\begin{pmatrix} \gamma_r^{11} & \gamma_r^{21} & 0 \\ \gamma_r^{21} & \gamma_r^{22} & 0 \\ 0 & 0 & \gamma_r^{22} \end{pmatrix} = \begin{pmatrix} 2\dot{\gamma}^{21}\gamma_r^{21} & \dot{\gamma}^{21}\gamma_r^{22} & 0 \\ \dot{\gamma}^{21}\gamma_r^{22} & 0 & 0 \\ 0 & 0 & 0 \end{pmatrix} + \begin{pmatrix} 0 & \dot{\gamma}^{21} & 0 \\ \dot{\gamma}^{21} & 0 & 0 \\ 0 & 0 & 0 \end{pmatrix} - \frac{(1-\lambda)\alpha}{\lambda}\begin{pmatrix} \gamma_r^{11} & \gamma_r^{21} & 0 \\ \gamma_r^{21} & \gamma_r^{22} & 0 \\ 0 & 0 & \gamma_r^{22} \end{pmatrix}. \tag{4.20}$$

4

The three-dimensional formulation of the equations (4.8)-(4.10) for the case of the vortex flow is given in Appendix A.

4.2.5. EVOLUTION OF THE STRUCTURE PARAMETER, λ, FOR VARIOUS VALUES OF STRESS

In equilibrium, the number of connections created equals the number of connections destroyed, therefore, $\dot{\lambda} = 0 \Rightarrow \lambda_e = \alpha/\left(\alpha + \beta|\tau : \dot{\gamma}|\right)$ and the rate of change of residual strain is zero, i.e., $\dot{\gamma}_r = 0$. Therefore,

$$\frac{d\gamma_r}{dt} = \dot{\gamma} - \frac{\gamma_r\alpha(1-\lambda_e)}{\lambda_e} = 0 \Rightarrow \gamma_r = \frac{\lambda_e\dot{\gamma}}{\alpha(1-\lambda_e)}. \tag{4.21}$$

Inserting (4.21) in (4.8) yields the effective viscosity,

$$\tau = \left(\frac{G_0\lambda_e^2}{\alpha(1-\lambda_e)} + \mu\right)\dot{\gamma} \Rightarrow \mu_e(\lambda_e) = \frac{G_0\lambda_e^2}{\alpha(1-\lambda_e)} + \mu. \tag{4.22}$$

Hence,

$$\dot{\gamma} = \frac{\tau\alpha(1-\lambda_e)}{G_0\lambda_e^2 + \mu\alpha(1-\lambda_e)}. \tag{4.23}$$

Inserting (4.23) in (4.9) yields,

$$\frac{d\lambda}{dt} = \alpha(1-\lambda_e) - \frac{\tau^2\alpha(1-\lambda_e)}{G_0\lambda_e^2 + \mu\alpha(1-\lambda_e)}\beta\lambda_e = 0, \tag{4.24}$$

which results in,

$$\alpha(1-\lambda_e)\left[1 - \frac{\tau^2\beta\lambda_e}{G_0\lambda_e^2 + \mu\alpha(1-\lambda_e)}\right] = 0. \tag{4.25}$$

The roots to (4.25) are,

$$\lambda_{e,y} = 1, \text{ and,} \tag{4.26}$$

$$\lambda_{e,\pm} = \frac{\mu\alpha + \beta\tau^2 \pm \sqrt{(\mu\alpha + \beta\tau^2)^2 - 4G_0\mu\alpha}}{2G_0}. \tag{4.27}$$

Only one solution to (4.27) exists when, $|\tau| = \sqrt{\left(\sqrt{4G_0\mu\alpha} - \mu\alpha\right)/\beta}$. This shear stress is called the critical stress, τ_c, and is the stress below which a flowing material comes to a stop.
At yield stress $\tau = \tau_y$, two solutions exist for (4.27), however, one of them coincides with (4.26). Inserting $\lambda_{e,y} = 1$ in (4.27) yields, $|\tau_y| = \sqrt{G_0/\beta}$. The other root, $\lambda_{e,-}$, can be obtained by inserting τ_y back into equation (4.27). This yields, $\lambda_{e,-} = \mu\alpha/G_0$. Once $\tau = \tau_y$, $\lambda_{e,-}$ is the stable solution where the structure will end up (since $\lambda_{e,y} = 1$ becomes unstable at this point and the material begins to flow).
Figure 4.6 depicts the development of the structure parameter, λ, for various initial structures, λ_0, under different constant stresses.
For stresses $\tau_c < \tau < \tau_y$, if the material is flowing, it will end up with a structure $\lambda_e = \lambda_{e,-} < 1$. However, if the material has not disintegrated, i.e., $\lambda_e < \lambda_{e,+}$, then it will end up at $\lambda_{e,y} = 1$.

4.2.6. EVOLUTION OF THE STRUCTURE PARAMETER, λ, FOR VARIOUS VALUES OF STRAIN RATE

Following the same procedure as in Section 4.2.5, and writing the stress in terms of the strain rate, equation (4.25) becomes,

$$\left(\beta G_0\dot{\gamma}^2\right)\lambda_e^3 - \left(\mu\dot{\gamma}^2\beta\alpha + \alpha^2\right)\lambda_e^2 + \left(\mu\dot{\gamma}^2\beta\alpha + 2\alpha^2\right)\lambda_e - \alpha^2 = 0. \tag{4.28}$$

For all the empirical parameters considered in this study (and perhaps for all appropriate values of β, G_0, $\dot{\gamma}$, μ, and α) this equation only has one real solution.
Let $b = -\frac{\mu\dot{\gamma}^2\beta\alpha+\alpha^2}{\beta G_0\dot{\gamma}^2}$, $c = \frac{\mu\dot{\gamma}^2\beta\alpha+2\alpha^2}{\beta G_0\dot{\gamma}^2}$, $d = \frac{-\alpha^2}{\beta G_0\dot{\gamma}^2}$, $p = c - \frac{1}{3}b^2$, and $q = d - \frac{1}{3}bc + \frac{2}{27}b^3$. Then for $p > 0$ the real solution to (4.28) can be written as (Holmes, 2002),

$$\lambda_e = -b/3 - 2\sqrt{p/3}\sinh\left(\frac{1}{3}\operatorname{arcsinh}\left(\frac{q/2}{(p/3)^{3/2}}\right)\right). \tag{4.29}$$

For an imposed strain rate, if $\lambda < \lambda_e$, then the structure parameter, λ, grows in time to reach λ_e. If on the other hand $\lambda > \lambda_e$, then the structure parameter decreases in time to reach λ_e. Figure 4.7 depicts the development of the structure parameter, λ, for various initial structures, λ_0, under a constant strain rate.

4.2.7. SOLUTIONS AT CONSTANT VALUES OF $\dot{\gamma}$ AND $|\tau : \dot{\gamma}|$

For constant values of $|\tau : \dot{\gamma}|$ in time, equation (4.9) can be solved to obtain,

$$\lambda = (\lambda_0 - \lambda_e)\, e^{-(\alpha+\beta|\tau:\dot{\gamma}|)\,t} + \lambda_e, \tag{4.30}$$

where, $\lambda_0 = \lambda(t = 0)$.
A more complex relation can be derived for the residual strain for constant values of $\dot{\gamma}$ and $|\tau : \dot{\gamma}|$,

$$\gamma_r = \frac{1}{u}\int \dot{\gamma} u \, dt + C, \tag{4.31}$$

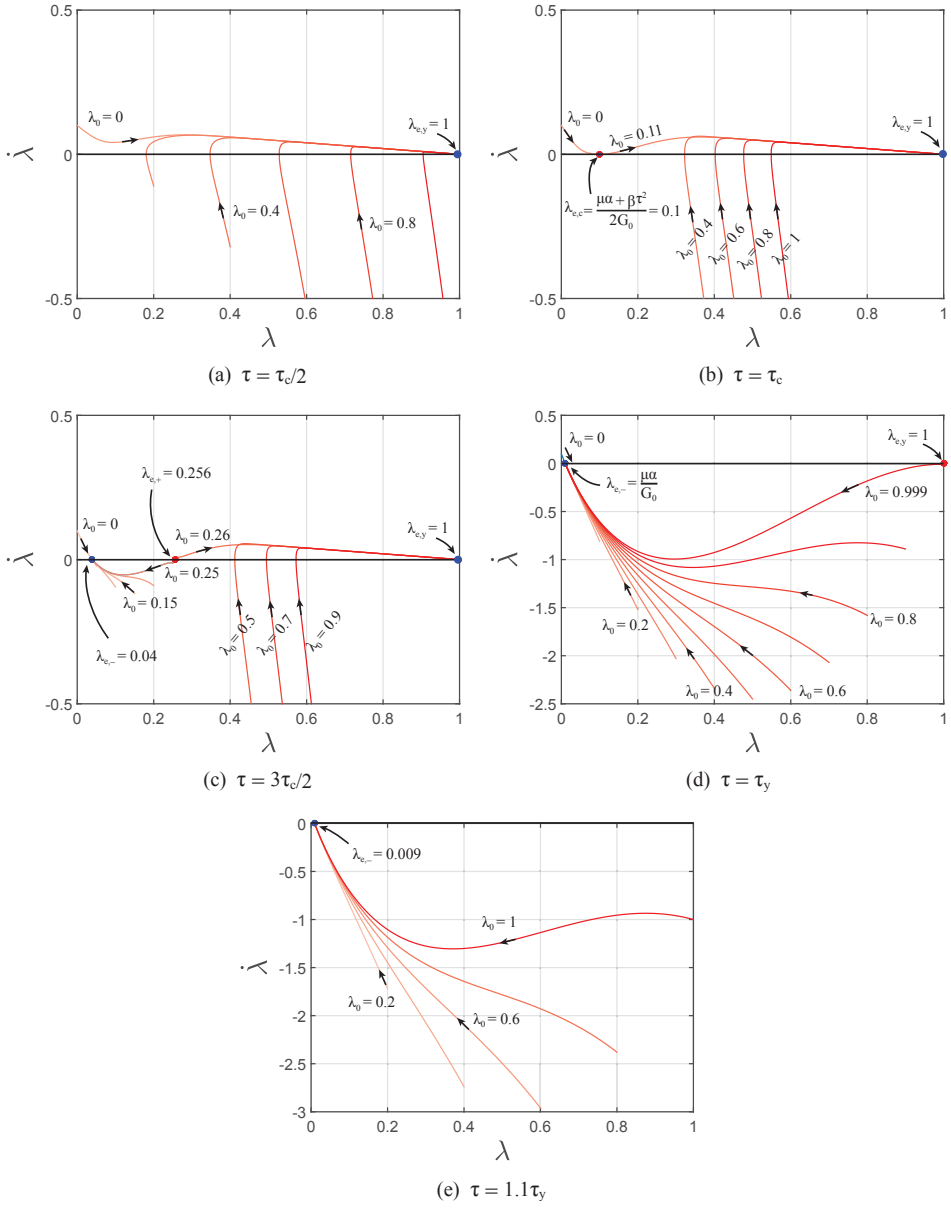

Figure 4.6: Change in the structure parameter, λ, with time, for various initial structures, λ_0, under different stress conditions.

where, C is a constant and,

$$u = \left(\frac{\lambda_0 - \lambda_e}{\lambda_e} + e^{(\alpha+\beta|\tau:\dot{\gamma}|)t} \right)^{1-\lambda_e} + \left(\frac{\lambda_0 - \lambda_e}{\lambda_e} + e^{-(\alpha+\beta|\tau:\dot{\gamma}|)t} \right)^{\lambda_e}. \tag{4.32}$$

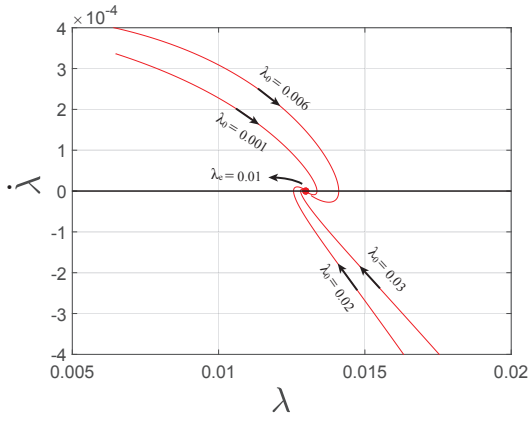

Figure 4.7: Change in the structure parameter, λ, with time, for various initial structures, λ_0, under a constant strain rate.

The complications in solving the integral in (4.31) can be avoided by introducing a new variable $\zeta = \lambda\gamma_r$. The rheological model then reads,

$$\tau = G_0\zeta + \mu\dot{\gamma}, \tag{4.33}$$
$$\dot{\lambda} = \alpha(1-\lambda) - |\tau:\dot{\gamma}|\beta\lambda, \tag{4.34}$$
$$\dot{\zeta} = \dot{\gamma}\lambda - |\tau:\dot{\gamma}|\beta\zeta. \tag{4.35}$$

For constant values of $\dot{\gamma}$ and $|\tau:\dot{\gamma}|$, equation (4.35) can be solved to obtain,

$$\zeta = \frac{\dot{\gamma}(\lambda_e-\lambda_0)}{\alpha}e^{-(\alpha+\beta|\tau:\dot{\gamma}|)t} + \lambda_e\frac{\dot{\gamma}}{\beta|\tau:\dot{\gamma}|} + \left[(\gamma_{r0}+\frac{\dot{\gamma}}{\alpha})\lambda_0 - (\frac{\dot{\gamma}}{\beta|\tau:\dot{\gamma}|}+\frac{\dot{\gamma}}{\alpha})\lambda_e\right]e^{-\beta|\tau:\dot{\gamma}|t}, \tag{4.36}$$

where, $\gamma_{r0} = \gamma_r(t=0)$.

4.2.8. TYPES OF FLOW CURVES

Let f be a map sending λ_e to its corresponding stress τ, i.e., $f(\lambda_e):\lambda_e \to \tau$, and let g be a map sending λ_e to its corresponding strain rate, $\dot{\gamma}$, i.e., $g(\lambda_e):\lambda_e \to \dot{\gamma}$. Then following the discussion in Sections 4.2.5 and 4.2.6, f is non-injective, while g is bijective.

Let us imagine a material with a complete structure, $\lambda = 1$, and increase the stress until $\tau = \tau_y$. Increasing τ beyond τ_y results in a jump in the equilibrium structure parameter from $\lambda = 1$ to $\lambda_{e,-}$. Since g is bijective, the strain rate also shows a jump at this point from $g(\lambda = 1) = \dot{\gamma}_{e,y}$ to $g(\lambda_{e,-}) = \dot{\gamma}_{e,-}$. This path is shown in Figure 4.8 by red arrows.

Now imagine a material under a high shear stress and with zero structure, $\lambda = 0$, and decrease the stress until $\tau = \tau_c$. Decreasing τ beyond τ_c results in a jump in the equilibrium structure parameter from $\lambda_{e,c}$ to $\lambda = 1$. Again, since g is bijective, the strain rate also shows a jump at this point from $g(\lambda_{e,c}) = \dot{\gamma}_c$ to $g(\lambda = 1) = \dot{\gamma}_{e,y}$. This path is shown in Figure 4.8, by black arrows.

Note that in Figure 4.8, the slope of the initial rise in the flow curve, resembling elastic solid behavior, as well as the stress at the point of yielding, are dependent on the speed at which the stress is increased. This topic will be explained more thoroughly in Section 4.2.9. Non-injectivity of f, results in a different picture for strain controlled hysteresis

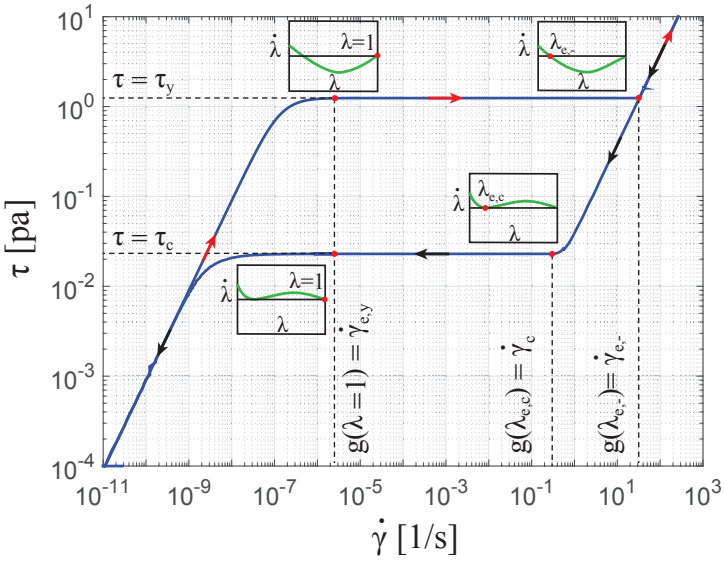

Figure 4.8: Stress controlled hysteresis plot obtained from equations (4.33)-(4.35). The red arrows show the path of increasing stress and the black arrows show the path of decreasing stress. The inset plots depict the bifurcation of the structure parameter.

plots. For $\tau_c < \tau < \tau_y$, there are three equilibrium structure parameters (non-injectivity of f) and each structure parameter corresponds to only one shear rate (bijectivity of g). Consequently, multiple strain rate values correspond to one specific stress in this regime. Figure 4.9 shows a strain controlled hysteresis plot. The red and black arrows show the path of increasing and decreasing strain rate, respectively. Note that the model has the ability to capture the critical yield stress, i.e., the minimum stress in a strain controlled flow curve. For clay-water suspensions, the falling region of the flow curve corresponds to the shear banding instability (Pignon et al., 1996). The model has an unstable equilibrium solution in this transitional region and therefore, mimics the physical behavior of the material well in this regime.

For $\tau_y = 0$ or $\dot{\gamma} \to \infty$, the model presented in (4.33) simplifies to the Newtonian fluid model, $\tau = \mu\dot{\gamma}$. Furthermore, for $\alpha \to \infty$, $\tau_c \to \tau_y$, and (4.33) resembles the Bingham elastic model (Yoshimura & Prud'homme, 1987). For all the other cases, the rheological model presented by equations (4.33)-(4.35) describes a thixotropic yield stress fluid.

4.2.9. APPARENT YIELD STRESS

In order to make a stationary material with a structure parameter, $\lambda < 1$, flow, one has to overcome the apparent yield stress that corresponds to $\lambda_{e,+}$ (Figure 4.6), i.e.,

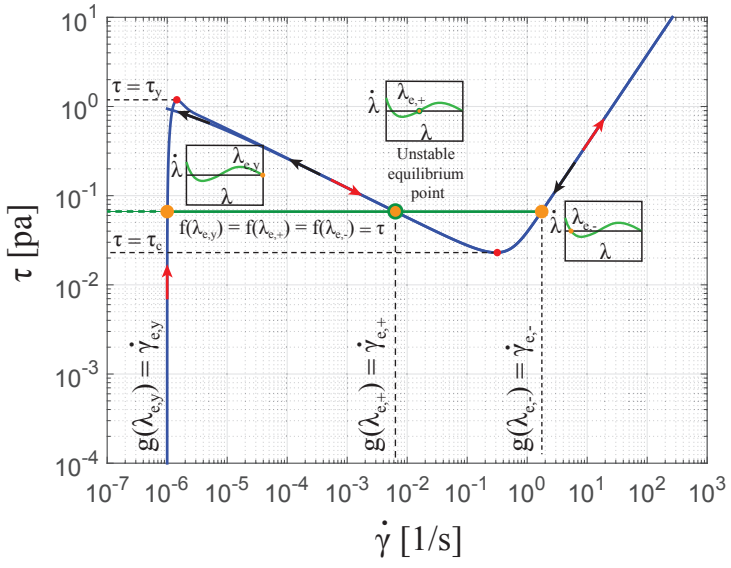

Figure 4.9: Strain controlled hysteresis plot obtained from equations (4.33)-(4.35). The red arrows show the path of increasing strain rate and the black arrows show the path of decreasing strain rate. The inset plots depict the bifurcation of the structure parameter.

$$|\tau_{y,+}| = \sqrt{\frac{G_0\lambda_{e,+}^2 + \mu\alpha\left(1-\lambda_{e,+}\right)}{\beta\lambda_{e,+}}}. \tag{4.37}$$

In general, the structure state of a stationary material at a given time is $\lambda_{e,+}$. Therefore, in order to break this structure, a stress level higher than $|\tau_{y,+}|$, where, $\tau_c < \tau_{y,+} < \tau_y$, should be imposed on the material. For $\lambda_{e,+} = 1$, $\tau_{y,+} = \tau_y$, and for $\lambda_{e,+} = \lambda_{e,c}$, $\tau_{y,+} = \tau_c$ (Figure 4.6). Once $\tau_y < \tau$, there are no longer any unstable equilibrium structure points, $\lambda_{e,+}$, and consequently, there are no apparent yield stresses.
In stress versus strain rate plots, the apparent yield stress is the stress at which the jump in strain rate occurs. To analyze such a case, let $\tau = \tau(t)$, be a logarithmic staircase function with a constant step duration, Δt, (inset plot of Figure 4.10(a)). During each step duration, Δt, equations (4.33)-(4.35) are then solved for each constant stress. Figure 4.10(a) shows the stress versus the strain rate value that is obtained at the end of each time step. Figure 4.10(b) shows the stress versus the structure parameter in blue and the apparent yield stress, $\tau_{y,+}$, versus $\lambda_{e,+}$ in red, all computed at the end of each time step. The point where the blue and the red curves cross corresponds to the structure state at which $\tau_{y,+} < \tau$, and the material first begins to flow, i.e., $\lambda \to \lambda_{e,-}$ (Figure 4.6).
Since from the apparent/transient stress versus strain rate plots (experimental or in this case numerical), one can only obtain the apparent yield stress, $\tau_{y,+}$, reverse engineering must be done to obtain the value of τ_y.

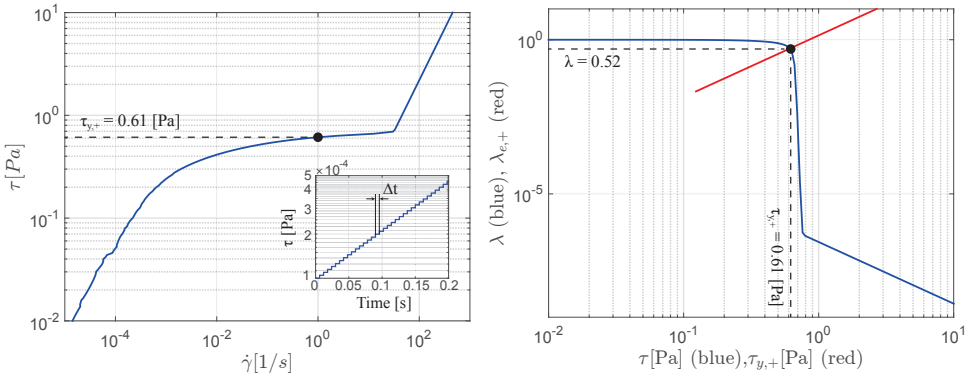

(a) Stress versus strain rate plot.

(b) Structure parameter versus stress.

Figure 4.10: Transient stress versus strain rate plot (a), and structure parameter versus stress curve (b), obtained at the end of each time interval Δt, for a logarithmic staircase input function shown in the inset plot of (a). The red and blue curves in (b) show the change in $\lambda_{e,+}$ with the apparent yield stress $\tau_{y,+}$, and the structure parameter, λ, with stress, τ, respectively.

4.2.10. RELATION TO OTHER MODELS

The rheological model presented in this study is analogous to those from the studies of Mujumdar et al. (2002) and Dullaert & Mewis (2006). The fundamental difference between these models is with regards to their formulations of the elastic strain and the structure parameter. Although a complete evaluation of the dis/similarities between these models is outside the scope of the current work, in this section some of these points are briefly discussed. Table 4.1 lists the three rheological models.

Authors	Const. model	Structure model	Elastic strain model	Emp. parameters
Mujumdar et al.	$\tau = \lambda G\gamma_e + (1-\lambda)K\dot{\gamma}^n$	$\dot{\lambda} = k_1\dot{\gamma}_+\lambda + k_2(1-\lambda),\ \dot{\gamma}_+ = \begin{cases} 0 : \dot{\gamma}\gamma_e \le 0, \\ \lvert\dot{\gamma}\rvert : \dot{\gamma}\gamma_e > 0. \end{cases}$	$\begin{cases} \dot{\gamma}_e = \dot{\gamma} : \lvert\gamma_e\rvert < \gamma_{co}\lambda^m, \\ \gamma_e = \gamma_{co}\lambda^m : \lvert\gamma_e\rvert > \gamma_{co}\lambda^m. \end{cases}$	G, n, K, k_1, k_2, γ_{co}, m
Dullaert and Mewis	$\tau = \lambda G_0\gamma_e + \lambda\eta_{st,0}\dot{\gamma} + \eta_\infty\dot{\gamma}$	$\dot{\lambda} = (1/t^\beta)\left(-k_1\dot{\gamma}\lambda + k_2\dot{\gamma}^{0.5}(1-\lambda) + k_3(1-\lambda)\right)$	$\dot{\gamma}_e = (1/t)^\beta\left(\tau\gamma_c - \tau_{ss}\gamma_e\right)$	γ_c, G_0, $\eta_{st,0}$, η_∞, β, k_1, k_2, k_3
This Study	$\tau = \lambda G_0\gamma_r + \mu\dot{\gamma}$	$\dot{\lambda} = -\beta\lvert\tau : \dot{\gamma}\rvert\lambda + \alpha(1-\lambda)$	$\dot{\gamma}_r = \dot{\gamma} - \frac{\gamma_r\alpha(1-\lambda)}{\lambda}$	μ, G_0, α, β

Table 4.1: The structural kinetic models of Mujumdar et al. (2002), Dullaert & Mewis (2006), and this study.

COMPARISON TO THE MODEL OF MUJUMDAR ET AL. (2002)

Mujumdar et al. (2002) present a model based on the network association theory where the material is viewed as a network of small indivisible particles. Once shear is applied to the material, the network breaks down into flocs. If breakdown is continued, the flocs eventually decompose into individual particles. In their formulation, the time-dependent elastic limit of the material is related to the size of the flocs via the structure parameter and an exponent, m, that characterizes the elastic limit of the flocs.

It is difficult to express the phenomenology that is explained by Mujumdar et al. (2002) (regarding the breakdown of the network into flocs and ultimately into particles) with a picture, such as the one shown in Figure 4.4. Similar to the model of Mujumdar et al. (2002), the model that is presented in the current study is based on the network theory. However, unlike their model, here it is assume that the behavior of the material is uniform and scale invariant. This precludes the need for an exponent such as m.
A key feature of the model of Mujumdar et al. is a smooth transition from an elastically dominated response to a viscous response, with no jump discontinuity in the stress-strain curve (Figure 4.11(b)). Nonetheless, the formulation of both the structure parameter and the elastic strain are discontinuous in their work, which makes numerical computation cumbersome (Table 4.1).
Analogous to the model of Mujumdar et al. (2002), the model presented here allows for a smooth transition from an elastically dominated response to a viscous response, with no jump discontinuity in the stress-strain curve (Figure 4.11(a)). However, in contrast to their model, the formulations of both the structure parameter and the elastic strain, are continuous in the model presented here.

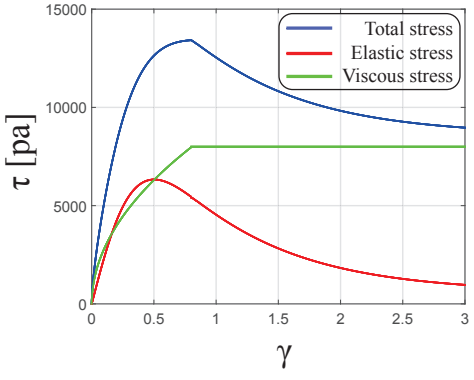

(a) Elastic and viscous contribution to the total stress according to the model from this study.

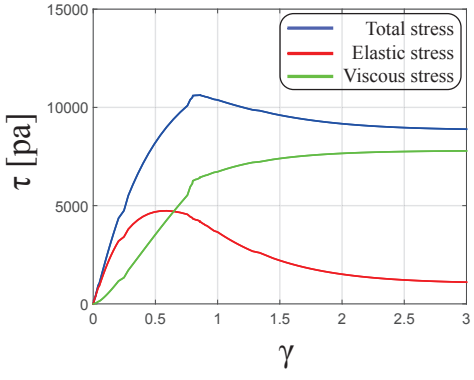

(b) Elastic and viscous contribution to the total stress according to the model of Mujumdar et al.

Figure 4.11: Prediction of the elastic, viscous, and total stress response from the model presented in the current study (a), and from the model presented by Mujumdar et al. (2002) (b), during the start-up of a steady shear flow, $\dot{\gamma} = 20\ s^{-1}$. The parameters used in the model from this study are: $G_0 = 25000\ Pa$, $\alpha = 1\ s^{-1}$, $\mu = 400\ Pa \cdot s$, $\beta = 0.00016\ Pa^{-1}$. The parameters used in the model of Mujumdar et al. are: $G = 25000\ Pa$, $K = 400\ Pa \cdot s$, $k_1 = 2$, $k_2 = 1\ s^{-1}$, $\gamma_{co} = 0.5$, $n = 1$, $m = -0.33$.

Following the same procedure as in Section 4.2.5, the evolution of the structure parameter under various stress conditions can be evaluated for the model of Mujumdar et al. To allow comparison with the current study, let the parameter $n = 1$ (no shear thinning) in Table 4.1. Then, in equilibrium, the following expression can be derived for the structure parameter,

$$k_1 G \gamma_{co} \lambda_e^{m+1} + K k_2 \lambda_e^2 - 2K k_2 \lambda_e + K k_2 - k_1 \tau = 0. \tag{4.38}$$

It can be seen that depending on the value of the exponent, m, equation (4.38) can have different numbers of roots. For instance for $m = -0.3$ (a representative case from their

study), this equation has in total 20 roots, repeated, as well as distinct (this can be shown by a change of variable from λ_e to Q, where $Q^{10} = \lambda_e$). This suggests that the model of Mujumdar et al. may be difficult to interpret with regards to the phenomenon of viscosity bifurcation.

Figure 4.12 shows the strain controlled flow curves obtained from the model of Mujumdar et al. (blue), and from the current study (red). It can be seen that qualitatively, the two models result in very similar flow curves. Nonetheless, there are small discrepancies that make the differences between the two models more conspicuous. A C^1 discontinuity can be observed within the non-linear elastic regime of the blue curve. This is not the case for the flow curve obtained from the current study. Furthermore, the two models show slightly different behaviors at the end of the liquefaction and the beginning of the viscous regimes.

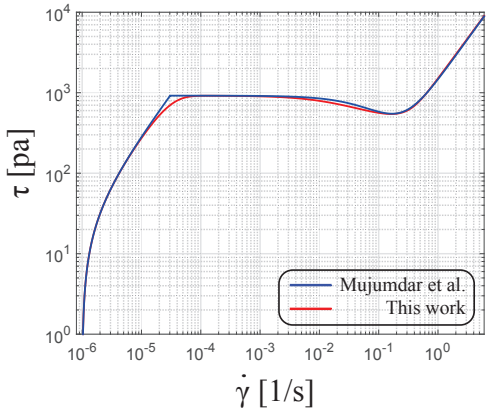

Figure 4.12: Strain controlled flow curves obtained from the model of Mujumdar et al. (2002) (blue), and from the current study (red). The parameters used to obtain the blue curve are: $G = 40000\ Pa$, $K = 1500 Pa \cdot s$, $k_1 = 10$, $k_2 = 1\ s^{-1}$, $\gamma_{co} = 0.023$, $n = 1$, $m = 0.15$. The parameters used to obtain the red curve are: $G_0 = 40000 Pa$, $\alpha = 1\ s^{-1}$, $\mu = 1500\ Pa \cdot s$, $\beta = 0.04\ Pa^{-1}$.

Finally, the model presented by Mujumdar et al. contains six empirical parameters (not including n). In contrast, the model presented in this study has four parameters.

COMPARISON TO THE MODEL OF DULLAERT & MEWIS (2006)

Dullaert & Mewis (2006) present a general structural kinetic model to describe the flow behavior of thixotropic systems. Analogous to the current study, in their work the total stress is divided into a structure-dependent elastic and a viscous contribution.

To describe the elastic contribution, Dullaert and Mewis propose a single stress-dependent kinetic equation that allows the aggregates to relax after a reduction in hydrodynamic stress and stretch when the stress is increased. This is in contrast to the approach taken in the current study where, the kinetic equation for the elastic strain of the flowing structure is derived from the first principles using the structure model, and based on a set of physical assumptions regarding particle interactions at the micro-scale. Dullaert and Mewis state that their model can predict overshoot stresses that are larger than the apparent yield stress during start up flows. The model presented herein however, does not predict such overshoot stresses. According to the model in the current

study, as soon as shear is applied to the material, the structure begins to break down. Depending on the strain rate, the structure can break down faster (higher strain rates), or slower (lower strain rates), which in turn can cause the material to reach its yield point quickly, or slowly. The stress at the point of yielding is here referred to as the apparent yield stress and is always smaller than the true yield stress of the material. During start up flows, the stress can quickly reach the apparent yield stress (stress over-shoot) and subsequently drop to the stress of the flowing material (Section 4.4.2). However, it can never exceed the apparent yield stress of the material.

According to Dullaert and Mewis, upon cessation of flow, their model can predict non-zero values for the stress. The model presented in this study also has this attribute (Section 4.4.1). The structure model employed by Dullaert and Mewis is not symmetric with respect to the stress and the strain rate. The structure model used in this study however, is symmetric.

Following the same procedure as in Section 4.2.5, the evolution of the structure parameter under various stress conditions can be evaluated for the model of Dullaert and Mewis. This results in the following expression for the structure parameter in equilibrium,

$$-k_1\left(\frac{\tau - G_0\lambda_e\gamma_c}{\eta_{st,0}\lambda_e + \eta}\right)\lambda_e + k_2\left(\frac{\tau - G_0\lambda_e\gamma_c}{\eta_{st,0}\lambda_e + \eta}\right)^{1/2}(1-\lambda_e) + k_3(1-\lambda_e) = 0. \tag{4.39}$$

The roots of this expression are difficult to obtain. This suggests that the model of Dullaert and Mewis may be difficult to interpret with regards to the phenomenon of viscosity bifurcation.

Figure 4.13 shows the strain controlled flow curves obtained from the model of Dullaert and Mewis (blue), and from the current study (red). It can be seen that qualitatively, the two models result in quite different flow curves. The red curve is non-monotonic and has a minimum. While the blue curve is a monotonically increasing flow curve. The two curves predict very different material behaviors within the non-linear elastic and the liquefaction regimes. However, some of these differences may be attributed to the values of the empirical parameters used here.

Finally, the model presented by Dullaert and Mewis contains eight empirical parameters. In contrast, the model presented in this study has four parameters.

4.3. METHODOLOGY FOR OBTAINING THE EMPIRICAL PARAMETERS AND THE RHEOMETRIC VALIDATION TESTS

In this section the methodology behind the stress and the strain controlled measurements which, (1) can be used to obtain the empirical parameters, μ, G_0, τ_y, and α (note that $\beta = G_0/\tau_y^2$), and (2) are used to evaluate the performance of the model, are explained.

The stress controlled shearing conditions within the boundary layer of sediment gravity flows are simulated using stress controlled stress versus strain rate curves. The stress controlled shearing conditions within the boundary layer eddies are simulated using oscillatory stress controlled amplitude sweep tests. The strain controlled shearing conditions within the free shear and boundary layers are simulated using strain controlled stress versus strain rate curves. For the computations, equations (4.33)-(4.35) are

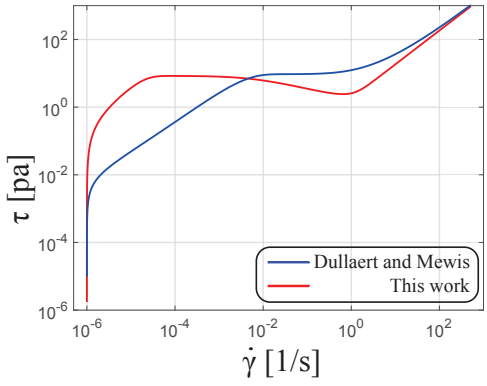

Figure 4.13: Strain controlled flow curves obtained from the model of Dullaert & Mewis (2006) (blue), and from the current study (red). The parameters used to obtain the blue curve are: $\gamma_c = 0.015$, $G_0 = 560\ Pa$, $\eta_{st,0} = 8.6\ Pa \cdot s$, $\eta_\infty = 1.84\ Pa \cdot s$, $\beta = 0.37$, $k_1/k_3 = 0.99\ s$, $k_2/k_3 = 0.42\ s^{0.5}$, $k_3 = 0.20\ s^{\beta-1}$. The parameters used to obtain the red curve are: $G_0 = 560\ Pa$, $\alpha = 0.55\ s^{-1}$, $\mu = 1.84\ Pa \cdot s$, $\beta = 7.9\ Pa^{-1}$.

solved numerically using a variable order backward differentiation formula (Shampine & Reichelt, 1997). A fast numerical approach for solving these equations in MATLAB is given in Appendix B.

4.3.1. MIXTURE PREPARATION AND MEASUREMENT CONSIDERATIONS AND APPARATUS

Mixture of quartz sand from Sibelco with median diameter of 150 μm and Crown Kaolinite clay from ActiveMinerals International, with median diameter of 0.18 μm were prepared. The sediment volume concentration was varied between 9%, 12.65%, 15%, 17.82%, and 21% and contained 2/3 sand and 1/3 clay. For the dilute case of 9% sediment concentration, the suspension is close to the gelling concentration and the low stress measurements may be influenced by artifacts such as surface tension or the shape of the sample periphery. Therefore, the data for this case is not included during apparent yield stress or shear modulus fitting (Figure 4.15).

MRC302 Anton Paar rheometer was used for all the measurements. To reduce the effect of settling on the measurements, a concentric cylinder geometry was used. The inner cylinder diameter was 28.92 mm. In order to avoid wall slip a sandblasted bob with a diameter of 26.663 mm and a surface roughness of 4-7 μm was used. The mixtures were introduced inside the cylinder with a syringe. A cover was used during the tests to reduce water evaporation. The measurements were performed at a temperature of 20°C.

4.3.2. OSCILLATORY STRESS CONTROLLED AMPLITUDE SWEEP TESTS AND SHEAR MODULUS, G_0, MEASUREMENTS

For low values of strain, $\lambda \approx 1 \Rightarrow N \approx N_0$, and $G' \approx G_0$. Therefore, the value of G_0 can be approximated by the value of the storage modulus, G', obtained from amplitude sweep tests at low values of strain.

Prior to the measurements, the samples were left at rest for a period of 3000 s in order to regain structure. Subsequently, stress controlled amplitude sweep tests were performed on the samples. The stress amplitude was increased from 0.0001 Pa to various final values depending on the sediment concentration, and the angular frequency was set to 10 rad/s.

Figure 4.14 depicts the storage, G', and loss, G'', moduli as a function of strain for a representative sample with 12.65% sediment concentration. The dashed line represents the value of G_0 approximated by the value of G' from the linear part of stress controlled amplitude sweep plots. Similar plots were obtained for other sediment concentrations.

Figure 4.15(a) depicts the shear modulus, G_0, obtained for various sediment concentration after a rest period of 3000 s. The dashed line in Figure 4.15(a) was obtained by fitting a power law function to the measurement data. The data for the 9% sediment concentration was not considered during fitting (section 4.3.1). The resulting R^2 goodness of fit value of this power law function is 0.99.

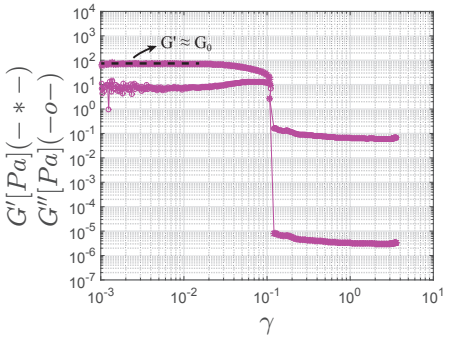

Figure 4.14: Storage and loss moduli versus strain obtained from a stress controlled amplitude sweep test for a sample with 12.65% sediment concentration, after a resting period of 3000 s. The dashed line represents the approximated value of elastic modulus, G_0.

4.3.3. YIELD STRESS, τ_y, AND VISCOSITY, μ, MEASUREMENTS

The yield stress and the viscosity values of the mixtures can be obtained from stress controlled rheometry tests. Prior to the measurements, the mixtures were poured into the cylinder geometry and were left to rest for 3000 s in order to regain structure. Stress was then increased from 0.0001 Pa to 1.6, 8, 11, 20, and 25 Pa for 9%, 12.65%, 15%, 17.82%, and 21% sediment concentrations, respectively. The duration for obtaining a data point was set to 2 s.

Figure 4.16 depicts the measurement result of a representative sample with 12.65% concentration for $0.01 < \dot{\gamma}$. The value of the apparent yield stress, $\tau_{y,+}$, and viscosity, μ, were obtained from the plots (Figure 4.16). Equations (4.33)-(4.35) were then solved for the same input stress parameters as for the measurements. Assuming 3000 s was enough time to reach complete structure ($\lambda = 1$), the initial conditions were set to $\lambda_0 = 1$ and $\gamma_{r0} = 0$. The value of τ_y for each concentration was then adjusted such that the value of $\tau_{y,+}$ obtained from the model matched its value from the measurements.

Figure 4.15 shows the values of the viscosity and the apparent yield stress for different sediment concentrations. Curve fitting was then performed on the results. The apparent yield stress data for the 9% sediment concentration was not considered during fitting (section 4.3.1). For the viscosity and the apparent yield stress, power law functions resulted in fits with $R^2 = 0.99$. The value of β was then calculated from the model (τ_y) and the data (G_0) using the relation $\beta = G_0/\tau_y^2$.

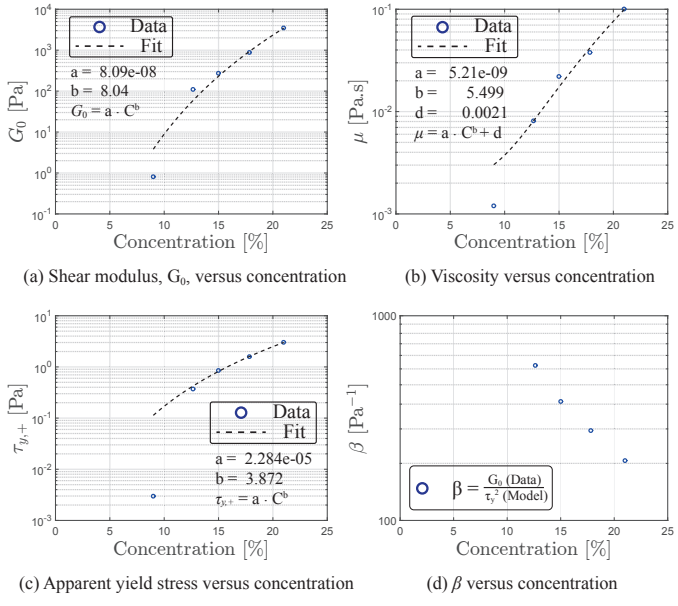

(a) Shear modulus, G_0, versus concentration

(b) Viscosity versus concentration

(c) Apparent yield stress versus concentration

(d) β versus concentration

Figure 4.15: Shear modulus, G_0, viscosity, μ, apparent yield stress $\tau_{y,+}$, and β versus sediment volume concentration. The dashed lines are obtained from curve fitting. For the shear modulus, the viscosity, and the apparent yield stress, power law functions resulted in fits with $R^2 = 0.99$. The apparent yield stress and shear modulus data obtained from samples with 9% concentration were not considered during fitting.

4.3.4. STRUCTURE BUILD UP RATE, α

From equation (4.34), for low values of, $|\tau : \dot{\gamma}|$, one has,

$$\dot{\lambda} \approx \alpha(1-\lambda). \tag{4.40}$$

Therefore, in order to obtain the structure build up rate, α, the value of $|\tau : \dot{\gamma}|$ should be kept small. Furthermore, the imposed stress amplitude must be set such that it is smaller than the critical stress, τ_c.

Immediately after the introduction of the mixture into the cylinder, stress controlled oscillatory tests were performed and the change of storage modulus was monitored in time. The amplitude of the sinusoidal stress input was set to 0.002 Pa and the angular frequency was set to 0.5 rad/s. Figure 4.17 shows the change of the storage modulus in time obtained from the measurements for samples with 12.65% and 15% concentrations.

To quantify the structure build up rate, α, equations (4.33)-(4.35) were solved. For the

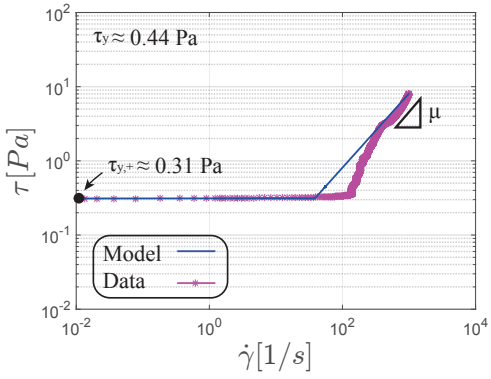

Figure 4.16: Stress versus strain rate curve obtained from stress controlled measurements after a resting period of 3000 *s* for a representative sample with 12.65% concentration. The solid blue line is computed using equations (4.33)-(4.35).

computations the same input parameters as the rheometry tests were used. The results were then fitted to the measurement data. The blue dashed lines in Figure 4.17 depict the results of this procedure. The values of α obtained from this procedure for the samples with 17.82% and 21% concentrations were 0.00025 and 0.00015, respectively.

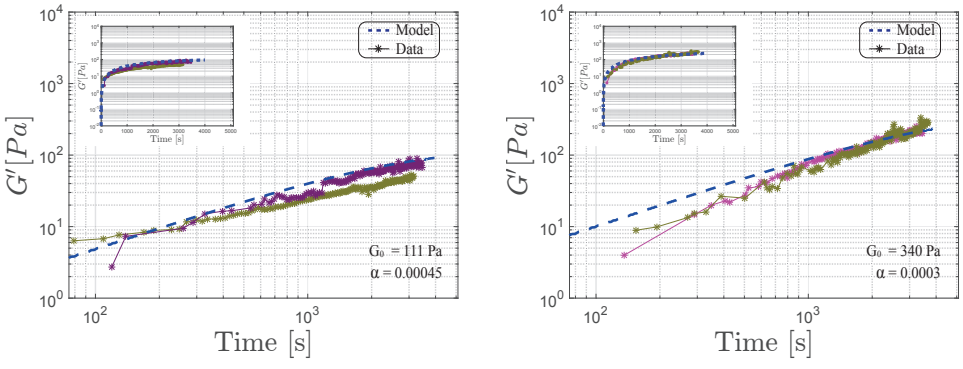

(a) 12.65% concentration

(b) 15% concentration

Figure 4.17: Modeled (blue dashed lines) and measured (purple and green lines) storage modulus, G', depicting structure build up in time for (a) 12.65%, and (b) 15% concentrations.

4.3.5. STRESS CONTROLLED MEASUREMENTS

A set of measurements were performed on a sample with 15% sediment concentration. In order to enhance the reproducibility of the results, before the measurements, the sample was pre-sheared. This was done by increasing the stress from 0.004 *Pa* to 10 *Pa*, immediately after the introduction of the sample within the cylinder geometry. The duration of this phase was 510 *s*. Next the mixture was left to rest for a period of 9000 *s* to regain structure. Subsequently, the stress was increased ramp logarithmically from

0.004 Pa to 10 Pa. Each data point was obtained by the rheometer once the shear rate reached a steady state. The mixture was then left to rest for a period of 9000 s to regain structure. Finally, a stress controlled oscillatory test was performed on the mixture. The angular frequency was set to 0.5 rad/s and the stress amplitude was increased ramp logarithmically from 0.004 Pa to 10 Pa.
For the numerical simulations, the same input conditions as for the measurements were used. For the oscillatory amplitude sweep computations, in order to suppress the noise within the numerical results, a lowpass filter was used in regions before the yielding occurred, and subsequent to the yielding, average values of the storage and loss moduli were considered.

4.3.6. STRAIN CONTROLLED MEASUREMENTS

Strain controlled measurements were performed on a sample with 15% sediment concentration. Prior to the measurements, the sample was left at rest for a period of 3000 s in order to regain structure. Subsequently, the strain rate was increased ramp logarithmically from $10^{-6}s^{-1}$ to $500s^{-1}$. The duration for obtaining a data point was set to 2 s. The number of measurement points was set to 7830. Data reproducibility was considered acceptable to not include a pre-shear period. For the numerical simulations, the same input conditions as for the measurements were used.

4.4. RESULTS AND DISCUSSION

In this section first the solutions of equations (4.33)-(4.35) for some selected flows is presented. Subsequently, the ability of the model to reproduce the results obtained from the stress and the strain controlled measurements, discussed in Sections 4.3.5 and 4.3.6, is evaluated.

4.4.1. DEFORMATION UNDER CONSTANT STRESS

We would like to investigate the predictions of the model at the solid-liquid transition. To do this we look at, (1) creep tests performed with different stress levels on a completely structured material $\lambda = 1$, and (2) creep tests performed with a specific stress level on a material with different initial structure states.
Figure 4.18(a) depicts material deformation as a function of time for a completely structured material, $\lambda_0 = 1$, under different stress levels, τ, where $\tau(t) = \tau H(t)$, and $H(t)$ is the Heaviside unit step function. As it is commonplace for pasty materials (Coussot et al., 2006), two regimes can be observed. For stresses smaller than $\tau_{y,+}$, the model predicts an initial rapidly rising phase in the deformation, followed by a leveling off and reaching a plateau phase. For stresses higher than $\tau_{y,+}$, the model predicts a straight line of slope 1 in the logarithmic scale, i.e., the deformation tends to increase at a constant rate. It can be seen that the transition between the two regimes is abrupt in terms of shear rate, i.e., for a small increase in stress beyond $\tau_{y,+}$, the slope of $\gamma(t)$ changes abruptly from zero to 1. As it was explained in Section 4.2.9, the value of $\tau_{y,+}$ is a function of how fast the stress ramp is reached and is smaller than τ_y (in this case $\tau_{y,+} = 0.5\tau_y$).
Figure 4.18(b) shows the material deformation as a function of time after application of

a stress ramp to a material with various initial structure parameters. It can be seen that for an initial structure parameter higher than approximately 0.4, the material shows an elastic solid behavior. For lower initial structure parameters however, the behavior of the material abruptly transforms to that of a viscous liquid. Once stress is applied to a ma-

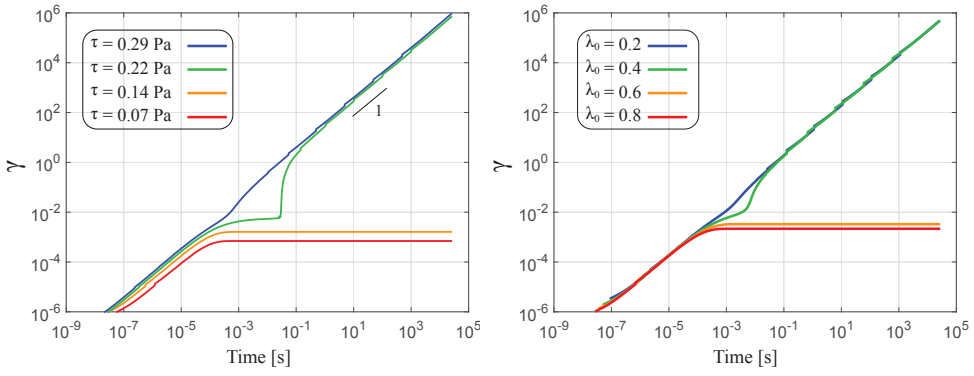

(a) Creep tests under different stresses ($\lambda_0 = 1$).

(b) Creep tests for different initial structure parameters ($\tau = 0.14$ Pa).

Figure 4.18: Creep test plots obtained from equations (4.33)-(4.35) for (a) a completely structured material, $\lambda_0 = 1$, under various stress levels, and (b) for various initial structure states and under a constant stress level, $\tau = 0.14\ Pa$. The value of the yield stress, τ_y, was set to 0.37 Pa.

terial, its structure is damaged and begins to undergo a recovery process known as aging (Coussot et al., 2006). For very short creep test durations, t_w, the deformation undergone by the material during the test is almost completely recovered for sufficiently long relaxation times. For longer creep tests on the other hand, the model predicts a drop in $\gamma(t)$ to a remaining value, γ_i. Figure 4.19 shows the deformation response of a material, as predicted by the model, to creep tests with different test durations, t_w. It can be seen that for longer t_w, the value of the remaining strain is higher. Once the structure is completely recovered, γ_i converges to a fixed value.
All these trends have been discussed by Coussot et al. (2006) for various pasty materials.

4.4.2. DEFORMATION UNDER CONSTANT STRAIN RATE

Let $\dot{\gamma}(t) = \dot{\gamma}(H(t-t_0) - H(t-t_1) + H(t-t_2))$, where t_0 and t_2 correspond to the times at which a strain rate of magnitude $\dot{\gamma}$ is applied to a completely structured material, and t_1 corresponds to the cessation of application of strain rate. The stress response of a material to such an input is depicted in Figure 4.20. For small strain rate inputs (Figure 4.20(a)), the elastic stress is dominant, i.e., $\tau \approx G_0\zeta$. In this regime no prominent local maximum can be observed in the stress response at $t = t_0$ (at which point the strain rate $\dot{\gamma}$ is initially applied). Instead, the stress increases until it reaches a steady value. Once the strain rate is set to zero at $t = t_1$, the stress response shows no change. This indicates that for $t_0 < t < t_1$, the material undergoes a deformation in this regime that is not recovered once the shear rate is set to zero, i.e., as $\lambda \to 1$ for long relaxation times, γ_r approaches a constant value. At $t = t_2$, again a strain rate of magnitude $\dot{\gamma}$ is applied to the material. The

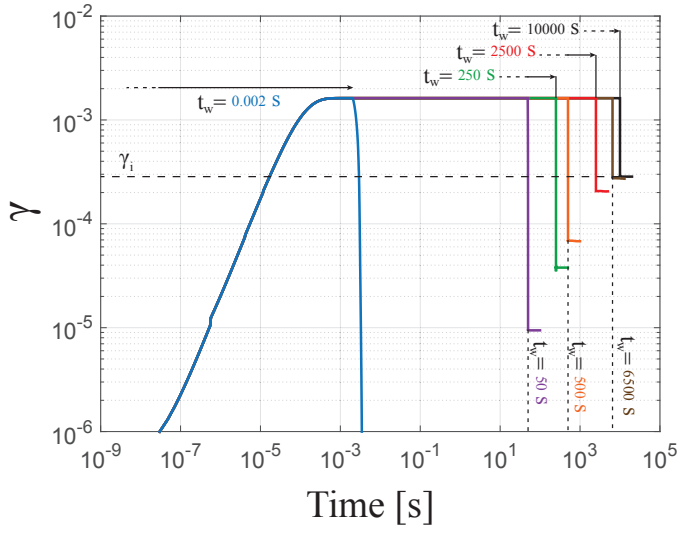

Figure 4.19: The deformation response of a material obtained from equations (4.33)-(4.35) to creep tests with different durations, t_w. The horizontal dashed line depicts the remaining strain, γ_i, after complete recovery of the material.

stress response shows an initial increase at $t = t_2$ to a maximum, drops to a minimum, and increases and reaches the same steady value as it had reached just before $t = t_1$. This is because the high shear rate after the jump results in a sudden increase in the stress, which then breaks the structure. Since the structure is lost, the stress begins to drop to a minimum (inset plot in Figure 4.20(a)). At this stage the material begins to recover its structure, and the stress begins to increase and reach a steady state value. The time it takes the material to reach the steady state after $t = t_2$ is shorter than the time it took it initially to recover after $t = t_0$. This is due to the fact that at $t = t_2$, $\gamma_r(t_2) > \gamma_r(t_0) = 0$. Therefore, it takes a shorter time for γ_r to reach the steady value, because it is closer to it. The same behavior can be observed in Figure 4.20(b), with the difference that now at $t = t_0$, stress responses show clear local maximums which are larger than the ones at $t = t_2$. This signifies that in this regime the applied strain rate is high enough to elicit an elastic response from the material that diffuses for long enough times. The red line in Figure 4.20(c) marks the initiation of a regime where viscous stresses first become comparable in magnitude to elastic stresses. Both the red and the yellow lines in this figure show a jump at $t = t_1$. This is because once the strain rate is set to zero at $t = t_1$, the portion of the stress response corresponding to viscous stress vanishes, i.e., $\mu\dot{\gamma} = 0$, and only the elastic part remains. As viscous stresses become the dominant form of stress at high shear rates the jumps in the stress response at $t = t_1$ become more severe (Figure 4.20(d)). Another interesting feature that can be observed from Figure 4.20 is that for lower strain rates, the time required to reach a steady state increases dramatically (de Souza Mendes, 2009).

These trends are corroborated by data for various thixotropic materials in the literature (Derec et al., 2003; Dullaert & Mewis, 2006).

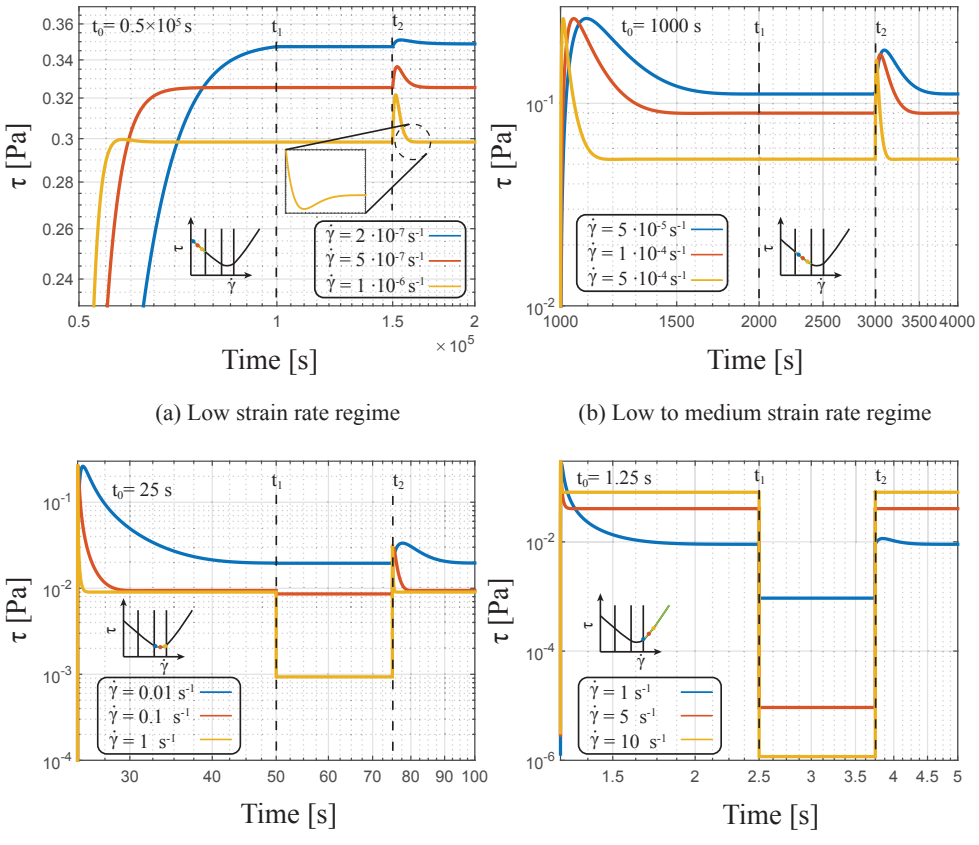

(a) Low strain rate regime

(b) Low to medium strain rate regime

(c) Medium to high strain rate regime

(d) High strain rate regime

Figure 4.20: The stress response of a material to the strain rate input $\dot{\gamma}(t) = \dot{\gamma}(H(t-t_0) - H(t-t_1) + H(t-t_2))$. Since the steady state was achieved faster at higher shear rates, the duration of the input signal (i.e. $t_2 - t_0$) was varied for the sake of improved visibility. The inset plot shows a schematic strain controlled flow curve and where the constant strain rate lines may fall on such a plot.

4.4.3. STRESS CONTROLLED MEASUREMENTS

Figure 4.21 shows the results of the stress controlled measurements that were described in Section 4.3.5.

Figure 4.21(a) presents the stress versus strain rate curves that were obtained from the model (blue line) and the measurements (red circles). The values of the empirical parameters used to solve the equations (4.33)-(4.35) are presented in this figure. The inset plot depicts the stress input, corresponding to $\dot{\gamma} > 10^{-4}\ s^{-1}$, that was imposed during the measurements and used during the simulation. It can be seen that the model shows a good agreement with the data within the liquefaction and the fluid regimes.

Figure 4.21(b) shows the stress as a function of strain. At very low values of strain, i.e., $\gamma < 10^{-4}$, the model shows small deviations from the measurements. These deviations did not have the same shape for all the sample measurements and sometime were not present. Due to the complexity of the mixture under investigation, more examination is

required to exactly pinpoint the source of this discrepancy. Nonetheless, at low values of strain, i.e., within the linear elastic regime, a relatively good agreement between the data and the model can be observed. At the end of the linear elastic regime and within the non-linear elastic regime, the model again shows some deviations from the data. As before, these deviations were not observed for all the sample measurements and their source may be traced back to the small amounts of slip that may have occurred during the measurement before yielding. The model shows good agreement with the data within the liquefaction and the fluid regimes. Figure 4.21(c) shows the measured and the

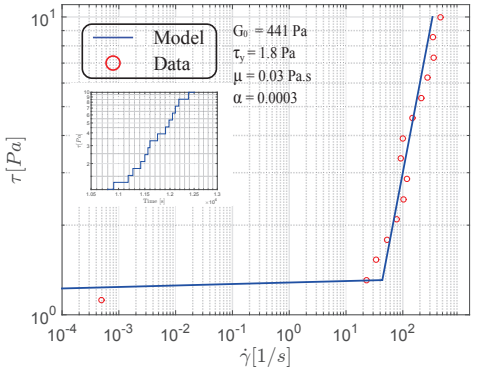

(a) Stress versus strain rate curve

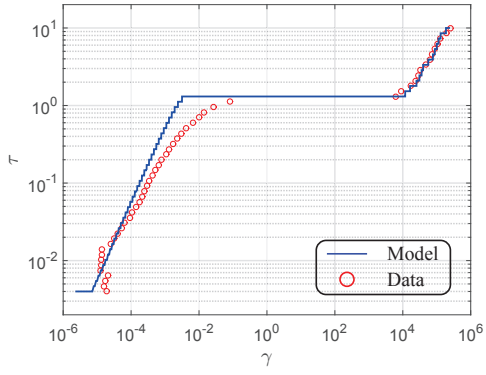

(b) Stress versus strain curve

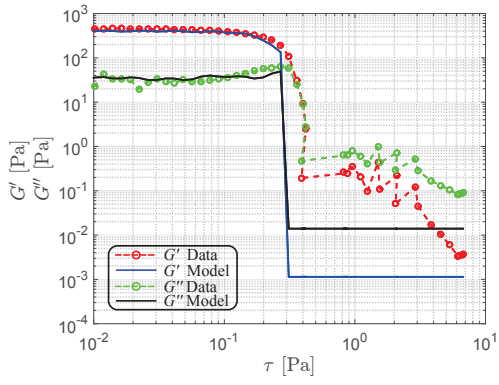

(c) Storage and loss moduli versus stress

Figure 4.21: Measured (red and green circles) and computed (solid blue and black lines) stress versus strain rate curves (a), stress versus strain curves (b), and storage and loss moduli versus stress curves (c), obtained from stress controlled measurements for 15% concentration.

computed values of the storage, G', and the loss, G'', moduli as a function of stress amplitude. A good agreement can be observed between the measured and the computed values of the storage and loss moduli within the linear and the nonlinear elastic regimes. At high stress amplitudes however, the data shows a complex behavior. The model does not capture this behavior and underestimates the average values of the storage and loss

moduli within this region. This may be due to the long duration of these tests which may have resulted in water evaporation, and in turn, increased viscosity of the mixture.

4.4.4. TRANSIENT STRAIN CONTROLLED STRESS VERSUS STRAIN RATE CURVE

Figure 4.22 shows the measured (blue stars) and the computed (solid red line) strain controlled shear stress versus strain rate curves for a sample with 15% concentration. The inset plot depicts a zoomed in view of the flow instability that is associated with the shear banding phenomenon. As discussed by Pignon et al. (1996), the shear rate values provided by the rheometer in this region correspond to a very localized or transient flow and are smaller than the actual shear rate values. Therefore, although with the corrected shear rate values, the qualitative shape of the transient curve would remain the same, the data in this part of the curve should be precluded from comparison with the model. It can be seen that the measurements and the model both show an initial rise in the shear stress until a maximum yield point followed by a drop to a minimum. The measurements suggest that at an approximate strain rate of $10^{-5}\ s^{-1}$ the mixture begins to exhibit strain hardening. The model fails to capture this phenomenon. At higher strain rates corresponding to $\tau > \tau_c$, the measurements and the model begin to again show good agreement.

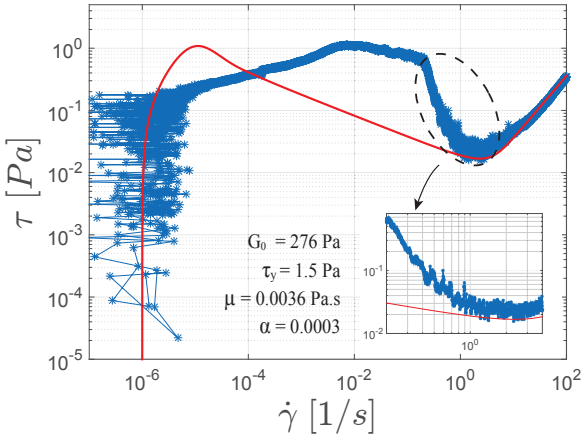

Figure 4.22: Transient stress versus strain rate curve obtained from strain controlled measurements for a sample with 15% concentration after a resting period of 3000 s (blue stars). The solid red line is computed using equations (4.33)-(4.35). The value of the empirical parameters used during the computation are presented inside the plot. The inset plot depicts a zoomed in view of the shear banding instability.

4.5. CONCLUSIONS

A new viscoelastic constitutive relation for modeling of subaqueous clay-rich gravity flows was presented. In order to capture the creep and the yield behavior of the plug

layer within these flows the Kelvin-Voigt model was considered. The total stress is split into an elastic and a viscous part. The importance of the elastic part is determined by the amount of structure. It was explained that for the materials which exhibit a minimum in their strain controlled flow curves the structure parameter must be a symmetric function of the strain rate and the stress. Therefore, the destruction of structure within the material was accounted for using the dissipation energy. An expression for the elastic strain of the flowing structure was then derived.

It was shown that the final set of equations can reproduce the viscosity bifurcation that clay suspensions may exhibit under a given load. This is important for accurate prediction of the run-out distance of gravity flows. The most general flow curves which are allowed by the model were discussed and the response of the model to a constant stress and a constant shear rate input was analyzed. It was concluded that the model can reproduce the well documented responses of pasty materials to such tests.

The final set of equations requires four empirical parameters. A methodology was presented for obtaining these parameters. Power law functions were then obtained for their calculations for a limited rest time of 3000 s.

The capability of the model was evaluated by comparing its output with the data obtained from stress controlled measurements. At low values of strain, i.e., within the linear elastic regime, a relatively good agreement between the data and the model was observed. At the end of the linear elastic regime and within the non-linear elastic regime, a discrepancy between the model output and the data was observed. This may be due to small amounts of slip that may have occurred before yielding. A good agreement between the model and the measurements was observed within the yielding and the viscous regions of the stress versus strain and the stress versus strain rate curves. For stress controlled oscillatory tests, a good agreement was observed between the measured and the computed values of the storage and loss moduli at low stress amplitudes. At high stress amplitudes on the other hand, the model appears to deviate from the measurement. This maybe due to the long duration of the tests which may result in water evaporation and in turn increased viscosity of the mixture. For transient strain controlled curves, a good agreement between the measurements and the model was observed at low and high strain rates. The measurements suggest that at intermediate strain rates, the mixture exhibits strain hardening. The model does not capture this phenomenon.

REFERENCES

Acierno, D., La Mantia, F., Marrucci, G., & Titomanlio, G. (1976). A non-linear viscoelastic model with structure-dependent relaxation times. *Journal of Non-Newtonian Fluid Mechanics*, *1*, 125–146. doi: 10.1016/0377-0257(76)80012-2

Baas, J. H., Best, J. L., & Peakall, J. (2016). Predicting bedforms and primary current stratification in cohesive mixtures of mud and sand. *Journal of the Geological Society*, *173*(1), 12–45. doi: 10.1144/jgs2015-024

Baker, M. L., Baas, J. H., Malarkey, J., Silva Jacinto, R., Craig, M. J., Kane, I. A., & Barker, S. (2017). The Effect of Clay Type On The Properties of Cohesive Sediment Gravity Flows And Their Deposits. *Jornal of Sedimentary Research*, *87*, 1176–1195. doi: 10.2110/jsr.2017.63

Billingham, J., & Ferguson, J. W. J. (1993). Laminar, unidirectional flow of a thixotropic fluid in a circular pipe. *Journal of Non-Newtonian Fluid Mechanics*, *47*, 21–55. doi: 10.1016/0377-0257(93)80043-B

Bird, R. B., Armstrong, R. C., & Hassager, O. (1987). *Dynamics of Polymeric Liquids* (second ed.). John Wiley & Sons.

Bocquet, L., Colin, A., & Ajdari, A. (2009). Kinetic theory of plastic flow in soft glassy materials. *Physical Review Letters*, *103*(3), 1–4. doi: 10.1103/PhysRevLett.103.036001

Cheng, D. C.-H., & Evans, F. (1965). Phenomenological characterization of the rheological behaviour of inelastic reversible thixotropic and antithixotropic fluids. *British Journal of Applied Physics*, *16*, 1599–1617. doi: 10.1088/0508-3443/16/11/301

Coussot, P. (1997). *Mudflow Rheology and Dynamics*. Taylor & Francis.

Coussot, P., Leonov, A. I., & Piau, J. M. (1993). Rheology of concentrated dispersed systems in a low molecular weight matrix. *Journal of Non-Newtonian Fluid Mechanics*, *46*, 179–211. doi: 10.1016/0377-0257(93)85046-D

Coussot, P., Nguyen, Q. D., Huynh, H. T., & Bonn, D. (2002a). Avalanche behavior in yield stress fluids. *Physical Review Letters*, *88*(17), 1755011–1755014. doi: 10.1103/PhysRevLett.88.175501

Coussot, P., Nguyen, Q. D., Huynh, H. T., & Bonn, D. (2002b). Viscosity bifurcation in thixotropic, yielding fluids. *Journal of Rheology*, *46*(3), 573–589. doi: 10.1122/1.1459447

Coussot, P., Roussel, N., Jarny, S., & Chanson, H. (2005). Continuous or catastrophic solid-liquid transition in jammed systems. *Physics of Fluids*, *17*(1). doi: 10.1063/1.1823531

Coussot, P., Tabuteau, H., Chateau, X., Tocquer, L., & Ovarlez, G. (2006). Aging and solid or liquid behavior in pastes. *Journal of Rheology*, *50*(6), 975–994. doi: 10.1122/1.2337259

De Kee, D., & Chan Man Fong, C. F. (1994). Rheological properties of structured fluids. *Polymer Engineering & Science*, *34*(5), 438–445. doi: 10.1002/pen.760340510

de Souza Mendes, P. R. (2009). Modeling the thixotropic behavior of structured fluids. *Journal of Non-Newtonian Fluid Mechanics*, *164*(1-3), 66–75. doi: 10.1016/j.jnnfm.2009.08.005

Derec, C., Ducouret, G., Ajdari, A., & Lequeux, F. (2003). Aging and nonlinear rheology in suspensions of polyethylene oxide–protected silica particles. *Physical Review E*, *67*(6), 9. doi: 10.1103/PhysRevE.67.061403

Dimitriou, C. J., & McKinley, G. H. (2014). A comprehensive constitutive law for waxy crude oil: A thixotropic yield stress fluid. *Soft Matter*, *10*(35), 6619–6644. doi: 10.1039/c4sm00578c

Dullaert, K., & Mewis, J. (2006). A structural kinetics model for thixotropy. *Journal of Non-Newtonian Fluid Mechanics*, *139*, 21–30. doi: 10.1016/j.jnnfm.2006.06.002

Falk, M. L., & Langer, J. S. (1998). Dynamics of viscoplastic deformation in amorphous solids. *Physical Review E*, *57*(6), 7192–7205. doi: 10.1103/PhysRevE.57.7192

Fielding, S. M., Sollich, P., & Cates, M. E. (2000). Ageing and Rheology in Soft Materials. *Journal of Rheology*, *44*(2). doi: 10.1122/1.551088

Fong, C. F. C. M., Turcotte, G., & De Kee, D. (1996). Modelling Steady and Transient Rheological Properties. *Journal of Food Engineering*, *27*, 63–70. doi: 10.1016/0260-8774(94)00077-M

Goodeve, C. F. (1939). A General Theory of Thixotropy and Viscosity. *Trans. Faraday Soc.*, *35*, 342–358. doi: 10.1039/TF9393500342

Hahn, S. J., Ree, T., & Eyring, H. (1959). Flow Mechanism of Thixotropic Substances. *Industrial and Engineering Chemistry*, *51*(7), 856–857. doi: 10.1021/ie50595a038

Healy, T., Wang, Y., & Healy, J. A. (2002). *Muddy Coasts of the World: Processes, Deposits and Function*. Elsevier Science.

Hermidas, N., Eggenhuisen, J. T., Silva Jacinto, R., Luthi, S. M., Toth, F., & Pohl, F. (2018). A Classification of Clay-Rich Subaqueous Density Flow Structures. *Journal of Geophysical Research*, *123*(5), 945–966. doi: 10.1002/2017JF004386

Hermidas, N., Silva Jacinto, R., Eggenhuisen, J. T., & Luthi, S. M. (2019). A new rheological model for thixoelastic materials in subaqueous gravity driven flows. *Journal of Non-Newtonian Fluid Mechanics*, *266*, 102–117. doi: 10.1016/j.jnnfm.2019.02.010

Hewitt, D., & Balmforth, N. (2013). Thixotropic gravity currents. *Journal of Fluid Mechanics*, *727*, 56–82. doi: 10.1017/jfm.2013.235

Holmes, G. C. (2002). The Use of Hyperbolic Cosines in Solving Cubic Polynomials. *The Mathematical Gazette*, *86*(507), 473–477. doi: 10.2307/3621149

Mas, R., & Magnin, A. (1994). Rheology of colloidal suspensions: Case of lubricating greases. *Journal of Rheology*, *38*(4), 889–908. doi: 10.1122/1.550598

Michaels, A. S., & Bolger, J. C. (1962). Settling rates and sediment volumes of flocculated kaolin suspensions. *Industrial and Engineering Chemistry Fundamentals*, *1*(1), 24–33. doi: 10.1021/i160001a004

Moore, F. (1959). The rheology of ceramic slips and bodies. *Transactions of the British Ceramic Society*, *58*, 470–494.

Mujumdar, A., Beris, A. N., & Metzner, A. B. (2002). Transient phenomena in thixotropic systems. *Journal of Non-Newtonian Fluid Mechanics*, *102*, 157–178. doi: 10.1016/s0377-0257(01)00176-8

Olphen, H. V. (1977). *An introduction to clay colloid chemistry: for clay technologists, geologists, and soil scientists*. Wiley.

Peter, S. (1964). Zur Theorie der Rheopexie. *Rheologica Acta*, *3*, 178–180. doi: 10.1007/BF01668885

Pignon, F., Magnin, A., & Piau, J.-M. (1996). Thixotropic colloidal suspensions and flow curves with minimum: Identification of flow regimes and rheometric consequences. *Journal of Rheology*, *40*, 573–587. doi: 10.1122/1.550759

Rivlin, R. S. (1948). The hydrodynamics of non-Newtonian fluids. I. *Proceedings of the Royal Society*, *193*(1033), 260–281. doi: 10.1098/rspa.1948.0044

Rivlin, R. S. (1949). The hydrodynamics of non-Newtonian fluids . II. *proceedings of cambridge philosophical society*, *45*(1), 88–91. doi: 10.1017/S0305004100000463

Roscoe, R. (1950). Mechanical Models for the Representation of Visco-Elastic Properties. *British Journal of Applied Physics*, *1*(7), 171–173. doi: 10.1088/0508-3443/1/7/302

Shampine, L. F., & Reichelt, M. W. (1997). The MATLAB ODE Suite. *SIAM Journal on Scientific Computing*, *18*(1), 1–22. doi: 10.1137/S1064827594276424

Sollich, P., Hébraud, P., & Cates, M. E. (1997). Rheology of Soft Glassy Materials. *Physical Review Letters*, *78*(10). doi: 10.1103/PhysRevLett.78.2020

Tanner, R. I. (2000). *Engineering Rheology*. OUP Oxford.

Toorman, E. a. (1997). Modelling the thixotropic behaviour of dense cohesive sediment suspensions. *Rheologica Acta*, *36*, 56–65. doi: 10.1007/BF00366724

Van Maren, D. S., Winterwerp, J. C., Wang, Z. Y., & Pu, Q. (2009). Suspended sediment dynamics and morphodynamics in the Yellow River, China. *Sedimentology*, *56*(3), 785–806. doi: 10.1111/j.1365-3091.2008.00997.x

Winterwerp, J. C., & van Kesteren, W. G. M. (2004). *Introduction to the Physics of Cohesive Sediment in the Marine Environment*. Elsevier.

Yoshimura, A. S., & Prud'homme, R. K. (1987). Response of an elastic Bingham fluid to oscillatory shear. *Rheologica Acta*, *26*(5), 428–436. doi: 10.1007/BF01333843

Yziquel, F., Carreau, P. J., Moan, M., & Tanguy, P. A. (1999). Rheological modeling of concentrated colloidal suspensions. *Journal of Non-Newtonian Fluid Mechanics*, *86*, 133–155. doi: 10.1016/S0377-0257(98)00206-7

5

BOUNDARY LAYER THEORY AND MODELING OF CLAY-LADEN FLOWS

Everything must be made as simple as possible. But not simpler.

Albert Einstein

In this study, the validity of the boundary layer approximation for clay-laden flows past a flat plate is analyzed using the rheological model presented in the previous chapter. Using the boundary layer approximation, a simplified set of equations is then derived for clay-laden free surface flows. It is concluded that the boundary layer approximation becomes less appropriate for high sediment concentrations. The steady state solutions of the clay-laden free surface flow equations are examined for various cases. The results suggest that these flows can stay mobile on very low gradients.

5.1. INTRODUCTION

PROCESS-BASED modeling of clay-laden gravity flows is riddled with physical complexities (Iverson, 1997), e.g., non-linear convection terms, sediment-water rheology, particle-particle interaction, particle-fluid interaction. Due to computational limitations, therefore, concession has to be made with regards to the level of physical detail that can be included in such models.

For dilute suspensions, i.e., particle volume fractions $< 10^{-3}$, it is feasible to consider only one- or two-way coupling between the particle phase and the fluid phase (Marble, 1970; Meiburg et al., 2017; Uhlmann, 2008). A classification of the computational approaches in this regime was presented by Balachandar (2009). For denser suspensions (particle volume fractions $> 10^{-3}$), on the other hand, also the effect of particle-particle interaction (four-way coupling) becomes important (Elghobashi & Truesdell, 1993; Vreman et al., 2009). However, due to the high computational costs involved in considering

four- or even two-way coupling, computational efforts of practical interest for mass gravity flows are generally focused on simplified models of the end members, i.e., (1) debris flows (Jiang & LeBlond, 1992; Pratson et al., 2000), and (2) turbidity currents (Groenenberg et al., 2009; Sequeiros et al., 2009), in which all the phases (solid as well as fluid) are treated as a single fluid.

In these models, the physical complexities are often mitigated through the widely used boundary layer theory, first propounded by Prandtl (Tollmien et al., 1961). In this approach, based on the geometrical characteristic of the flow, i.e., thinness of the boundary layer compared to the length scales in the flow direction, the unwieldy Navier-Stokes equations are reduced to the easier-to-tackle boundary layer equations (Groenenberg et al., 2009; Huang & Garcia, 1998; Jiang & LeBlond, 1992; Pratson et al., 2000).

For Newtonian fluids and at high Reynolds numbers, the predictions made by the boundary layer theory are generally in good agreement with the experimental results (Schlichting, 1964). For non-Newtonian fluids on the other hand, the theory is a subject of research (Acrivos et al., 1960; Balmforth et al., 2017; Oldroyd, 1947; Rajagopal et al., 1980; Ruckenstein, 1994). A lesser known topic in this domain is the boundary layer of thixotropic fluids (Anwar et al., 2008; Harris, 1977; Sadeqi et al., 2011).

Kármán (1921) put forth an integral analysis which can lead to the dimensional analysis of boundary layer approximation. Therefore, this approach, together with the rheological model presented in Chapter 4, are used in this study to investigate the validity of the boundary layer approximation for clay-laden flows.

The discussion in Chapter 3 suggests that the numerical models which aim to accurately simulate the behavior of clay-laden flows, e.g., their run-out distance, should at the very least employ constitutive models that can capture the rheology of sediment-water suspensions. This is in contrast to the common numerical practices that often rely on time-independent constitutive models, e.g., the Bingham plastic, or the Herschel–Bulkley, for modeling of such flows (Cantelli, 2009; Huang & Garcia, 1998; Jiang & Le Blond, 1993; L. Jing et al., 2018; M. Pastor et al., 2015; Pratson et al., 2000; van Kessel & Kranenburg, 1996). Therefore, in this contribution, the boundary layer approximation and the rheological model presented in Chapter 4 are used to derive a simplified set of equations for modeling clay-laden free surface flows. The steady state solutions of these equations will be examined for various cases.

5.2. BOUNDARY LAYER THEORY

Here we will follow the approach first introduced by Kármán (1921) to derive an expression for the boundary layer thickness of clay-laden flows.

Consider a control volume of clay-rich suspension flowing past a flat plate depicted in Figure 5.1. Assuming constant density, ρ, within the boundary layer, the equations for the displacement thickness, δ^*, and the momentum thickness, θ, can be written as (White, 1991),

$$\delta^* = \int_0^{\delta} \left(1 - \frac{u}{u_p}\right) dy, \tag{5.1}$$

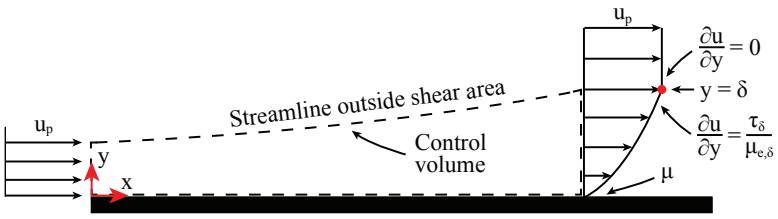

Figure 5.1: Flow past a flat plate.

and,

$$\frac{D}{\rho u_p^2} = \theta = \int_0^\delta \frac{u}{u_p}\left(1 - \frac{u}{u_p}\right) dy, \tag{5.2}$$

where, u is the flow velocity, u_p is the velocity of the plug layer, and D is the drag force. Ideally, for a viscoelastic fluid in two dimensions, the drag force is composed of integrals of τ^{11} and τ^{21} (Section 4.2.4) (Harris, 1977). However, within the boundary layer and below the plug layer we will assume that the shear rate is high enough that τ^{11} becomes negligible compared to τ^{21}.
The friction coefficient can be written as,

$$C_f = \frac{\tau_w}{\frac{1}{2}\rho u_p^2} = 2\frac{d\theta}{dx}, \tag{5.3}$$

where,

$$\tau_w = \mu \frac{\partial u}{\partial y}|_{y=0}, \tag{5.4}$$

is the wall shear stress and μ is the viscosity of the fluid at the wall. Assuming high shear rate values at the wall, $\mu \approx \mu(\lambda = 0)$, where λ is the structure parameter whose value ranges from 1, for a completely structured material, to 0, for a material with no structure (Chapter 4).
The velocity profile within the boundary layer satisfies three physical conditions,

$$u(0) = 0, \;\; u(\delta) = u_p, \;\; \frac{\partial u}{\partial y}|_{y=\delta^-} = \frac{\tau_\delta}{\mu_{e,\delta}}, \tag{5.5}$$

where, τ_δ, $\mu_{e,\delta}$, and $\frac{\partial u}{\partial y}|_{y=\delta^-}$, are the stress, the apparent viscosity of the fluid, and the shear rate, just below the plug layer (Figure 5.1).
At $y = \delta$, if $\tau_\delta < \tau_c$, then the plug begins to grow towards the wall. Furthermore, if $\tau_y < \tau_\delta$, then the boundary layer begins to eat away at the plug. Therefore, in a steady state, $\tau_c \leq \tau_\delta \leq \tau_y$.
For laminar flows, the conditions in (5.5) can be satisfied by the second order polynomial,

$$u(y) = \left(\frac{2u_p}{\delta} - \frac{\tau_\delta}{\mu_{e,\delta}}\right) y + \left(\frac{\tau_\delta}{\mu_{e,\delta}\delta} - \frac{u_p}{\delta^2}\right) y^2. \tag{5.6}$$

Inserting this approximate velocity profile into the equation (5.1) yields,

$$\delta^* = \frac{\tau_\delta}{6\mu_{e,\delta} u_p}\delta^2 + \frac{1}{3}\delta. \tag{5.7}$$

Inserting (5.6) into equations (5.2) and (5.4) yields,

$$\theta = -\left(\frac{\tau_\delta}{\mu_{e,\delta} u_p}\right)^2 \frac{\delta^3}{30} + \frac{2\delta}{15} + \frac{\tau_\delta}{\mu_{e,\delta} u_p}\frac{\delta^2}{15}, \tag{5.8}$$

and,

$$\tau_w = \mu \frac{\partial u}{\partial y}|_{y=0} = \left(\frac{2u_p\mu}{\delta} - \frac{\tau_\delta \mu}{\mu_{e,\delta}}\right). \tag{5.9}$$

Inserting (5.8) and (5.9) in equation (5.3) yields,

$$\left(-\frac{\tau_\delta^2 \rho}{\mu_{e,\delta}}\frac{3}{15}\delta^3 + \tau_\delta \rho u_p \frac{4}{15}\delta^2 + \frac{4\rho u_p^2 \mu_{e,\delta}}{15}\delta\right)\frac{d\delta}{dx} = 4\mu\mu_{e,\delta} u_p - 2\tau_\delta \mu\delta. \tag{5.10}$$

Equation (5.10) is an ordinary differential equation that can be solved to obtain the boundary layer thickness. The rheological properties of sediment-water suspensions are incorporated in (5.10) through specification of the value of the shear rate below the plug layer. In what follows we will focus on solving the equation (5.10) for different sediment volume concentrations (i.e., different values of the structure build up rate, α, the static yield stress, τ_y, the zero-structure viscosity, μ, and the modulus of elasticity G_0) for the two extreme cases: 1) ($\tau_\delta = \tau_c$, $\mu_{e,\delta} = \mu_{e,c}$), and 2) ($\tau_\delta = \tau_y$, $\mu_{e,\delta} = \mu_{e,y}$), where, $\mu_{e,c}$ and $\mu_{e,y}$ are the apparent viscosities corresponding to the critical and the static yield stresses. In steady state conditions, the boundary layer thickness falls between the ones belonging to these two extreme cases.
Performing dimensional analysis on equation (5.10) yields,

$$\frac{\delta}{x} \sim \frac{1}{Re_{BL}}, \tag{5.11}$$

where, $Re_{BL} = \rho u_p \delta/\mu$, is the boundary layer Reynolds number.
Equation (5.10) does not take into account the effect of gravity. Therefore, for the case where sediment is pumped into a flume with a bed inclination, equation (5.10) is only valid if the gravitational forces are small compared to the inertial and stress forces (i.e., small slopes). In the next section we will look to improve our analysis by incorporating the effect of gravity in the momentum equation.

5.3. A MODEL FOR FREE SURFACE CLAY-LADEN FLOWS

Let us confine ourselves to two-dimensional incompressible flow for which the continuity and the momentum equations are,

$$\frac{\partial u}{\partial x}+\frac{\partial v}{\partial y} = 0, \tag{5.12}$$

$$\frac{\partial u}{\partial t}+u\frac{\partial u}{\partial x}+v\frac{\partial u}{\partial y} = -\frac{1}{\rho_f}\frac{\partial p}{\partial x}+\frac{\left(\rho_f-\rho_w\right)}{\rho_f}g\sin(\theta)+\frac{1}{\rho_f}\frac{\partial \tau^{11}}{\partial x}+\frac{1}{\rho_f}\frac{\partial \tau^{12}}{\partial y}, \tag{5.13}$$

$$\frac{\partial v}{\partial t}+u\frac{\partial v}{\partial x}+v\frac{\partial v}{\partial y} = -\frac{1}{\rho_f}\frac{\partial p}{\partial y}+\frac{\left(\rho_f-\rho_w\right)}{\rho_f}g\cos(\theta)+\frac{1}{\rho_f}\frac{\partial \tau^{12}}{\partial x}+\frac{1}{\rho_f}\frac{\partial \tau^{22}}{\partial y}, \tag{5.14}$$

where, u and v are the velocity components in the x and y directions, p is the pressure, τ^{11} and τ^{12} are the normal and the shear components of the stress tensor, and θ is the bed slope [1]. $\rho_f=\left(\rho_s-\rho_w\right)C+\rho_w$, where ρ_s is the particle density, ρ_w is the density of water, and C is the sediment volume concentration.
For the sake of simplicity we will ignore the terms $\partial\tau^{11}/\partial x$ and $\partial\tau^{22}/\partial y$ (note that, $\tau^{22}=0$, for the case of steady simple shear flow). Furthermore, $\tau^{12}=\tilde{\mu}\partial u/\partial y$, where $\tilde{\mu}$ is the apparent viscosity.
We then define the following dimensionless variables,

$$x^*=\frac{x}{L},\ y^*=\frac{y}{\delta},\ t^*=\frac{tu_p}{L},\ u^*=\frac{u}{u_p},\ v^*=\frac{vL}{u_p\delta},\ p*=\frac{p-p_0}{\rho_f u_p^2},\ \tilde{\mu}^*=\frac{\tilde{\mu}}{\mu}, \tag{5.15}$$

where, δ is the boundary layer height, L is a reference length scale in the x direction, u_p is the plug velocity, p_0 is a reference pressure, and μ is the steady state apparent viscosity at the bed where, it is assumed that $\lambda\approx 0$.
Using these non-dimensional variables and noting that $\frac{\delta}{x}\sim\frac{1}{Re_{BL}}$, equations (5.12) to (5.14) can be written as,

$$\frac{\partial u}{\partial x}+\frac{\partial v}{\partial y} = 0, \tag{5.16}$$

$$\frac{\partial u}{\partial t}+u\frac{\partial u}{\partial x}+v\frac{\partial u}{\partial y} = -\frac{\partial p}{\partial x}+\left[\frac{\left(\rho_f-\rho_w\right)}{\rho_f}\frac{gL}{u_p^2}\sin(\theta)\right]+\ldots + \frac{\partial \tau^{12}}{\partial y}, \tag{5.17}$$

$$\frac{\partial v}{\partial t}+u\frac{\partial v}{\partial x}+v\frac{\partial v}{\partial y} = -\left[Re_{BL}^2\right]\frac{\partial p}{\partial y}+\ldots + \left[\frac{\left(\rho_f-\rho_w\right)}{\rho_f}\frac{gL}{u_p^2}\cos(\theta)Re_{BL}\right]+\frac{\partial \tau^{12}}{\partial x}. \tag{5.18}$$

[1] Note that θ does not represent the momentum thickness in these equations.

where, we have omitted the star notation for simplicity.
For high values of Re_{BL} (boundary layer approximation), from (5.16) to (5.18) we retain,

$$\frac{\partial u}{\partial x}+\frac{\partial v}{\partial y} = 0, \tag{5.19}$$

$$\frac{\partial u}{\partial t}+u\frac{\partial u}{\partial x}+v\frac{\partial u}{\partial y} = -\frac{\partial p}{\partial x}+\frac{(\rho_f-\rho_w)}{\rho_f}\frac{1}{Fr^2}\sin(\theta)+\frac{\partial \tau^{12}}{\partial y}, \tag{5.20}$$

$$0 = -\frac{\partial p}{\partial y}, \tag{5.21}$$

where, $Fr=\sqrt{u_p^2/gL}$ is the Froude number. These are the well-known boundary layer equations (White, 1991), which in dimensional form become,

$$\frac{\partial u}{\partial x}+\frac{\partial v}{\partial y} = 0, \tag{5.22}$$

$$\frac{\partial u}{\partial t}+u\frac{\partial u}{\partial x}+v\frac{\partial u}{\partial y} = -\frac{1}{\rho_f}\frac{\partial p}{\partial x}+\frac{(\rho_f-\rho_w)}{\rho_f}g\sin(\theta)+\frac{1}{\rho_f}\frac{\partial \tau^{12}}{\partial y}, \tag{5.23}$$

$$0 = -\frac{\partial p}{\partial y}. \tag{5.24}$$

Following Reynolds averaging procedure, the flow variables in equations (5.22) to (5.24) may be split into a time averaged component denoted by $\bar{}$, and a fluctuating component denoted by $'$, e.g., $u=\bar{u}+u'$. Performing time averaging on the resulting equations (and noting that $\frac{\partial \overline{u'^2}}{\partial x}$ is a factor $\frac{1}{Re_{BL}}$ smaller than $\frac{\partial \overline{u'v'}}{\partial y}$) then yields,

$$\frac{\partial \bar{u}}{\partial x}+\frac{\partial \bar{v}}{\partial y} = 0, \tag{5.25}$$

$$\rho_f\left(\frac{\partial \bar{u}}{\partial t}+\bar{u}\frac{\partial \bar{u}}{\partial x}+\bar{v}\frac{\partial \bar{u}}{\partial y}\right) = -\frac{\partial \bar{p}}{\partial x}+(\rho_f-\rho_w)g\sin(\theta)+\frac{\partial(\overline{\tau^{12}}+\overline{\tau^{12'}}-\rho_f\overline{u'v'})}{\partial y}, \tag{5.26}$$

$$0 = -\frac{\partial \bar{p}}{\partial y}. \tag{5.27}$$

From equation (2.6) it can be seen that $\overline{\tau^{12'}}\neq 0$. The time averaged total stress is then written as $\bar{\hat{\tau}}=\overline{\tau^{12}}+\overline{\tau^{12'}}-\rho_f\overline{u'v'}$.
We further simplify these equations by assuming that the downslope gradients are small, i.e., $\partial p/\partial x\approx\partial u/\partial x\approx\partial v/\partial x\approx 0$. This results in the following set of equations,

$$\frac{\partial \bar{u}}{\partial t} = \frac{(\rho_f-\rho_w)}{\rho_f}g\sin(\theta)+\frac{1}{\rho_f}\frac{\partial \bar{\hat{\tau}}}{\partial y}, \tag{5.28}$$

$$\overline{\tau^{12}} = G_0\lambda\gamma_r+\mu\dot{\gamma}, \tag{5.29}$$

$$\frac{\partial \lambda}{\partial t} = \alpha(1-\lambda)-|\tau:\dot{\gamma}|\beta\lambda, \tag{5.30}$$

$$\frac{\partial \gamma_r}{\partial t} = \dot{\gamma}-\frac{\alpha(1-\lambda)}{\lambda}\gamma_r, \tag{5.31}$$

where, λ is the structure parameter, γ_r is the residual strain, G_0 is the modulus of elasticity, α is the structure build up rate, μ is the viscosity of a material with zero structure, and $\beta = G_0/\tau_y^2$, where τ_y is the static yield stress (Chapter 4).
Considering no slip between the flow and the bed and ignoring the stress between the density flow and the overlying water results in the following boundary conditions for these equations,

$$\bar{u}(0,t) = 0,\ \bar{\hat{\tau}}(h,t) = 0, \tag{5.32}$$

where, h is the flow height (Figure 5.2).

5.3.1. ESTIMATING TURBULENT STRESS

Due to turbulence, the expression for the total stress is complicated by the two new terms: $\overline{\tau^{12'}}$, and $-\rho_f \overline{u'v'}$, in the mean momentum equation (5.28). Since the analytic forms of these terms are not known, empirical results obtained from Chapter 2 are used to estimate the value of the total stress. Accordingly, instead of the laminar apparent viscosity, the compounded apparent viscosity is considered. From (2.8), then for the total stress one has,

$$\bar{\hat{\tau}} = \tilde{\mu}_{BL}\dot{\gamma}, \tag{5.33}$$

where, $\tilde{\mu}_{BL}$ is the compounded apparent viscosity and $\dot{\gamma}$ is the strain rate. For laminar flows, this expression reduces to,

$$\tau = \mu_{BL}\dot{\gamma}, \tag{5.34}$$

where, μ_{BL} is the laminar apparent viscosity.
Dividing (5.33) by (5.34) yields,

$$\bar{\hat{\tau}}/\tau = \tilde{\mu}_{BL}/\mu_{BL}. \tag{5.35}$$

In order to approximate the total stress, the laminar stress at each time step is calculated from equation (5.29). Then, using the linear fit in Figure 2.9 and equation (5.35),

$$\bar{\hat{\tau}} = \begin{cases} \tau f(Re_{BL}) & 1 < \tilde{\mu}_{BL}/\mu_{BL}, \\ \tau & \tilde{\mu}_{BL}/\mu_{BL} \leq 1, \end{cases} \tag{5.36}$$

where, $f(Re_{BL}) = e^{-2.2+0.6\,ln(Re_{BL})}$.
Since for $Re_{BL} \lesssim 39.1$, in the expression (5.36), one has $\bar{\hat{\tau}}/\tau = 1$, the effect of turbulence is only incorporated in the calculations when $Re_{BL} \gtrsim 39.1$. This corresponds to the inner variable $z^+ \gtrsim 30$ (Figure 2.8(a)), at which, a logarithmic overlap region initially begins to form.
The function $f(Re_{BL})$ in (5.36) adjusts the laminar stress profile such that the value of the stress within the boundary layer corresponds to the total stress in this region.

5.3.2. DISCRETIZATION

Equation (5.28) is discretized using the explicit Euler method,

$$\bar{u}^{n}_{i+1/2} = \bar{u}^{n-1}_{i+1/2} + \Delta t \left(\frac{(\rho_f - \rho_w)}{\rho_f} g \sin(\theta) + \frac{1}{\rho_f} \frac{\bar{\hat{\tau}}_{i+1} - \bar{\hat{\tau}}_i}{\Delta y} \right)^{n-1}. \tag{5.37}$$

At each time step equations (5.29) to (5.31) are solved and the stress term is advanced in time from t_{n-1} to t_n, where, $\Delta t = t_n - t_{n-1}$, using a variable-step, variable-order solver based on the numerical differentiation formulas (Shampine & Reichelt, 1997). The resulting stress field, τ_n, is then used to advance the velocity field in time. The staggered grid used to solve the equations (5.28) to (5.31) is shown in Figure 5.2.

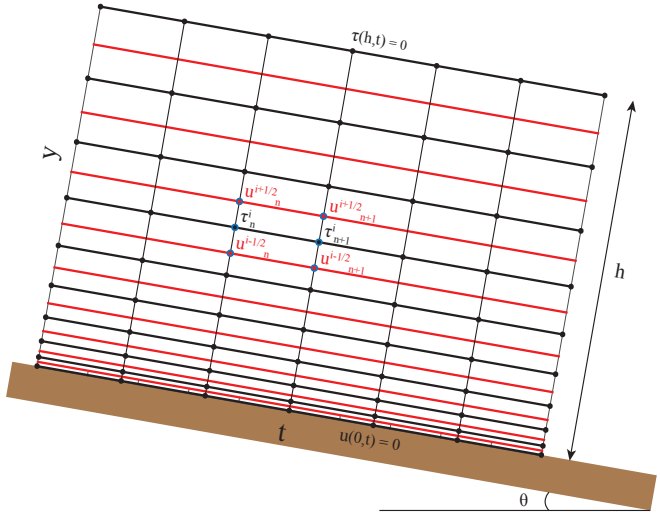

Figure 5.2: The staggered grid used for solving equations (5.28) to (5.31).

5.4. RESULTS AND DISCUSSIONS

In this section, first the results obtained from solving the equation (5.10) are presented for different sediment concentrations. Subsequently, the results of solving the equations (5.28) to (5.31) for one-meter thick flows of sediment with various concentrations and on different slopes are presented.

5.4.1. NUMERICAL RESULTS OBTAINED FROM EQUATION (5.10)

Figure 5.3 shows the results of solving the equation (5.10) for various values of α, τ_y, μ, and G_0, corresponding to 0%, 9%, 12.65%, 15%, 17.82%, and 21% sediment concentrations.

It can be seen that the thickness of the boundary layer increases for higher sediment concentrations. This is due to the fact that for higher concentrations, the viscosity increases

dramatically. Consequently, Re_{BL} decreases considerably, which according to (5.11), results in larger boundary layer thicknesses. At 2.7 meters from the leading edge, for 0% concentration, $x/\delta \sim 300$, while for 21%, $x/\delta \sim 45$.
Furthermore, for case 1, i.e., ($\tau_\delta = \tau_c$, $\mu_{e,\delta} = \mu_{e,c}$), boundary layers are thicker than for case 2, i.e., ($\tau_\delta = \tau_y$, $\mu_{e,\delta} = \mu_{e,y}$). This has to do with the fact that $\tau_y > \tau_c$, which results in a lower structure parameter below the plug layer for case 2 compared to case 1. Consequently, from equation (4.22), $\mu_{e,y} < \mu_{e,c}$ which again according to (5.11), results in larger boundary layer thicknesses for case 1 compared to case 2. The difference between the results obtained for the two cases diminishes for lower concentrations, and for 0%, it vanishes.

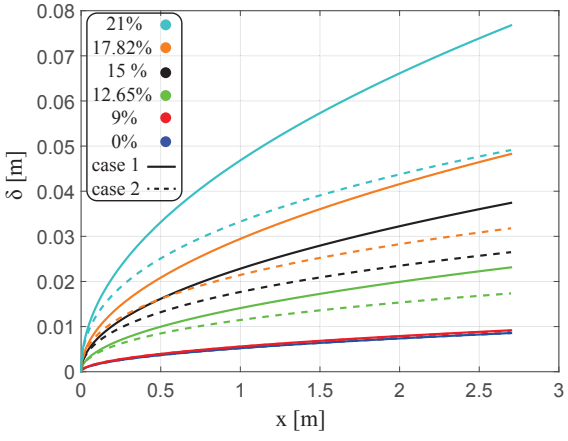

Figure 5.3: Laminar boundary layer thicknesses, δ's, obtained from equation (5.10), for 0%, 9%, 12.65%, 15%, 17.82%, and 21% sediment volume concentrations. Solid lines pertain to case 1, i.e., ($\tau_\delta = \tau_c$, $\mu_{e,\delta} = \mu_{e,c}$), and dashed lines pertain to case 2, i.e., ($\tau_\delta = \tau_y$, $\mu_{e,\delta} = \mu_{e,y}$). The velocity of the plug layer was set to $u_p = 1\ m/s$.

Figure 5.4 shows boundary layer thickness contours obtained from flume experiments performed using sand-clay-water and sand-silt-clay-water mixtures. At smaller slopes, the data suggests larger boundary layer thicknesses for flows with higher sediment concentrations. This is in agreement with the numerical results presented in Figure 5.3. Comparing Figures 5.3 and 5.4 suggests that at low concentrations, equation (5.10) agrees well with the experimental data. This is curious because, for lower concentrations the flow within the boundary layer is more turbulent. Therefore, thicker boundary layers may be expected for these flows. Nonetheless, the data shows a relatively good agreement with the results that correspond to laminar flows. An explanation for this agreement may lie in the interactions between the turbulent boundary and free shear layers. However, this point requires further investigation. At higher concentrations, the model appears to vastly over-predict the size of the boundary layer thickness. This maybe because the gravitational force was neglected in the derivation of the equation (5.10).

Figure 5.5 shows the gradient of the displacement thickness calculated from equation (5.7). It can be seen that $d\delta^*/dx$ grows with the sediment concentration. For 21%

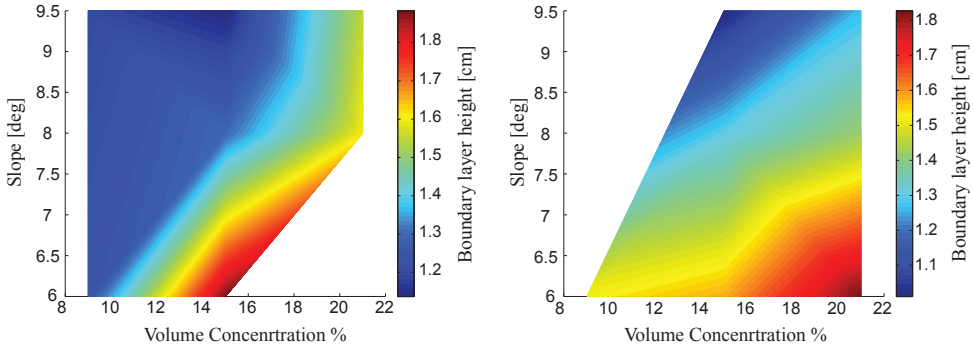

(a) Sand-Clay Runs, Disch. rate 15 [m^3/h]

(b) Silt-Sand-Clay Runs, Disch. rate 15 [m^3/h]

Figure 5.4: Boundary layer thickness contours for (a) sand-clay-water runs, and (b) sand-silt-clay-water runs, obtained at 2.7 m from the inlet, as a function of concentration and slope.

5

sediment concentration it is ~ 10 times higher than for 0% sediment concentration. Furthermore, it can be seen that for case 2, $d\delta^*/dx$, is higher than for case 1, and that away from the origin, i.e., $(x = 0, y = 0)$, it decreases dramatically for both cases.

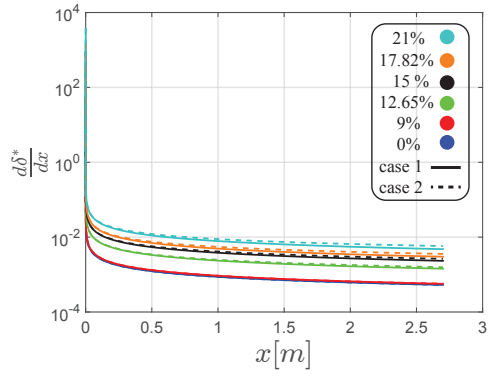

Figure 5.5: Change in the gradient of the displacement thickness, $d\delta^*/dx$, for case 1 (solid lines) and case 2 (dashed lines) along the bed for various sediment concentrations.

Figure 5.6 shows contours of $log_{10}(\partial u/\partial y)$ for case 1, calculated from equation (5.6) for different sediment concentrations. It can be seen that $\partial u/\partial y$ attains its lowest values at the edge of the boundary layer and its highest values at the bed. The difference between the highest and the lowest values of $\partial u/\partial y$ become less significant for higher sediment concentrations. Figure 5.7 shows contours of $log_{10}(\partial u/\partial y)$ for case 2. It can be seen that close to the origin, i.e., $(x = 0, y = 0)$, $\partial u/\partial y$ increases when moving from the edge of the boundary layer towards the bed. However, for high concentrations, this trend changes far from the origin and $\partial u/\partial y$ starts to decrease when moving from the edge of the boundary layer towards the bed. For 17.82% concentration, this change occurs at $x \approx 1.3\ m$, while for 21% concentration it occurs at $x \approx 1\ m$. Therefore, for higher

concentrations, this trend seems to move towards the origin.

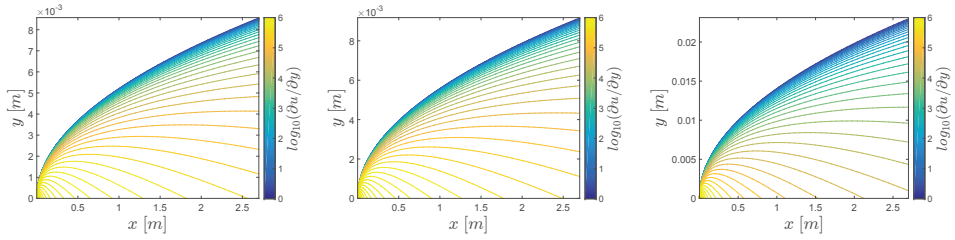

(a) 0% concentration (b) 9% concentration (c) 12.65% concentration

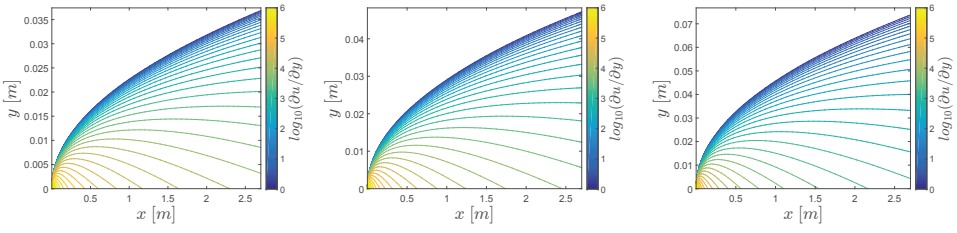

(d) 15% concentration (e) 17.82% concentration (f) 21% concentration

Figure 5.6: Contours of $log_{10}(\partial u/\partial y)$ for case 1, calculated from equation (5.6) for different sediment concentrations.

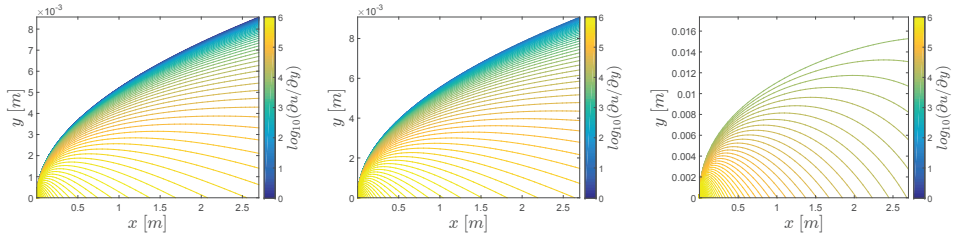

(a) 0% concentration (b) 9% concentration (c) 12.65% concentration

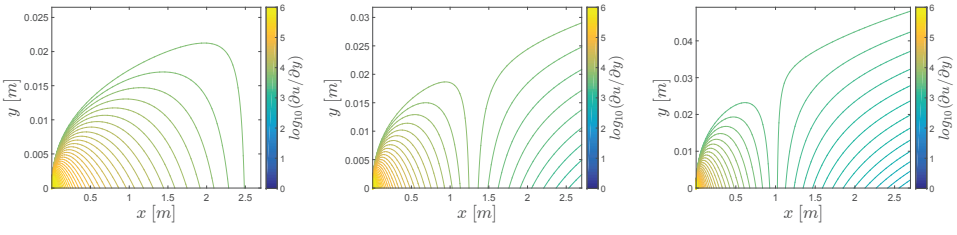

(d) 15% concentration (e) 17.82% concentration (f) 21% concentration

Figure 5.7: Contours of $log_{10}(\partial u/\partial y)$ for case 2, calculated from equation (5.6) for different sediment concentrations.

Figures 5.8 and 5.9 show contours of $|\partial u/\partial y|/|\partial u/\partial x|$ for cases 1 and 2. It can be seen that close to the bed, $|\partial u/\partial y|/|\partial u/\partial x|$ is very high and decreases dramatically when moving towards the edge of the boundary layer. For higher concentrations this dramatic decrease occurs closer to the bed, and for case 2 even more so compared to case 1. For the highest concentration, i.e., 21%, $|\partial u/\partial y|/|\partial u/\partial x| \sim 3000$ close to the bed and ~ 100 close to the edge of the boundary layer. For 0% concentration, $|\partial u/\partial y|/|\partial u/\partial x| \sim 6000$ close to the bed and ~ 600 close to the edge of the boundary layer.

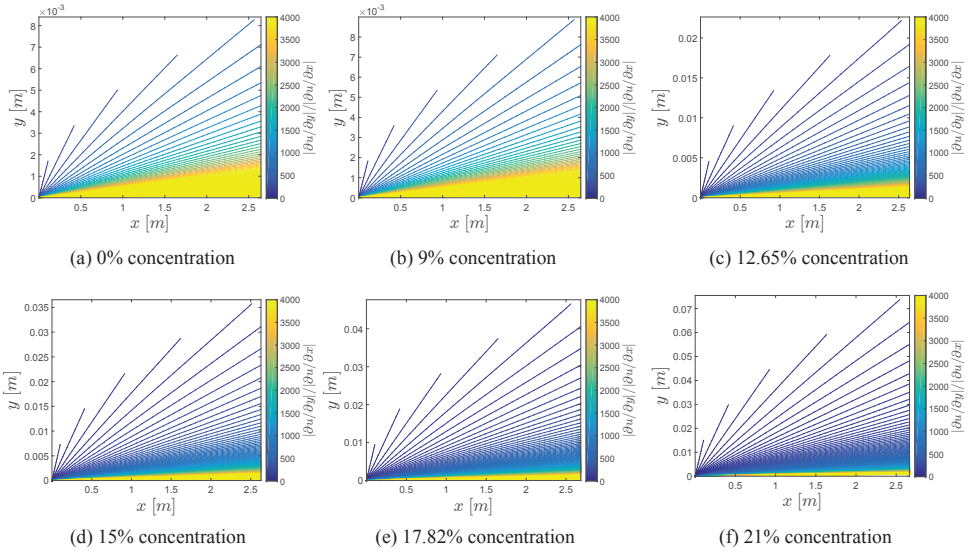

(a) 0% concentration (b) 9% concentration (c) 12.65% concentration

(d) 15% concentration (e) 17.82% concentration (f) 21% concentration

Figure 5.8: Contours of $|\partial u/\partial y|/|\partial u/\partial x|$ for case 1 calculated for various sediment concentrations.

5.4.2. MODELING FREE SURFACE CLAY-LADEN FLOWS

Figure 5.10 shows the steady state profiles of u, $\dot{\gamma}$, τ, λ, and $\zeta = \gamma_r \lambda$, calculated from equations (5.28) to (5.31), for a one-meter thick flow of cohesive sediment-water mixture with the volume concentration of 21%, and on a bed slope of 0.1°. At the edge of the boundary layer, it can be seen that the model predicts a C^1 discontinuity in the velocity profile. A linear stress profile is predicted by the model throughout the sediment layer. The value of the structure parameter, λ, is very low ($\sim 10^{-7}$) at the bed, and grows only slightly from the bed until the edge of the boundary layer. At the edge of the boundary layer λ shows a jump to ~ 0.41. Above the boundary layer and until the height of $z \approx 0.9\ m$, λ shows a slight growth. Since zero stress is imposed on top of the sediment layer, λ shows a second jump at $z \approx 0.9\ m$ and grows to 1 at the height of $z = 1\ m$. The value of ζ is approximately zero within the boundary layer and shows a jump to $\sim 10^{-5}$ at the edge of the boundary layer. From the bottom to the top of the plug layer the value of ζ decreases from $\sim 10^{-5}$ to zero.

Figure 5.11 shows the steady state velocity profiles of one-meter thick flows of cohesive sediment-water mixtures with volume concentrations of 9%, 15%, and 21%, on a

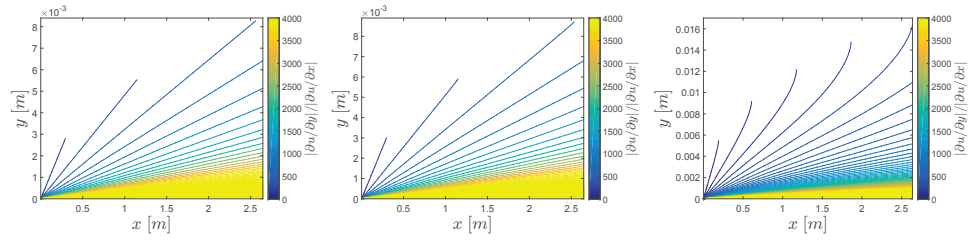

(a) 0% concentration (b) 9% concentration (c) 12.65% concentration

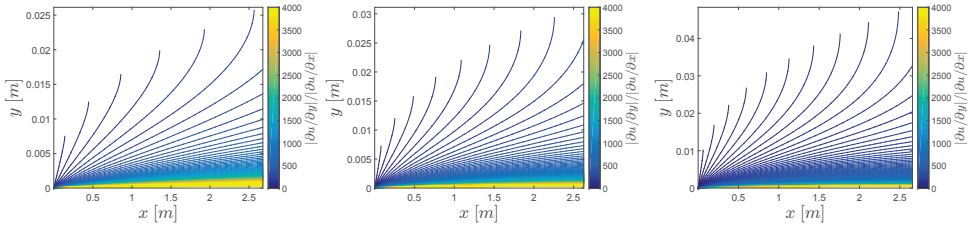

(d) 15% concentration (e) 17.82% concentration (f) 21% concentration

Figure 5.9: Contours of $|\partial u/\partial y|/|\partial u/\partial x|$ for case 2 calculated for various sediment concentrations.

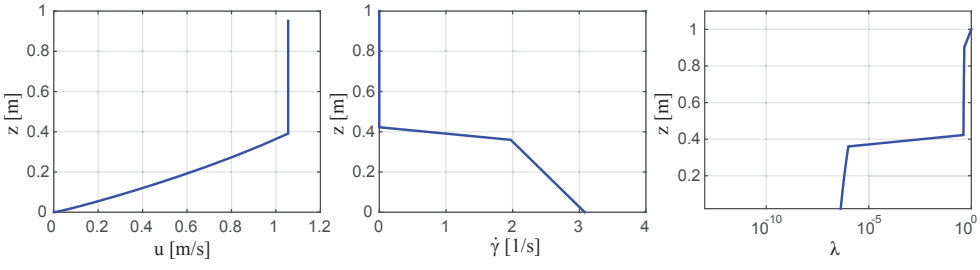

(a) Velocity profile (b) Shear rate profile (c) Structure parameter profile

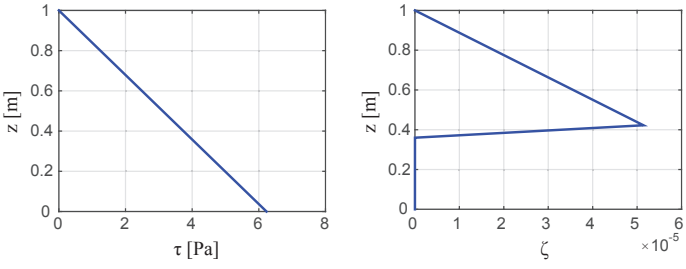

(d) Stress profile (e) ζ profile

Figure 5.10: Steady state profiles of u, $\dot{\gamma}$, τ, λ, and ζ obtained from solving equations (5.28) to (5.31) for a one-meter thick flow of cohesive sediment-water mixture with a volume concentration of 21%, on a bed slope of 0.1°.

bed slope of 0.1°. It can be seen that the highest velocities are predicted for the 9% sediment concentration. Furthermore, according to the model, increasing the sediment volume concentration from 9% to 21% results in an initial decrease followed by an increase in the boundary layer height. The magnitude of the velocity varies non-monotonically with the concentration. It initially decreases with increasing the sediment concentration from 9% to 15%. However, further increasing the concentration from 15% to 21%, results in a slight increase in the velocity.

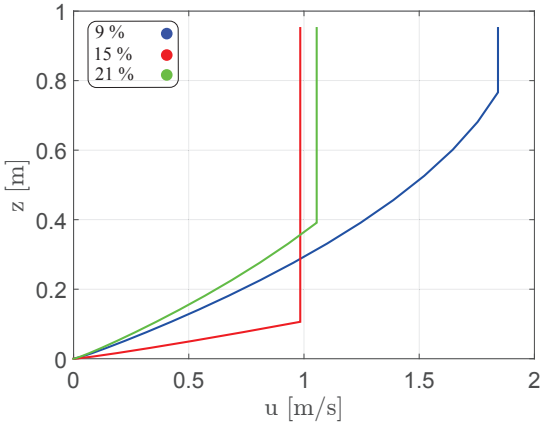

Figure 5.11: Steady state velocity profiles of one-meter thick flows of cohesive sediment-water mixtures with volume concentrations of 9%, 15%, and 21%, on a bed slope of 0.1°.

Figure 5.12 shows the steady state velocity profiles of one-meter thick flows of cohesive sediment-water mixtures with volume concentrations of 9%, 15%, and 21%, on a slope which was varied from 0.1°, to 0.01°, and finally to 0.0001°. Decreasing the slope from 0.1° to 0.01°, resulted in a decrease in the flow velocities. The thicknesses of the boundary layers, however, remained unchanged. Further decreasing the slope from 0.01° to 0.0001°, resulted in the stoppage of the flows with 15%, and 21% concentrations. This is due to the fact that on this slope the stresses at the bed fall below the critical yield stresses required to keep these suspensions mobile. The boundary layer thickness of the suspension with 9% concentration dramatically decreased on this slope.

5.5. CONCLUSION

Boundary layer approximation is predicated upon the existence of the following inequalities (White, 1991):

$$\delta \ll x, \; v \ll u, \; \frac{\partial u}{\partial x} \ll \frac{\partial u}{\partial y}, \; \frac{\partial v}{\partial x} \ll \frac{\partial v}{\partial y}. \tag{5.38}$$

The results in this study suggest that for higher sediment concentrations:

1) x/δ decreases,

2) $d\delta^*/dx$ increases, and since $v/u \leq d\delta^*/dx \Rightarrow v/u$ increases,

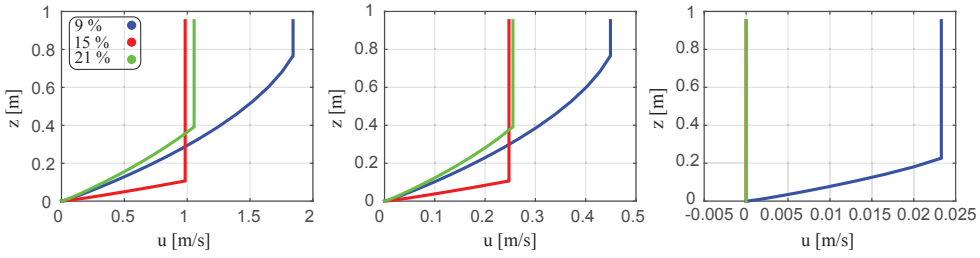

(a) Slope 0.1°. (b) Slope 0.01°. (c) Slope 0.0001°.

Figure 5.12: Steady state velocity profiles of one-meter thick flows of cohesive sediment-water mixtures, with volume concentrations of 9%, 15%, and 21%, on bed slopes of (a) 0.1°, (b) 0.01°, and (c) 0.0001°.

3) $\frac{du}{dy}/\frac{du}{dx}$ decreases,

4) and from (2) and (3), it can be concluded that $\frac{dv}{dy}/\frac{dv}{dx}$ decreases.

5

For sediment concentrations considered here, the boundary layer approximation may still produce reliable results. For increasing concentrations however, the results suggest that this approximation slowly begins to break down.
A set of equations for modeling free surface clay-laden flows was presented using the boundary layer approximation. For equilibrium conditions, the model predicts flow stoppage to occur only over slopes at which the bed stress falls below the critical yield stress of the suspension. This is important for accurate prediction of the run-out distance of clay-laden flows. Furthermore, it was explained that the model can capture the C^1 discontinuity that exists at the edge of the boundary layer in the velocity profiles of these flows.
The effect of sediment concentration on the velocity profiles of clay-laden flows was studied. The following observation were made:

1) For increasing sediment volume concentrations, the model predicts an initial decrease followed by an increase in the boundary layer height.

2) The highest velocities were predicted for the most dilute flows in this study.

3) The magnitude of the flow velocity varied non-monotonically with the concentration. In moving from 9% to 15%, and finally to 21%, it showed an initial decrease followed by a slight increase.

A sensitivity analysis can shed further light on the relationship between the turbulence model, the empirical parameters used in the rheological model, and the predictions made by the proposed flow equations regarding the boundary layer height and the velocity of the flow on different slopes.

REFERENCES

Acrivos, A., Shah, M. J., & Petersen, E. E. (1960). Momentum and heat transfer in laminar boundary layer flows of non-Newtonian fluids past external surfaces. *AIChE Journal*, *6*(2), 312–317. doi: 10.1002/aic.690060227

Anwar, I., Amin, N., & Pop, I. (2008). Mixed convection boundary layer flow of a viscoelastic fluid over a horizontal circular cylinder. *International Journal of Non-Linear Mechanics*, *43*(9), 814–821. doi: 10.1016/j.ijnonlinmec.2008.04.008

Balachandar, S. (2009). A scaling analysis for point-particle approaches to turbulent multiphase flows. *International Journal of Multiphase Flow*, *35*(9), 801–810. doi: 10.1016/j.ijmultiphaseflow.2009.02.013

Balmforth, N. J., Craster, R. V., Hewitt, D. R., Hormozi, S., & Maleki, A. (2017). Viscoplastic boundary layers. *Journal of Fluid Mechanics*, *813*, 929–954. doi: 10.1017/jfm.2016.878

Cantelli, A. (2009). Uniform Flow of Modified Bingham Fluids in Narrow Cross Sections. *Journal of Hydraulic Engineering*, *135*(8), 640–650. doi: 10.1061/(ASCE)HY.1943-7900.0000092

Elghobashi, S., & Truesdell, G. C. (1993). On the two-way interaction between homogeneous turbulence and dispersed solid particles. II. Particle dispersion. *Physics of Fluids*, *5*(7), 1790–1801. doi: 10.1063/1.868254

Groenenberg, R. M., Sloff, K., & Weltje, G. J. (2009). A high-resolution 2-DH numerical scheme for process-based modeling of 3-D turbidite fan stratigraphy. *Computers & Geosciences*, *35*, 1686–1700. doi: 10.1016/j.cageo.2009.01.004

Harris, J. (1977). *Rheology and Non-Newtonian Flow*. Longman.

Huang, X., & Garcia, M. H. (1998). A Herschel–Bulkley model for mud flow down a slope. *Fluid Mechanics*, *374*, 305–333. doi: 10.1017/S0022112098002845

Iverson, R. M. (1997). The physics of debris flows. *Reviews of Geophysics*, *35*, 245–296. doi: 10.1029/97RG00426

Jiang, L., & Le Blond, P. H. (1993). Numerical Modelling of an Underwater Bingham Plastic Mud Slide and the Waves which it Generates. *Journal of Geophysical Research*, *98*(C6), 10303–10317. doi: 10.1029/93JC00393

Jiang, L., & LeBlond, P. H. (1992). The coupling of a submarine slide and the surface waves which it generates. *Journal of Geophysical Research*, *97*(C8), 12731–12744. doi: 10.1029/92JC00912

Kármán, T. V. (1921). Über laminare und turbulente Reibung. *ZAMM - Journal of Applied Mathematics and Mechanics / Zeitschrift für Angewandte Mathematik und Mechanik*, *1*(4), 233–252. doi: 10.1002/zamm.19210010401

L. Jing, Kwok, C. Y., Leung, Y. F., Zhang, Z., & Dai, L. (2018). Runout Scaling and Deposit Morphology of Rapid Mudflows. *Journal of Geophysical Research: Earth Surface*, *123*(8), 2004–2023. doi: 10.1029/2018JF004667

M. Pastor, Blanc, T., Haddad, B., Morles, M. S., Dutto, P., Stickle, M. M., … Fernández Merodo, J. A. (2015). Depth Averaged Models for Fast Landslide Propagation : Mathematical, Rheological and Numerical Aspects. *Archives of Computational Methods in Engineering*, *22*, 67–104. doi: 10.1007/s11831-014-9110-3

Marble, F. E. (1970). Dynamics of Dusty Gases. *Annual Review of Fluid Mechanics*, *2*, 397–446. doi: 10.1146/annurev.fl.02.010170.002145

Meiburg, E., Radhakrishnan, S., & Nasr-azadani, M. (2017). Modeling Gravity and Turbidity Currents : Computational Approaches and Challenges. *Applied Mechanics Reviews*, *67*(4), 1–23. doi: 10.1115/1.4031040

Oldroyd, J. G. (1947). Two-dimensional plastic flow of a Bingham solid: A plastic boundary-layer theory for slow motion. *Mathematical Proceedings of the Cambridge Philosophical Society*, *43*(3), 383–395. doi: 10.1017/S0305004100023616

Pratson, L. F., Imran, J., Parker, G., Syvitski, J. P. M., & Hutton, E. (2000, jan). *Debris Flows vs. Turbidity Currents: A Modeling Comparison of Their Dynamics and Deposits* (Vol. 72). American Association of Petroleum Geologists. doi: 10.1306/M72703C6

Rajagopal, K. R., Gupta, A. S., & Wineman, A. S. (1980). On a boundary layer theory for non-Newtonian fluids. *Lett. Appl. Engng Sci.*, *18*, 875–883. doi: 10.1016/0020-7225(80)90035-X

Ruckenstein, E. (1994). Thermal and Diffusion Boundary Layers in Viscoelastic Flows. *Industrial & Engineering Chemistry Research*, *33*(10), 2331–2335. doi: 10.1021/ie00034a011

Sadeqi, S., Khabazi, N., & Sadeghy, K. (2011). Blasius flow of thixotropic fluids: A numerical study. *Communications in Nonlinear Science and Numerical Simulation*, *16*(2), 711–721. doi: 10.1016/j.cnsns.2010.05.009

Schlichting, H. (1964). *Boundary -Layer Theory* (7th ed.). New York: McGraw-Hill Book Company. doi: 10.1119/1.1971812

Sequeiros, O. E., Cantelli, A., Viparelli, E., White, J. D., Garcí, M. H., & Parker, G. (2009). Modeling turbidity currents with nonuniform sediment and reverse buoyancy. *Water Resources Research*, *45*(6), 1–28. doi: 10.1029/2008WR007422

Shampine, L. F., & Reichelt, M. W. (1997). The MATLAB ODE Suite. *SIAM Journal on Scientific Computing*, *18*(1), 1–22. doi: 10.1137/S1064827594276424

Tollmien, W., Schlichting, H., Görtler, H., & Riegels, F. W. (1961). Über Flüssigkeitsbewegung bei sehr kleiner Reibung. In F. W. Riegels (Ed.), *Ludwig prandtl gesammelte abhandlungen: zur angewandten mechanik, hydro- und aerodynamik* (pp. 575–584). Berlin, Heidelberg: Springer Berlin Heidelberg. doi: 10.1007/978-3-662-11836-8_43

Uhlmann, M. (2008). Interface-resolved direct numerical simulation of vertical particulate channel flow in the turbulent regime. *Physics of Fluids*, *20*(5). doi: 10.1063/1.2912459

van Kessel, T., & Kranenburg, C. (1996). Gravity Current of Fluid Mud on Sloping Bed. *Journal of Hydraulic Engineering*, *122*(12), 710–717. doi: 10.1061/(ASCE)0733-9429(1996)122:12(710)

Vreman, B., Geurts, B. J., Deen, N. G., Kuipers, J. A. M., & Kuerten, J. G. M. (2009). Two- and four-way coupled euler-lagrangian large-eddy simulation of turbulent particle-laden channel flow. *Flow, Turbulence and Combustion*, *82*(1), 47–71. doi: 10.1007/s10494-008-9173-z

White, F. M. (1991). *Viscous Fluid Flow*. McGraw-Hill.

6

CONCLUSIONS

6.1. GENERAL CONCLUSIONS ON THE MAIN RESULTS

The primary focus of this thesis has been to provide the reader with new insights regarding the questions:

(1) How are the dynamics of subaqueous gravity flows related to their deposits?, and,

(2) Why are these flows able to travel so far?

In an attempt to answer the first question, a series of flume experiments was carried out at the Eurotank Laboratory of Utrecht University. The results demonstrate that the most complete anatomy of subaqueous clay-rich gravity flows is composed of three vertically stacked layers, 1) a free shear layer, 2) a plug layer, and 3) a boundary layer. A classification is proposed for these flows based on the state of the free shear and boundary layers and existence of a plug layer (Figure 6.1)(Chapter 2). According to this classification, a clay-laden density flow may fall within one of four distinct flow types: 1) a clay-rich plug flow (PF), 2) a top transitional plug flow (TTPF), 3) a transitional turbidity current (TTC), or 4) a turbulent turbidity current (TC).

Study of the deposits emplaced by the experimental runs revealed some common signatures for each flow type. Figure 6.1 gives an overview of the results. In general, clay-rich PFs resulted in either no deposition or deposition of a thin bottom sand layer. TTPFs and TTCs were mostly characterized by a thin bottom sand layer. The bottom sand layers in PFs, TTPFs, and TTCs were subsequently overlain by a mud-sand mixture that was emplaced by the tail of the flow. TCs, which have abundantly been studied in other works, resulted in the deposition of a thick massive bottom sand layer which was overlain by either a mud-sand mixture or a sand and silt planar lamination from the tail of the flow. For all flows, a top thin clay drape was deposited from the suspension after the flows stopped.

The results demonstrate that the hybrid beds, as deposits of clay-laden flows, should be abundant in clay-rich deep-water systems (Chapter 2). While the generally held view recognizes front running turbidity currents as the main agent for the deposition of the

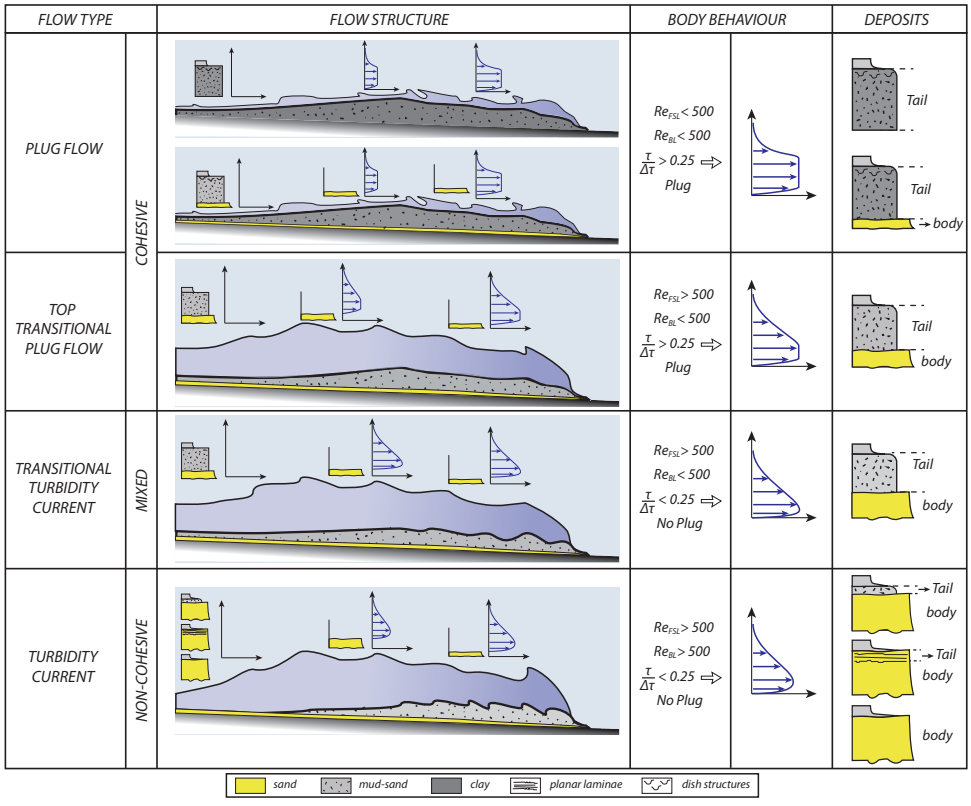

Figure 6.1: Classification scheme proposed in the present study, depicting the subaqueous sediment gravity flow types and their resulting deposits. The hybrid beds are generally produced by TTPFs and TTCs. The bottom sand layer in these beds are deposited gradually from the body of the flow, due to shearing.

bottom sand layer in the hybrid beds (Haughton et al., 2003, 2009), the experimental results from this study demonstrate that the bottom sand layers in these beds can be deposited gradually (in contrast to *en masse*) from the body of a variety of flows, including highly cohesive PFs, due to the shearing of the suspension. This shearing both weakens (Chapter 5) and breaks up the gel structure that is created by the electrostatically charged clay particles at high concentrations ($\gtrapprox$ 4%), thus reducing the yield stress of the suspension (Chapter 4) and allowing the sand particles, which are otherwise supported by the static yield stress, to settle out. This finding is important for facies analyses and lithology prediction in deep-water basins.

Example 6.1.1: Hybrid beds of deep-water fans in the northern North Sea
Study of cores from Late Jurassic sandy deep-water fan systems in two separate anoxic half-graben basins of northern North Sea, namely, the Kingfisher area on the outer fringe of the Brae-Miller fan (Mcclure, 1990) and the Penguin area on the distal fringe of the Magnus sandy fan (Ravnas & Steel, 1997), has suggested that the outer parts of these fans are dominated by hybrid

event beds (Haughton et al., 2003). These are composed of basal structureless and dewatered sandstone beds overlain by clast-rich argillaceous sandstones and sandy mudrocks interpreted as debrites.
Previous study (Haughton et al., 2003), linked the creation of these beds to debris flows that, at some point on their journey, purportedly fell behind front running turbidity currents that deposited sand layers. The slower debris flows would then run over these sand layers, emplacing their clay-rich deposits on top of them.
While this idea may be valid, it requires an explanation why debris flows may repeatedly fall behind turbidity currents. Since hybrid beds have been reported from various locations, the explanation should ideally be independent of the setting and the composition. The physical justifications that support such a phenomenon are difficult to provide.
The results obtained from the present study suggest that the sand layers observed in the Brae-Miller and the Magnus fans may have been deposited from the bodies of clay-rich turbidity currents which, after emplacing most of their sand in the proximal regions (due to high levels of shearing that successfully sieved the sand particles through the clay), transformed into transitional turbidity currents (TTCs). The clay-rich layers that are observed in the outer fringes of these fans were either deposited by the tail of the TTCs (where the force of gravity is counteracted by the critical yield stress of the suspension), or in the outermost parts, created due to the freezing of the entire flow, once the slope or the flow height diminished sufficiently.

Furthermore, this study emphasizes that the structure of the deposit at a location is to a large extent influenced by the time-dependent variations in the flow height and the turbulence levels that are brought about by the passage of different parts of the flow from that location (Chapter 2). For cohesive plug flows, the final deposit is mainly a result of a time-dependent decrease in the flow height (from the body to the tail) and dominance of the yield strength of the suspension over the force of gravity. For dilute clay-laden flows, time dependence may be in the form of fluctuations in the turbulence levels. For instance, the sand-silt interlamination observed in the deposits of turbidity currents are concluded to have been produced by those flows whose turbulent energy levels moved back and forth between those of a flow that was able to support only the smaller silt particles, and those that could support both silt and sand particles. This stresses the importance of the variabilities that exist inside a single flow as opposed to flows outpacing each other in a single event.
In moving from low to high Reynolds numbers, it was observed that the thick mud-sand deposit that is emplaced by the tail of the flow diminishes in thickness and more sand is deposited from the body. At very high Reynolds numbers however, very little deposit was emplaced by the flow. Consequently, the Reynolds versus Froude number plots from this study suggest the existence of flows within the turbulent regime that can produce massive clean sand deposits (Chapter 2).
To address why subaqueous gravity flows can travel so far, the rheology of kaolinite clay, sand, and water mixtures was theoretically, experimentally, and numerically studied (Chapters 3 and 4). Research on the rheology of clay-water suspensions has long shown

that, while flow initiation for these suspensions is controlled by the static yield stress, its stoppage is dictated by the critical yield stress. In this study, it is suggested that this fact has a direct bearing on the run-out distance of clay-laden gravity flows, i.e., that the difference between the static and the critical yield stresses of sediment suspensions, to a great extent, governs the run-out distance of gravity flows. The rheometry tests performed in this study revealed that the critical yield stresses of kaolinite clay, sand, and water mixtures can be much smaller than their static yield stresses (~ 10 times). From the momentum equation, it is deduced that for a flow of such a suspension to stop, either the slope, or the flow height, has to decrease dramatically (Chapters 3).

Example 6.1.2: The flow at Agadir, northwest Africa

Talling et al. (2007) give an account of a flow at Agadir, northwest Africa, that traveled for ~ 1500 km. The flow was initiated by a landslide from the continental shelf and contained 125 km^3 of sediment. After passing through the Agadir canyon, it entered a ~ 100-km-long area of open sea floor, that Talling et al. termed the 'exit ramp'. The flow allegedly deposited very little sediment on the exit ramp and locally eroded up to one meter of underlying material. The end of the exit ramp marks a drop in the slope from 0.05° to 0.01°. This coincides with the start of a debrite deposit that extends for ~ 250 km inside the Agadir basin. The debrite is wholly encased in turbidite. The turbidite deposits spread more widely than the debrite and continue into the Madeira abyssal plain, ~ 800 km further away.

From the erosional features described by Talling et al. (2007), it can be deduced that the flow at Agadir must have been erosional throughout the Agadir canyon and the exit ramp. This make it difficult to comment with confidence on the flow type, before it entered the Agadir basin. However, according to the sedimentary logs, since the flow resulted in very little sand deposition at the beginning of the Agadir basin, it can be concluded that at that point it was a plug flow whose tail resulted in a 1.5-meter thick debrite. The bottom sand layer that appears close to the center of the Agadir basin may have been produced from the body of the flow due to shearing. This probably occurred due to flow acceleration that was induced by the increase in the slope in this region from < 0.01∘ to ~ 0.02∘. The top sand layer in Bed 5 may have been produced by a dilute turbidity current that occurred in the wake of the main event and continued to travel into the Madeira abyssal plain.

The flow at Agadir has been estimated to have had a density of ~ 1250 kg/m^3 (Talling et al., 2007). This is close to 15% sediment volume concentration. On low gradients, the tail of such a clay-laden flow would result in the deposition of a mud-sand mixture. Reading a critical yield stress of ~ 0.015 Pa, from Figure 3.2 and assuming a flow height of ~ 1.5 m based on the sedimentary logs, the slope over which such a flow would stop can be approximated from equation (3.3) to be, $\theta_c \sim 0.0002°$. The fact that this slope is smaller than the slope on which the actual flow stoppage occurred suggests that, 1) The sediment concentration within the tail of the flow may have been higher than the approximated value of ~ 1250 kg/m^3, and/or 2) The sediment com-

position may have been different from the one studied in this work.

Another contributing factor to the long run-outs of clay-laden gravity flows can be explained by their ability to stay close to the equilibrium conditions. It is theoretically suggested that, regardless of the regime, all gravity flows reach the equilibrium state at least once during their journey from the proximal to the distal regions (Chapters 3). Since the presence of cohesive clay particles in density flows can boost their ability to resist disturbances and promote turbulence damping, it is suggested that clay is the main agent that allows sediment flows stay close to the equilibrium conditions for extended periods of time and thus, achieve large run-out distances.

In conclusion, although hydroplaning (Mohrig et al., 1998) and flow stratification (Kneller et al., 2016) have commonly been cited as the main mechanisms behind the long run-outs of clay-laden subaqueous flows, this research, through theoretical reasoning, quantitative rheological measurements, and numerical modeling, demonstrates that the clay-related rheology is the key player for explaining the remarkable run-out distance of clay-rich density flows. Consequently, the numerical models which aim to accurately simulate the behavior of these flows on varying slopes should employ rheological models that can capture the flow behavior of clay-water suspensions.

In order to advance towards the construction of a predictive numerical model, a new structural kinetics rheological model with four empirical parameters is proposed (Chapter 4). It is suggested that for the materials that exhibit a minimum in their strain controlled flow curves, the structure model must be a symmetric function of strain rate and stress. An expression for the elastic strain of the flowing structure is derived by assuming spring like interactions between particles at the micro-scale, and based on the structure model. It is shown that the final set of equations can reproduce the viscosity bifurcation that sediment suspensions may exhibit under a given load. Therefore, the use of the model in numerical simulations allows for accurate prediction of the run-out distance of clay-laden gravity flows. Furthermore, the model offers a phenomenological picture for the apparent yield stress, that is unique (Chapter 4). As will be explained in section 6.2.1, this opens up the opportunity for future research on modeling of shear-induced particle settling in materials which exhibit viscosity bifurcation.

Using the rheological model developed in this study, the validity of the boundary layer approximation is investigated for clay-laden flows (Chapter 5). It is concluded that the boundary layer approximation becomes less appropriate for higher sediment concentrations. Using the boundary layer approximation, a simplified set of equations is then derived. The steady state solutions of these equations demonstrate that clay-laden flows can stay mobile on very low gradients (Chapter 5).

6.2. FUTURE RESEARCH AND ECONOMIC IMPLICATIONS

Some of the future research and economic implications of the work presented in this thesis are discussed in the following paragraphs.

6.2.1. PARTICLE SETTLING VELOCITY

Clay-rich gravity flow deposits are distinct from those of their dilute counterparts in lithology and are emplaced through a different depositional process (Hermidas et al.,

2018; Talling et al., 2012). This difference is induced by the manner in which clay particles affect the sedimentation process. Although there has been a lot of research on the deposition of clay flocs (Winterwerp, 2000), currently only few articles address the issue of deposition of particles suspended in flowing yield-stress fluids (Gheissary & Van Den Brule, 1996; Merkak et al., 2009; Ovarlez et al., 2012), and none addresses sedimentation of particles in flowing thixotropic fluids.

At high clay concentrations, the static yield stress of the suspension, τ_y, can counterbalance the net gravitational force exerted on a particle and hence keep it in suspension. The dimensionless parameter which quantifies the stability of a particle in a yield stress fluid is therefore,

$$Y = \frac{\tau_y}{\Delta\rho g d}, \tag{6.1}$$

where, d is the particle diameter, and $\Delta\rho$ is the difference between the density of the particle and the fluid. The lowest value of Y beyond which a particle is immobile in a fluid is referred to as the stability criterion and is denoted by Y_s. Merkak et al. (2009), studied the dynamics of a particle suspended in a viscoplastic fluid flowing in a cylindrical pipe. The flow in their study was composed of an inner plug layer and an outer shear layer. During their experiments they observed no settling for the particles that were placed inside the plug layer. Particles that were placed inside the shear layer, on the other hand, settled to the bottom of the pipe. From their observations they concluded that for particles that are denser than the fluid, the stability criterion is ~ 3. For $Y_s > 3$ a suspension of solid particles can flow without being destabilized. Ovarlez et al. (2012) studied the time evolution of volume fraction of non-colloidal particles in yield stress fluids during Couette flows. Contrary to the conclusion of Merkak et al. (2009), Ovarlez et al. (2012) observed that shearing induced sedimentation in all systems which were stable at rest. They derived the following expression for the settling velocity of a particle in a yield-stress fluid,

$$V(\phi) = \alpha \frac{\Delta\rho g d^2}{\mu(\dot{\gamma}_l(\phi))} f_{Newt.}(\phi), \tag{6.2}$$

where,

$$\dot{\gamma}_l(\phi) = \bar{\dot{\gamma}} \sqrt{(1-\phi/\phi_{div})^{-2.5\phi_{div}}(1-\phi)^{-1}}, \tag{6.3}$$

is the average local shear rate in the interstitial fluid. Equation (6.2) is the Stokes settling velocity, modified for the case of high solid fraction in a yield stress fluid. The effect of particle-particle interaction (high solid fraction) on the settling velocity is incorporated in (6.2) by the hindrance function $f_{Newt.}(\phi)$, as in a Newtonian fluid (Davis & Acrivos, 1985). $f_{Newt.}$ is a function of particle volume fraction ϕ. $\mu(\dot{\gamma}_l(\phi))$ is the apparent viscosity of the fluid and is a function of the average local shear rate. For the case of a single particle in a Newtonian fluid α is a constant equal to 1/18. However, this constant seems to take on other values at low and high shear rates. At low shear rates (plastic regime) $\alpha \approx 1/18$. However, at high shear rates, the value of α is unknown but is predicted to be significantly higher than 1/18 (by a factor of 3 or more) (Ovarlez et al., 2012). Finally, in (6.3), $\phi_{div} = 60.5\%$, is the maximum packing fraction of the solid particles.

From Figure (5.10), it can be seen that the value of the structure parameter inside the

plug region is smaller than 1. This suggests that if the particles inside the plug layer are heavy enough, they should be able to break the weakened structure and settle out of the suspension. Thus, the difference between the results of Merkak et al. (2009) and Ovarlez et al. (2012), may have been produced by the weight of the particles and the type of materials they used in their experiments.
Using the expression for the apparent yield stress (Chapter 4), an analogous relation to (6.1) can be proposed to quantify the stability of a sand particle in a clay-water suspension,

$$Y = \frac{\tau_{y,+}}{\Delta\rho g d}, \tag{6.4}$$

where, $\tau_{y,+}$ is the apparent yield stress of the mixture.
Following the same procedure as Ovarlez et al. (2012), one may be able to derive a particle settling velocity that does not depend on the value of the Bingham number.

6.2.2. SOCIETAL AND ECONOMIC IMPLICATIONS

The societal and economic impacts of this research can be analyzed from a governmental and an industrial perspective. The governmental impacts can be studied in the context of the preventive measures that the governments may take to reduce the damages that gravity flows can inflict on public households, submarine cables, boats and ships, individuals' lives, etc. Furthermore, it is known that, aside from natural causes, such flows can be created from human activities, such as slope oversteepening by landfills, and dredging or trawling which can have a significant impact on the marine ecology of an area (Payo-Payo et al., 2017). Recently, there has been a renewed interest in mining of polymetallic nodules that contain critical raw materials, e.g., cobalt, nickel, copper, manganese as well as sizable amounts of gallium and rare earth elements, from the seabed. Developments in this field are being made against a backdrop where the regulations to control deep-sea mining are being established. Currently, it is unclear what the final environmental regulations will look like, however they most probably will address the plumes caused by the mining vehicles and dewatering of the ores at the ship. Process-based models that can accurately simulate such flows can therefore help with both recognizing and emplacing the proper preventive measures by the governments.
Today successful production of oil and gas holds great sway over the economy. The Congressional Budget Office recently estimated that the total gross income collected by the U.S. federal government from offshore oil and gas production averaged at $8 billion per year from 2005 to 2014. In contrast, the income from onshore production averaged at $3 billion for the same period (Weimer, 2018). The necessary investments that lead to these incomes include offshore structures to explore, appraise, and produce oil and natural gas reservoirs. Consequently, from an industrial perspective, accurate prediction of the run-out distance of sediment gravity flows (and therefore their destructive capabilities) and the type of deposit they emplace at a location can be beneficial for risk mitigation purposes for offshore structures as well as oil and gas exploration.

REFERENCES

Davis, R. H., & Acrivos, A. (1985). Sedimentation of Noncolloidal Particles at Low Reynolds Numbers. *Annual Review of Fluid Mechanics*, *17*, 91–118. doi: 10.1038/170368a0

Gheissary, G., & Van Den Brule, B. H. (1996). Unexpected phenomena observed in particle settling in non-Newtonian media. *Journal of Non-Newtonian Fluid Mechanics*, *67*(1-3), 1–18. doi: 10.1016/S0377-0257(96)01436-X

Haughton, P., Barker, S. P., & Mccaffrey, W. D. (2003). ' Linked ' debrites in sand-rich turbidite systems – origin and significance. *Sedimentology*, *50*, 459–482.

Haughton, P., Davis, C., McCaffrey, W., & Barker, S. (2009). Hybrid sediment gravity flow deposits - Classification, origin and significance. *Marine and Petroleum Geology*, *26*, 1900–1918. doi: 10.1016/j.marpetgeo.2009.02.012

Hermidas, N., Eggenhuisen, J. T., Silva Jacinto, R., Luthi, S. M., Toth, F., & Pohl, F. (2018). A Classification of Clay-Rich Subaqueous Density Flow Structures. *Journal of Geophysical Research*, *123*(5), 945–966. doi: 10.1002/2017JF004386

Kneller, B., Nasr-Azadani, M. M., Radhakrishnan, S., & Meiburg, E. (2016). Long-range sediment transport in the world's oceans by stably stratified turbidity currents. *Journal of Geophysical Research*, *121*(12). doi: 10.1002/2016JC011978

Mcclure, N. M. (1990). Miller Field : A Subtle Upper Jurassic submarine Fan Trap in the South Viking Graben, United Kingdom sector, North Sea. In *Giant oil and gas fields of the decade 1978-88* (p. 1519). Tulsa, OK: American Association of Petroleum Geologists.

Merkak, O., Jossic, L., & Magnin, A. (2009). Migration and Sedimentation of Spherical Particles in a Yield Stress Fluid Flowing in a Horizontal Cylindrical Pipe. *AIChE Journal*, *55*(10), 2515–2525. doi: 10.1002/aic.11852

Mohrig, D., Whipple, K. X., Hondzo, M., Ellis, C., & Parker, G. (1998). Hydroplaning of subaqueous debris flows. *GSA Bulletin*, *110*(3), 387–394. doi: 10.1130/0016-7606(1998)110<0387:HOSDF>2.3.CO;2

Ovarlez, G., Bertrand, F., Coussot, P., & Chateau, X. (2012). Shear-induced sedimentation in yield stress fluids. *Journal of Non-Newtonian Fluid Mechanics*, *177-178*, 19–28. doi: 10.1016/j.jnnfm.2012.03.013

Payo-Payo, M., Silva Jacinto, R., Lastras, G., Rabineau, M., Puig, P., Martín, J., … Sultan, N. (2017). Numerical modeling of bottom trawling-induced sediment transport and accumulation in La Fonera submarine canyon, northwestern Mediterranean Sea. *Marine Geology*, *386*, 107–125. doi: 10.1016/j.margeo.2017.02.015

Ravnas, R., & Steel, R. (1997). Contrasting styles of Late Jurassic syn-rift turbidite sedimentation: a comparative study of the Magnus and Oseberg areas , northern North Sea. *Marine and Petroleum Geology*, *14*(4), 417–449.

Talling, P. J., Masson, D. G., Sumner, E. J., & Malgesini, G. (2012). Subaqueous sediment density flows: Depositional processes and deposit types. *Sedimentology*, *59*, 1937–2003. doi: 10.1111/j.1365-3091.2012.01353.x

Talling, P. J., Wynn, R. B., Masson, D. G., Frenz, M., Cronin, B. T., Schiebel, R., … Amy, L. A. (2007, nov). Onset of submarine debris flow deposition far from original giant landslide. *Nature*, *450*, 541–544. doi: 10.1038/nature06313

Weimer, P. (2018). Deeper Waters : How Science and Technology Pushed Exploration to Greater Depths. *The AAPG Explorer*(January 2017).

Winterwerp, J. C. (2000). *On the dynamics of high-concentrated mud suspensions.* Delft: Judels Brinkman & Ammerlaan.

ACKNOWLEDGEMENTS

This work would not have been possible without the financial support from the Netherlands Research Center for Integrated Solid and Earth Science (ISES).

I am specially indebted to Stefan M. Luthi for giving me the opportunity to work on this project, granting me the freedom to explore different research avenues, and for his leadership and unwavering support throughout these four years. He is a formidable supervisor with an outsized personality.

I would like to express my gratitude to Joris T. Eggenhuisen, for inviting me to Utrecht, welcoming me into his team, and allowing me to carry out my experiments at the renowned Eurotank laboratory. His meticulous comments and dedicated craftsmanship truly elevated my work by leaps and bounds.

I am grateful to Ricardo Silva Jacinto for introducing me into the world of rheology and lending me his expertise when I was performing the rheometry tests. His remarkable intuition regarding the physical processes was fundamental in the development of the rheological model that is presented in Chapter 4 of this thesis.

Special thanks go to Ferenc Tóth and Florian Pohl for their excellent assistance in performing the flume experiments and carrying out the grain size analysis.

I thank H. K. J. Heller, A. Middeldorp, and A. D. Schuit for their great technical support in obtaining the rheometry data.

Special thanks go to Joeri Brackenhoff for his generous assistance in translating the summary of this thesis into Dutch.

Along the way the associations have been so rewarding. Working with João Trabucho Alexandre and Jan de Leeuw was exciting. We talked about clay minerals, the effect of silt on the particle settling, and inception of channel levee systems in the Big Tank. My discussion with Dennis den Ouden-van der Horst about the solutions of non-linear ODEs was insightful. Talking with Cor Kasbergen about tensor calculus and index gymnastics was helpful.

Thinking back, I find I am also greatly indebted to all my teachers and supervisors from the faculty of Aerospace Engineering. I owe them a lot.

My special gratitude goes to Marc Gerritsma for introducing me to the field of differential geometry, antisymmetric tensors and differential forms, and algebraic

topology during my master's thesis. This knowledge helped me when I was deriving the three-dimensional versions of our rheological model.

Working within the Applied Geology section, and in close collaboration with the Applied Geophysics & Petrophysics group here at TUDelft, was a joy. Therefore, I would like to extend my thanks to all the staff members, and all the supporting staff for their great support. I also would like to thank all my colleagues from the CiTG for the good memories that we share.

Finally, I come to the most important thing. My heartfelt thanks go to my family. I hope I have been strong when they needed me. You held me up at a time when I was sorely in need of your support.

A

THREE-DIMENSIONAL FORMULATION OF THE CONSTITUTIVE MODEL: VORTEX FLOW

Within the free shear layer, let us consider a vortex flow in the polar coordinates given by,

$$\vec{u} = (v_r, v_\theta, v_z) = \left(0, \frac{C}{r}, 0\right), \tag{A.1}$$

where, C is a constant and r is the distance from the center of the vortex.
Using the rotational symmetry of vortex flow, the stress tensor in polar coordinates can be written as,

$$\tau = \begin{pmatrix} \tau^{11} & 0 & 0 \\ 0 & \tau^{11} & 0 \\ 0 & 0 & \tau^{33} \end{pmatrix}. \tag{A.2}$$

The strain tensor can be written as,

$$\gamma = \begin{pmatrix} 0 & -\frac{2Ct}{r^2} & 0 \\ -\frac{2Ct}{r^2} & -\frac{2Ct}{r} & 0 \\ 0 & 0 & 0 \end{pmatrix}. \tag{A.3}$$

and the strain rate tensor can be written as,

$$\dot{\gamma} = \begin{pmatrix} 0 & -\frac{2C}{r^2} & 0 \\ -\frac{2C}{r^2} & 0 & 0 \\ 0 & 0 & 0 \end{pmatrix}. \tag{A.4}$$

A

From the definition of the residual strain and assuming linearity between the stain and the residual strain tensors and a homogeneous, isotropic, material yields,

$$\gamma_r = \begin{pmatrix} \gamma_r^{11} & \gamma_r^{21} & 0 \\ \gamma_r^{21} & \gamma_r^{22} & 0 \\ 0 & 0 & \gamma_r^{33} \end{pmatrix}. \tag{A.5}$$

Time derivative of (A.5) can be written as,

$$\dot{\gamma}_r = \frac{\partial}{\partial t} \begin{pmatrix} \gamma_r^{11} & \gamma_r^{21} & 0 \\ \gamma_r^{21} & \gamma_r^{22} & 0 \\ 0 & 0 & \gamma_r^{33} \end{pmatrix} + \begin{pmatrix} -2C\gamma_r^{21} & -C\gamma_r^{22} & 0 \\ -C\gamma_r^{22} & 0 & 0 \\ 0 & 0 & 0 \end{pmatrix}. \tag{A.6}$$

Finally, the three-dimensional formulation of the equations (4.8) to (4.10) for the case of the vortex flow can be written as,

$$\begin{pmatrix} \tau^{11} & 0 & 0 \\ 0 & \tau^{11} & 0 \\ 0 & 0 & \tau^{33} \end{pmatrix} = G_0\lambda \begin{pmatrix} \gamma_r^{11} & \gamma_r^{21} & 0 \\ \gamma_r^{21} & \gamma_r^{22} & 0 \\ 0 & 0 & \gamma_r^{33} \end{pmatrix} + \mu \begin{pmatrix} 0 & -\frac{2C}{r^2} & 0 \\ -\frac{2C}{r^2} & 0 & 0 \\ 0 & 0 & 0 \end{pmatrix}, \tag{A.7}$$

$$\dot{\lambda} = \alpha(1-\lambda) - |\tau : \dot{\gamma}|\beta\lambda, \tag{A.8}$$

$$\begin{aligned} \frac{\partial}{\partial t} \begin{pmatrix} \gamma_r^{11} & \gamma_r^{21} & 0 \\ \gamma_r^{21} & \gamma_r^{22} & 0 \\ 0 & 0 & \gamma_r^{33} \end{pmatrix} &= \begin{pmatrix} 2C\gamma_r^{21} & C\gamma_r^{22} & 0 \\ C\gamma_r^{22} & 0 & 0 \\ 0 & 0 & 0 \end{pmatrix} + \begin{pmatrix} 0 & -\frac{2C}{r^2} & 0 \\ -\frac{2C}{r^2} & 0 & 0 \\ 0 & 0 & 0 \end{pmatrix} \\ &- \frac{(1-\lambda)\alpha}{\lambda} \begin{pmatrix} \gamma_r^{11} & \gamma_r^{21} & 0 \\ \gamma_r^{21} & \gamma_r^{22} & 0 \\ 0 & 0 & \gamma_r^{33} \end{pmatrix}. \end{aligned} \tag{A.9}$$

B

DECOUPLING THE STRUCTURE MODEL FROM THE RESIDUAL STRAIN MODEL

The structure and the residual strain models in matrix form can be written as,

$$\frac{d}{dt}\underbrace{\begin{pmatrix}\lambda\\ \zeta\end{pmatrix}}_{\vec{U}} = \underbrace{\begin{pmatrix}\alpha\\ 0\end{pmatrix}}_{\vec{Q}} - \underbrace{\begin{pmatrix}\alpha+\beta|\tau:\dot{\gamma}| & 0\\ -\dot{\gamma} & \beta|\tau:\dot{\gamma}|\end{pmatrix}}_{A}\underbrace{\begin{pmatrix}\lambda\\ \zeta\end{pmatrix}}_{\vec{U}}. \tag{B.1}$$

Diagonalizing matrix A from (B.1) yields,

$$A = \underbrace{\begin{pmatrix}\alpha & 0\\ -\dot{\gamma} & 1\end{pmatrix}}_{P}\underbrace{\begin{pmatrix}\alpha+\beta|\tau:\dot{\gamma}| & 0\\ 0 & \beta|\tau:\dot{\gamma}|\end{pmatrix}}_{D}\underbrace{\begin{pmatrix}1/\alpha & 0\\ \dot{\gamma}/\alpha & 1\end{pmatrix}}_{P^{-1}}. \tag{B.2}$$

Inserting (B.2) in equation (B.1) and multiplying both sides by P^{-1} yields,

$$\begin{pmatrix}\alpha^{-1}d\lambda/dt\\ \dot{\gamma}\alpha^{-1}d\lambda/dt + d\zeta/dt\end{pmatrix} = P^{-1}Q - \begin{pmatrix}\alpha+\beta|\tau:\dot{\gamma}| & 0\\ 0 & \beta|\tau:\dot{\gamma}|\end{pmatrix}\begin{pmatrix}\lambda/\alpha\\ \dot{\gamma}\lambda/\alpha+\zeta\end{pmatrix}. \tag{B.3}$$

Furthermore, note that,

$$\frac{d}{dt}\left(\frac{\dot{\gamma}\lambda}{\alpha}+\zeta\right) - \frac{\ddot{\gamma}\lambda}{\alpha} = \frac{\dot{\gamma}}{\alpha}\frac{d\lambda}{dt} + \frac{d\zeta}{dt}. \tag{B.4}$$

Let $\kappa = \frac{\dot{\gamma}\lambda}{\alpha}+\zeta$. Then from (B.3) we have,

$$\frac{d\lambda}{dt} = \alpha - \left(\alpha+\beta|\tau:\dot{\gamma}|\right)\lambda, \tag{B.5}$$

and,

$$\frac{d\kappa}{dt} = \dot{\gamma} + \frac{\ddot{\gamma}\lambda}{\alpha} - \kappa\beta|\tau : \dot{\gamma}|. \tag{B.6}$$

Combining, $\tau = G_0\zeta + \mu\dot{\gamma}$ and the definition of κ yields,

$$\lambda = \frac{\alpha G_0\kappa - \tau\alpha + \mu\alpha\dot{\gamma}}{\dot{\gamma}G_0}. \tag{B.7}$$

Inserting (B.7) in equation (B.6) yields,

$$\frac{d\kappa}{dt} = \dot{\gamma} - \frac{\tau\ddot{\gamma}}{\dot{\gamma}G_0} + \frac{\mu\ddot{\gamma}}{G_0} + \left(\frac{\ddot{\gamma}}{\dot{\gamma}} - \beta|\tau : \dot{\gamma}|\right)\kappa. \tag{B.8}$$

Again from, $\tau = G_0\zeta + \mu\dot{\gamma}$ and the definition of κ we have,

$$\ddot{\gamma} = \frac{1}{\mu}\left(\dot{\tau} - G_0\dot{\gamma}\lambda + G_0\kappa\beta|\tau : \dot{\gamma}| - \frac{G_0\dot{\gamma}\lambda}{\alpha}\beta|\tau : \dot{\gamma}|\right), \tag{B.9}$$

and,

$$\dot{\gamma} = \frac{\tau - G_0\kappa}{\mu - G_0\lambda/\alpha}. \tag{B.10}$$

At each time step equations (B.9) and (B.10) are calculated and inserted in the decoupled equations (B.5) and (B.8) to solve for λ and κ. If stress or strain rate is imposed, their time derivatives can be calculated analytically and inserted into equations (B.9) and (B.10).

CURRICULUM VITÆ

Navid HERMIDAS

03-01-1985	Born in Teheran, Iran.

EDUCATION

2015–2019	PhD. Applied Geology Delft University of Technology
2010–2012	M.Sc. Aerospace Engineering (Fluid Dynamics) Delft University of Technology
2007–2010	B.Sc. Aerospace Engineering Delft University of Technology

AWARDS

2010	Merit Faculty Scholarship for Master's Degree at TUDelft

TEACHING

2011	Teaching assistant for the B.Sc. course "Computational Modeling"at TUDelft
2010	Teaching assistant for the B.Sc. course "Computational Fluid & Solid Mechanics"at TUDelft

OTHER SERVICES

2017	Reviewer for the Journal of Advances in Numerical Analysis

LIST OF PUBLICATIONS

JOURNAL PUBLICATIONS

1. **Hermidas, N.**, Eggenhuisen, J. T., Silva Jacinto, R., Luthi, S. M., Toth, F., & Pohl, F. (2018). A Classification of Clay-Rich Subaqueous Density Flow Structures. *Journal of Geophysical Research, 123(5)*, 945–966. doi: 10.1002/2017JF004386

2. **Hermidas, N.**, Silva Jacinto, R., Eggenhuisen, J. T., & Luthi, S. M. (2019). A new rheological model for thixoelastic materials in subaqueous gravity driven flows. *Journal of Non-Newtonian Fluid Mechanics, 266*, 102-117. doi: 10.1016/j.jnnfm.2019.02.010

3. Pohl, F., Eggenhuisen, J. T., Cartigny, M. J., Tilston, M., De Leeuw, J., & **Hermidas, N.** The influence of a slope break on turbidite deposits: an experimental investigation. In review for publication in *Journal of Marine Geology.*

CONFERENCE PROCEEDINGS

1. **Hermidas, N.**, Eggenhuisen, J. T., Luthi, S. M., Silva Jacinto, R., Toth, F., & Pohl, F. (2017). A classification of clay-rich subaqueous density flow structures. IAS 2017, Toulouse, France

2. **Hermidas, N.**, Eggenhuisen, J. T., Luthi, S. M., Silva Jacinto, R., Toth, F., & Pohl, F. (2017). A Classification of Subaqueous Density Flows Based on Transformations From Proximal to Distal Regions. EGU 2017, Vienna, Austria

3. Pohl, F., Eggenhuisen, J.T., Cartigny, M.J., De Leeuw, J., Sypkens, G., & **Hermidas, N.** (2016). Break-of-slope linked to unexpected downstream grain size coarsening in experimental and natural turbidites. AGU Fall Meeting 2016, San Francisco, USA

4. **Hermidas, N.**, Luthi, S. M., Eggenhuisen, J. T., Silva Jacinto, R., Toth, F., Pohl, F. & De Leeuw, J. (2016). Experimental and theoretical investigation of the role of clay in subaqueous sediment flows and its effect on run-out distance. EGU 2016, Vienna, Austria

5. Pohl, F., Eggenhuisen, J. T., De Leeuw, J., Sypkens, G., Cartigny, M. J., Toth, F., & **Hermidas, N.** (2016). Depositional Pattern associated with Experimental Turbidity Currents going through a Break-of-Slope. GeoTirol 2016, Innsbruck, Austria

6. **Hermidas, N.**, Luthi, S. M., Eggenhuisen, J. T., Silva Jacinto, R., Toth, F., Pohl, F., & De Leeuw, J. (2016). Experimental and theoretical study of the role of clay on the run-out distance of subaqueous sediment flows. NAC 2016, Veldhoven, Netherlands

7. Pohl, F., Eggenhuisen, J. T., De Leeuw, J., Cartigny, M. J., Tóth, F. & **Hermidas, N.** (2016). Variation in Depositional Pattern of Experimental Turbidity Currents Going Through a Break-of- Slope as a Function of Their Efficiency. AAPG 2016, Calgary, Canada

8. Pohl, F., Eggenhuisen, J. T., De Leeuw, J., Cartigny, M. J., Toth, F. & **Hermidas, N.** (2016). Depositional Pattern associated with Experimental Turbidity Currents going through a Break-of-Slope. NAC 2016, Veldhoven, Netherlands

9. Pohl, F., Eggenhuisen, J. T., De Leeuw, J., Cartigny, M. J., Toth, F. & **Hermidas, N.** (2015). Depositional Pattern associated with Experimental Turbidity Currents going through a Break-of-Slope. BSRG 2015, Keele, United Kingdom

DATASET

Hermidas, N., Eggenhuisen, J. T., Silva Jacinto, R., Luthi, S. M., Toth F., & Pohl F. (2016). Experimental clay-laden density flow velocity and deposit data from the Eurotank laboratory. *SEANOE*, doi: 10.17882/54834